Final Report to NASA KSC on the Airborne Field Mill Project (ABFM) under NASA Grant NAG10-284

James E. Dye and Sharon Lewis
National Center for Atmospheric Research
Boulder, Colorado

June 4, 2004

TABLE OF CONTENTS

1. INTRODUCTION

Lightning poses considerable threat to the launch of the Shuttle or other space vehicles at Kennedy Space Center and also can pose a threat at other launch facilities as well. Experience has suggested that the current Lightning Launch Commit Criteria appear to restrict launches in some cases when there may not be hazard from triggered lightning. This is in part because information is lacking on electric fields and microphysical conditions in clouds that may be electrified and may or may not pose a hazard. Anvils from thunderstorms, thick clouds and debris clouds are of particular interest in this regard. The Airborne Fill Mill Project (ABFM) was conducted in June 2000, February 2001 and May/June 2001. The purpose of these campaigns was to obtain simultaneous in-situ airborne measurements of the electric field and microphysical content in anvils, thick clouds, debris clouds and other cloud conditions near Kennedy Space Center using the Univ. of North Dakota Citation jet aircraft. The aircraft flights were coordinated with the WSR74C 5 cm radar at Patrick Air Force Base and the WSR 88D 10 cm NEXRAD radar at Melborne, Florida. When possible flights were conducted over the surface based field mill network at KSC and in the operating range of the KSC Lightning Detection and Ranging (LDAR) system and the Cloud to Ground Lightning Surveillance System (CGLSS).

ABFM was a joint project with in addition to investigators from NCAR, Dr. Eric Defer, now at National Observatory of Athens, Greece, Drs. Hugh Christian, Monte Bateman, and Douglas Mach of NASA Marshall Space Flight Center (MSFC); Dr. Anthony Grainger, PI for the Citation from the University of North Dakota; Mr. Paul Willis of NOAA/Hurricane Research Division; Dr. E. Phillip Krider and Ms Natalie Murray from the University of Arizona; and Dr. John Willett of Garrett Park, Maryland. Dr. Francis Merceret of NASA Kennedy Space Center was also one of the investigators as well as the Project Monitor.

In addition to the goal of obtaining measurements to identify possible relationships of electric field, microphysics and radar structure of these clouds, a specific goal was to try to determine decay rates of electric field within the anvils over KSC to see if these decay rates were consistent with decay rates theoretically predicted in a simple model developed by Dr. John Willett.

The flight characteristics and description of sensors to measure state parameters, air motions and microphysics of the Citation are described in Appendix A at the end of this report. Table A.2 presents the measurement capabilities available during ABFM, while Table A.3 list the instruments along with general information on range, time response and accuracy. There were six microphysical sensors on the aircraft to measure concentration and size for hydrometeors from sizes of a few microns to several millimeters. Additionally, there were two sensors for detection of liquid water content. The microphysical instruments are described in Appendix C.

In-situ measurement of the 3-dimensional electric field was a critical component of instrumentation on the aircraft. This was accomplished using 6 high sensitivity, fast response time electric field mills designed and built by NASA MSFC. The placement of the field mills on the aircraft and the techniques used to determine the 3-dimensional electric field and calibration thereof is described in Appendix B. Appendices D and E describe the operating characteristics, calibration and processing of the WSR74C and NEXRAD radar data. Appendices F and G describe the operation and limitations of the Lightning Detection and Ranging (LDAR) instrument and the Cloud to Ground Lightning Surveillance System (CGLSS). At KSC there also is a surface network of field mills and during ABFM this was supplemented with a mobile field mill operated by the University of Arizona. The measurements and analysis of results from the surface and mobile field mills will be described in a separate report by Ms. Natalie Murray and Dr. Phillip Krider of the University of Arizona.

2. THE FIELD CAMPAIGNS

Three field campaigns were flown during ABFM II. [The first ABFM project was conducted in 1991 and 1992, but for brevity in this report, we will refer to ABFM II simply as ABFM]. The June 2000 and the May/June 2001 campaigns were intended primarily to investigate anvils and the decay of other summertime convective events. The February 2001 campaign was climatologically timed to investigate thick clouds and long -lived anvils passing over KSC that originated from storms over the Gulf of Mexico. Unfortunately the February campaign was held during a period of intense drought in central Florida. Consequently only one thick cloud case over KSC was obtained and another extremely marginal thick cloud case near Jacksonville, FL.

For the June campaigns, especially June 2000, initial penetrations were often made near to, but at a safe distance from, the convective cores of storms. Then subsequent passes were made in the anvil at different distances downstream to examine the decay of the electric field both with time and distance. When Air Traffic Control (ATC) would allow, spiral ascents or descents were made through the anvils, but these were not nearly as frequent as was desirable for studying the anvil vertical structure. As a result our sampling of the vertical structure of the anvil of individual storms is often incomplete. However, over the period of the two summer campaigns anvils were sampled at a wide variety of altitudes in different locations relative to anvil top and bottom. Thus, the observations in aggregate are felt to be representative of conditions in anvils of Florida thunderstorms. On some occasions, horizontal passes were made through the anvil at different altitudes both across the anvil and at other times along the downwind axis. In other cases the aircraft arrived during the decay stage of the anvil, but these cases are also important because we know the lightning and reflectivity history of that storm relative to the aircraft flights.

During all 3 campaigns the Citation was flown with 2 pilots and three scientific observers: a flight scientist, a scientist to operate and monitor the UND data system and microphysical instruments, and a scientist or engineer to operate and monitor the field mill measurements. Decisions on where to fly were interactive between crew in the

aircraft and aircraft coordinators at the KSC Range Operations Control Center (ROCC). There were normally 2 or more ABFM team members on the ground in the ROCC. Aircraft position was telemetered to the ROCC and overlaid on the WSR74C near real-time vertical and horizontal displays generated using Sigmet software. In the ROCC one ABFM team member communicated with the aircraft for both safety and scientific purposes while one person operated the 74C radar display system to produce desired cross sections. Often there was an additional person in the ROCC to guide personnel operating the University of Arizona mobile field mill to the vicinity of storms of interest and especially those being investigated by the Citation. Unfortunately, storms were often too distant from KSC for the mobile field mill to be deployed directly below storms studied by the aircraft.

It is worth commenting that as we conducted the June 2000 and 2001 campaigns we quickly learned that as the Citation flew from weaker to greater reflectivity there often would be a relatively rapid increase in the electric field at reflectivities of roughly 5 to 10 dBZ. This occurred frequently enough that in June 2001 aircraft coordinators in the ROCC would often tell the aircraft crew where large increases/decreases in electric fields might be expected. The sections below explore the relationship between reflectivity, electric field, and microphysics in some detail. The goal of much of this work was to provide a basis for new, physically based Lightning Launch Commit Criteria (LLCC) rules for anvils.

Table 2.1 lists all Citation flights for the June 2000, February 2000 and May/June 2001 campaigns. The table provides a link to the ABFM Web page for each day, shows takeoff and landing times, the type of cloud investigated and a brief comment on that flight.

Table 2.1
SUMMARY OF CITATION FLIGHT DAYS AND TIMES
AIRBORNE FIELD MILL PROJECT KENNEDY SPACE CENTER

Date (yy/mm/dd)	Flight times (UTC)	Cloud Type	Summary
* 000604	2006 - 2340	o Anvil o Convective	o Case 1 (2059 - 2302): The aircraft was frequently near anvil edge, but other times close to the convection. o Case 2 (2312 - 2325): Single pass through a convective region.
000607	1755 - 1907	o Anvil	o Case 1 (1815 - 1852): A few brief moments in anvils. Mostly this is a convective flight.
000611	1758 - 2000	o Anvil o Anvil o Anvil	o Case 1 (1810 - 1826): Cell is in decay. o Case 2 (1828 - 1858): Cell was in decay at aircraft arrival. Aircraft flew on the edge of the anvil, not in the middle. o Case 3 (1901 - 1955): The part of the anvil studied was fairly close to the generating convection.
000612	1415 - 1756	o Convective o Convective	o Case 1 (1430 - 1730): o Case 2 (1730 - 1745):
000613	2016 - 2424	o Anvil	o Case 1 (2045 - 2405): Aircraft arrives at early anvil development, stays through loss of convective and until anvil mostly decayed.
000614	2058 - 2424	o Anvil o Anvil	o Case 1 (2127 - 2158): This anvil has mostly decayed. o Case 2 (2212 - 2409): A good anvil case for studying the decay of an anvil.
000617	1551 - 1724	o Debris	o Case 1 (1604 - 1724):
000620	2132 - 2349	o Debris o Convective	o Case 1 (2150 - 2227): o Case 2 (2228 - 2332): This is mostly convection.
000623 - 1	1636 - 1911	o Convective o Debris o Debris o Debris	o Case 1 (1654 - 1718): o Case 2 (1718 - 1744): o Case 3 (1748 - 1752): o Case 4 (1756 - 1824):

000623 - 2	2050 - 2115	o Stratiform	o Case 5 (2057 - 2110): A ferry flight.
000624 - 1	1624 - 1958	o Convective	o Case 1 (1645 - 1945):
000624 - 2	2044 - 2343	o Debris o Debris o Convective	o Case 2 (2100 - 2113): electrified stratiform o Case 3 (2113 - 2225): electr. stratiform. o Case 4 (2225 - 2332): but like 2 & 3 above
000625	1702 - 1817	o Convective o Anvil	o Case 1 (1710 - 1730): small, simple cell o Lost cabin pressure. o Case 2 (1730 - 1811), low altitude below anvil
000628 - 1	1400 - 1511	o Debris o Debris	o Case 1 (1404 - 1425): o Case 2 (1425 - 1456):
000628 - 2	1809 - 2135	o Anvil o Anvil & Convective o Anvil	o Case 3 (1815 - 1837): o Case 4 (1837 - 2000): The anvil was sampled only in the turns. o Case 5 (2003 - 2118): The aircraft remained too close to the core when sampling this anvil case.
Date (yy/mm/dd)	Flight times	Cloud Type	Summary
010203	2039 - 2254	Thick Cloud	o Case 1 (2053- 2005) Thick Cloud o Case 2 (2125 - 2240) Thick Cloud
010210	2147 - 2417	o CuCg o Thick Cloud	o Case 1 (2250 - 2309) o Case 2 (2312 - 2345) very marginal thick cloud near Jacksonville
010217	1611 – 1756	Attempt for Thick clouds E cals over SLF	o Case 1 (Times 1610 – 1710) Try for pre-frontal Thick clouds o Case 2 (Times 1710 – 1755) E mill cals over SLF
Date (yy/mm/dd)	Flight times	Cloud Type	Summary
010522	2120 - 2439	o Convective	o Case 1 (2133 - 2427):
010525	1829 - 2213	o Anvil o Debris o Convective o Debris	o Case 1 (1853 - 1913): o Case 2 (1913 – 1;931): o Case 3 (1931 - 1938):. o Case 4 (1938 - 1944): This might be the same debris as case 2.

		o Debris o Anvil	o Case 5 (1944 - 2038): This is debris from the convective part of case 1. o Case 6 (2028 - 2200): Aircraft was flying close to convection.
010527	2125 - 2437	o Anvil o Anvil o Anvil o Convective o Anvil	o Case 1 (2135 - 2201): Early stage. o Case 2 (2201 - 2222): o Case 3 (2222 - 2322): o Case 4 (2322 - 2409): In decay o Case 5 (2409 - 2422): This anvil is associated with the decaying cell of Case 4.
010528	1802 - 2202	o Anvil	o Case 1 (1806 - 211120):
010529	1939 - 2248	o Anvil	o Case 1 (2006 - 2231): Small anvil attached to a long lasting active core.
010602	1839 - 2258	o Anvil & Convective	o Case 1 (1914 - 2238): This is a part of a large system.
010604	1840 - 2314	o Anvil o Debris o Anvil o Anvil o Anvil	o Case 1 (1901 - 1908): This shows precip. going to the ground, but no cores. o Case 2 (1908 - 1921): This is very close to the radar data void and rather small so we can't really say much about it. o Case 3 (1921 - 1928): It is possible this anvil is from the cell studied in Case 1. o Case 4 (1928 - 2010): At this time this is a separate cell with some lightning. It will soon be taken over by the one to the south. This anvil becomes detached at about 2003. o Case 5 (2010 - 2259):
010605	1759 - 2154	o Debris o Debris o Debris o Debris	o Case 1 (1820 - 1846): o Case 2 (1853 - 1928) o Case 3 (1938 - 2044): o Case 4 (2044 - 2116):
010606	1733 - 2035	o Convective o Debris o Debris o Convective	o Case 1 (1749 - 1815): a mass of several cells o Case 2 (1815 - 1921): o Case 3 (1921 - 2005): o Case 4 (2009 - 2020): multiple cells
010607	1717 - 2027	o Convective o Debris o Debris	o Case 1 (1729 - 1936): o Case 2 (1937 - 1950): o Case 3 (1950 - 2008):

		o Convective	o Case 4 (2009 - 2017):
010610	1958 - 2346	o Convective o Anvil o Debris o Anvil o Convective	o Case 1 (2008 - 2042):. o Case 2 (2042 - 2133): This was flown very close to the source. o Case 3 (2133 - 2210): o Case 4 (2210 - 2311): o Case 5 (2311 - 2345) : Landing.
010615	2106 - 2406	o Convective o Anvil o Convective	o Case 1 (2120 - 2146): complex cumulus o Case 2 (2146 - 2252): anvil in weakening line of convection o Case 3 (2252 - 2347):
010618	2007 - 2220	o Debris	o Case 1 (2032 - 2203):
* 010623	1816 - 2008	o Debris	o Case 1 (1824 - 2006):
010624	1757 - 2027	o Anvil	o Case 1 (1804 - 2024): Tornado occurred
010625	1920 - 2220	o Anvil o Anvil	o Case 1 (1952 - 204810): Decaying anvil o Case 2 (204820 - 2215): E calibrations at low altitude below anvil from earlier storm.
010627	1434 - 1733	o Convective o Anvil o Anvil	o Case 1 (1450 - 1457): o Case 2 (1457 - 1615): o Case 3 (1615 - 1732): Another part of the cloud system and probably has a different anvil source.
010628	1917 - 2127	o Thick o Thick	o Case 1 (1925 - 2032): no convection o Case 2 (2032 - 2125): E calibrations over SLF below same system.

* On dates 000604 and 010623 the times from the raw Citation flight level data were off by 2 hours and for 010217 by 5 hours. The times recorded here are the corrected times.

See Section 3.2 for a description of the different cloud categories: anvil, debris, convective, thick cloud and stratiform.

3. ANALYSIS APPROACH FOR INDIVIDUAL FLIGHTS

A natural first step of analysis was to examine the radar and airborne measurements from each flight to determine the type(s) of cloud or storm in which the aircraft flew on a given day. The results of such analysis are those displayed in Table 2.1 that shows a wide variety of types. But before this detailed analysis could be done it was necessary to process and display both the airborne and radar measurements and place them into a coordinated framework. Early display products of the airborne measurements were separate plots of individual parameters such as altitude, temperature, particle concentrations and electric fields. Examples of such plots for some parameters are presented on the ABFM WEB site. The ABFM Web site developed at NCAR and various products and plots are described in Appendix H.

The WSR74C radar located at Patrick Air Force Base was the primary source of radar observations, because it is dedicated for KSC operations. Analysis was also performed using the Melborne Florida NEXRAD WSR88D, 10cm radar observations. In order to display vertical and horizontal cross sections of the 74C or NEXRAD radar observations it was first necessary to process and grid the raw data. The processing, gridding, display and issues with the 74C and NEXRAD radar data are described in Appendices D and E, respectively. The raw radar measurements in range and elevation space were converted to Cartesian space on a 1 km grid both vertically and horizontally using SPRINT software. See Appendix D for more details. Minimal interpolation or filtering of the raw data was done in order to try to preserve the spatial resolution of the raw measurements. Both radars have gaps between consecutive elevation sweeps (referred to herein as scan gaps), at higher elevation angles. This issue is discussed more in Appendices D and E. Processing, gridding and early production of the 74C CAPPIs was done at NCAR and at MSFC by Monte Bateman for the NEXRAD radar**.** CAPPIs were created for each 1 km of altitude (MSL) using the NCAR software CEDRIC and for each volume scan (every 2 ½ min for 74C and 5 min for NEXRAD) from roughly 2 hrs before aircraft takeoff to about 1 hr after landing. The gridded radar volumes have been copied onto CDs and are available through the KSC Weather Office. Early analyses used individual CAPPIS displayed at 4, 7 and 10 km MSL with the aircraft track overlaid. These early 74C CAPPIs can be viewed for each day at the ABFM Web site by clicking on Link 16. See Appendix H for additional information.

It quickly became apparent that given the wealth of measurements a method was needed to display airborne and radar observations together. There also was a need to make these display products available to all participants at different institutions so that all members of the team could participate in analysis. As a result NCAR developed the ABFM Web site with the goal of not only displaying the measurements but also making the plots and many of the data sets available to participants (within the disk storage space limitation of the Web server). This Web site has now evolved into a powerful analysis and display tool and is described in Appendix H. As this report is being written the ABFM Web site is being transferred to a server at NASA Kennedy Space Center.

To meet the need of being able to view vertical sections of the radar and key airborne observations on the same plot the MER (Microphysics, Electric fields, Radar) software was developed using the Interactive Display Language (IDL). Likewise plots were developed using IDL to show CAPPIs at 4, 7 and 10 km on the same image frame with overlay of aircraft track and, if desired, lightning observations from LDAR and CGLSS. To aid in examining the evolution of the storm structure JAVA applets were developed so that sequential plots of various products including MER and CAPPI images could be viewed rapidly via animation.

3.1 An example: The June 13, 2000 Anvil Case

As an example of analysis that was performed for each flight, a discussion and presentation of plots for the 13 June 2000 case is presented in this sub-section. Only the NEXRAD radar data were available for this day. On all other flight days, except Feb. 10, 2001 when the aircraft was flying near Jacksonville, data are available for the 74C. NEXRAD radar data are available for all days except for June 24, 2000, June 25, 2000, and Feb 17, 2001.

The aircraft investigated the June 13th storm for over 3 hours. For the first 2 hours reciprocal passes were made from east to west through the anvil at roughly 50 to 75 km from the storm core. The storm produced lightning throughout this period. Then after lightning ceased in the storm, reciprocal passes were made from northeast to southwest along the axis of the anvil. Figure 3.1 presents a composite CAPPI plot with lightning overlaid for one of the east-west passes from 2104 to 2110.

In addition to this example of CAPPIs at 4, 7 and 10 km, the evolution of the radar structure of the storm and the flight of the Citation in the storm can be viewed in animation on the ABFM Web site by going to the ABFM Home Page at http://box.mmm.ucar.edu/abfm. On the left side of the ABFM Home Page is a vertical listing with links for all flight days. Click on June 13, 2000. This brings up the Daily Web page for June 13th showing links to various display products and data. To use the applet that animates NEXRAD CAPPIs without lightning click on Link 7 or for CAPPIs with lightning overlaid click on Link 8. The user can select a specific CAPPI or specific periods to examine in the right window and can move forward and back in time with buttons on the top of the window display. Only NEXRAD data were available for this day but for most other days both 74C and NEXRAD data can be viewed with these applets.

Similarly, the evolution of lightning in and near this storm can be viewed by clicking on Link 12 on the June 13, 2000 Daily Web page. The lightning display for the 10 min time period 2100 to 2110 surrounding the CAPPIs of Figure 3.1 is shown in Figure 3.2.

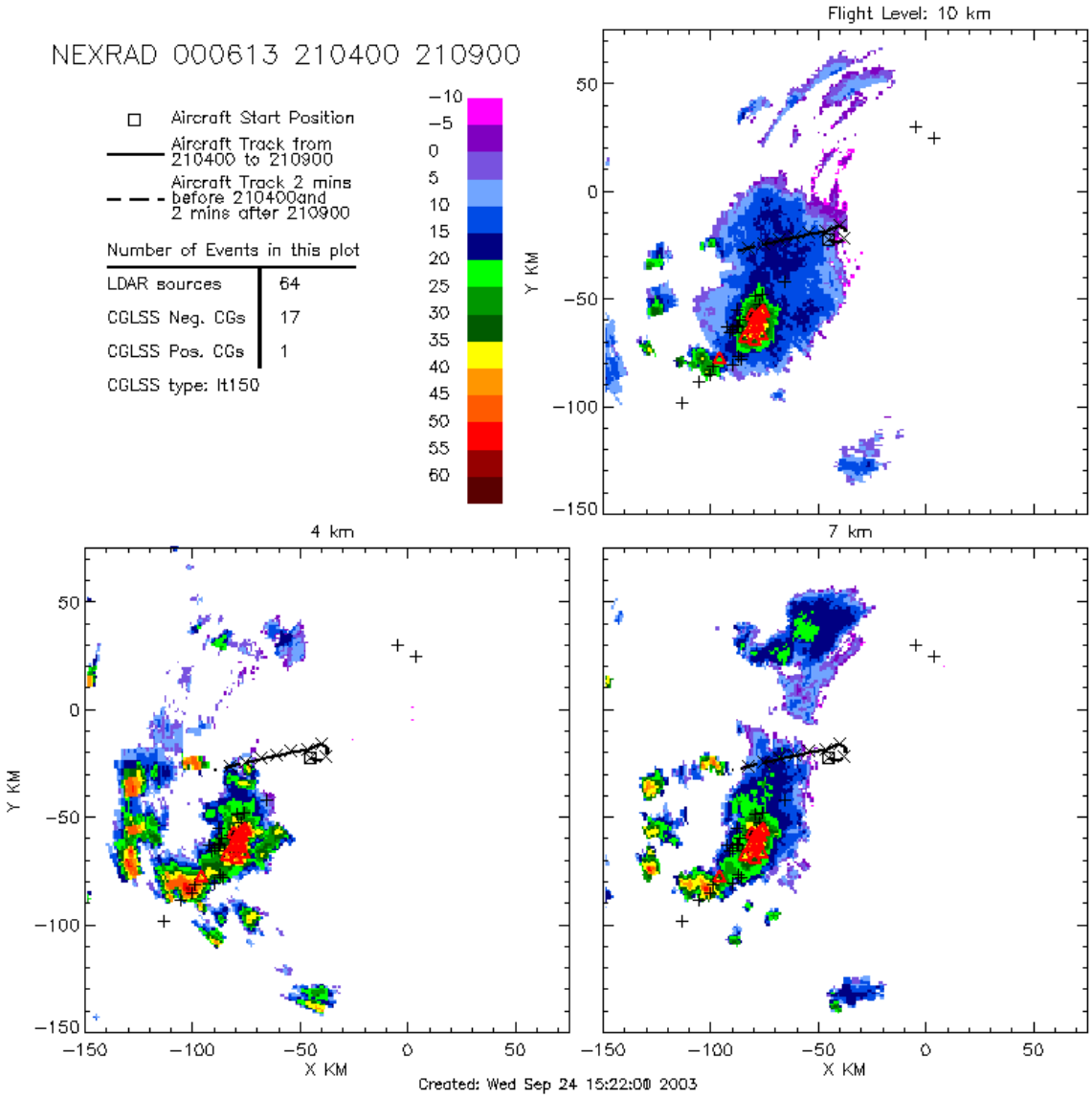

Figure 3.1 CAPPIs at 4, 7 and 10 km MSL showing the Citation track for the period as indicated. CG flashes detected by the CGLSS system are overlaid as red triangles and LDAR VHF sources as black pluses for the period of this volume scan (2104-2109). This storm was ~150 km from LDAR so the detection efficiency was low.

As the aircraft flew from east to west it flew from the edge of the anvil into regions of higher reflectivity with precipitation extending to the ground near the western end of the track. The vertical structure of reflectivity along the aircraft track along with measurements of particle concentrations and electric fields is shown in Figure 3.3, one of our MER plots (Microphysics, Electric Field and Reflectivity) for the period 2100 to 2110. The period from 2100 to ~2102:30 is the end of an east-bound pass. Additional MER plots for different time periods on this day can be viewed by going to the June 13 Web page and clicking on Link 6 -- the applet or directory for NEXRAD MER plots.

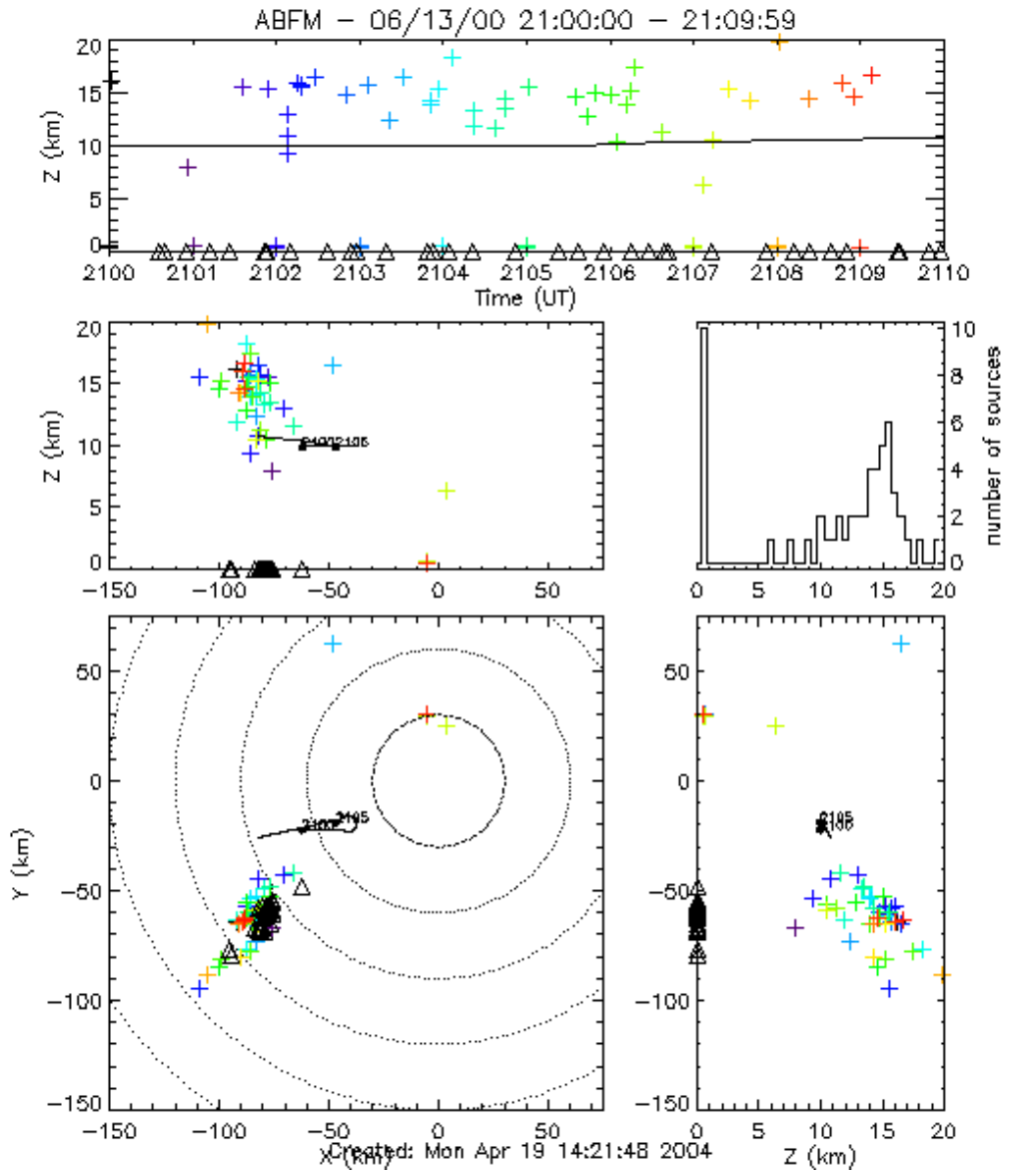

Figure 3.2 Top panel: Display of VHF sources detected by LDAR at the given time (color coded) and altitude. The triangles at the base shows the time of occurrence of CG flashes detected by the KSC CGLSS. The panel on the lower left shows the X,Y location relative to the WSR74C radar of LDAR sources and CG flashes detected during this 10 min time period. The panels above and to the right of the XY display show VHF sources and CG flashes in a XZ and YZ presentation. Track of the aircraft during the 10 min time period is overlaid. For more information on the LDAR and CGLSS systems see Appendices F and G, respectively.

Figure 3.3 illustrates how the electric field can increase dramatically as the aircraft enters regions of reflectivity >~10 dBZ at ~2107. Emag increases from~ 3 kV/m to ~20 kV/m in ~10 s (~1200 m). Unlike the abrupt increase for electric field, the concentration of particles in various size ranges (top panel) increase without abrupt changes as the Citation flew from the edge of the anvil towards the more dense anvil then out the other side. This big increase in electric field is a common feature of the ABFM measurements.

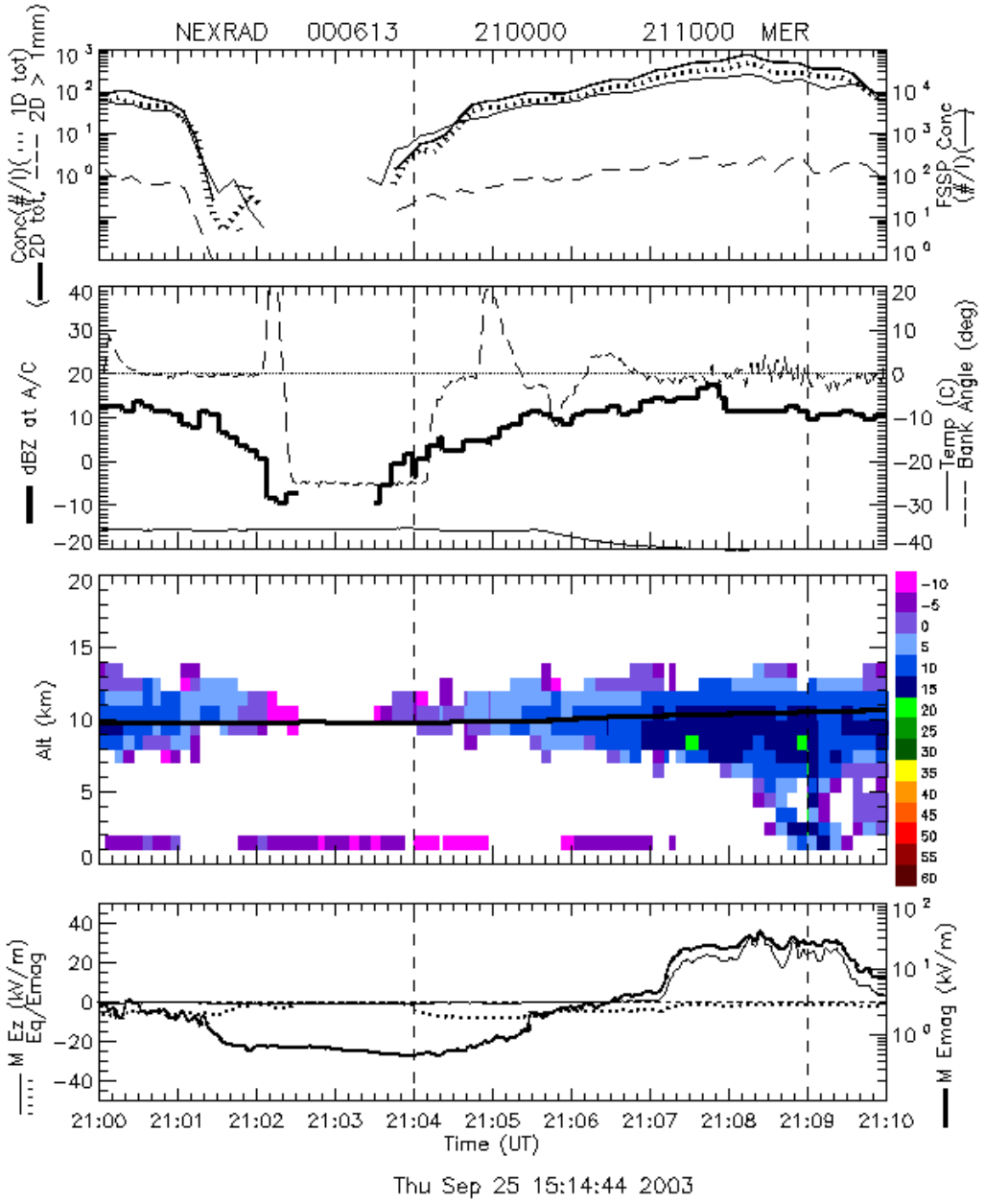

Figure 3.3 Top Panel: Particle concentrations measured by: The PMS FSSP (1 to 48 μm), light, solid line = total conc. on right scale; The PMS 2D-C (30 μm to ~3 mm), bold = total conc., dashed = conc. >1 mm on left; The PMS 1D-C (15 to 960 μm), dotted line = total conc. on left. **Second panel:** Reflectivity at the location of the aircraft, bank angle of the aircraft and ambient temperature. **Third Panel:** The curtain of radar reflectivity in the 1x1 km column above and below the aircraft, in this case from the NEXRAD radar; bold line = aircraft altitude. **Bottom panel:** Vertical component of the electric field, M Ez, light line on left on a linear scale; Eq/Emag dotted on left scale (Eq = apparent field due to charge on the aircraft; Eq/Emag is an indicator of the reliability of the electric field measurement); M Emag, the resultant vector field determined from the M matrix solution, bold line on the right on a log scale. The dashed vertical lines running from top to bottom are time boundaries of individual radar volume scans used to produce the vertical section. For the 1o min period of this plot 3 separate volume scans were used.

Note that the sharp increase in electric field occurs almost a minute before the aircraft passes over precipitation reaching the ground. One minute corresponds to ~7 km at the flight speed of the Citation. As the Citation continued flying toward the western edge of the anvil, reflectivity, particle concentration and electric field decreased.

The three components of the ambient electric field, Ex, Ey, Ez, and Emag, the absolute magnitude of the electric field, are shown for this same time period in the first four panels of Figure 3.4. The X component is along the fuselage of the aircraft, the Y component along the wings and the Z component is vertical in a right handed coordinate system. A positive field is the direction in which a positive charge will move. Electric field plots for other time periods can be viewed on the June 13th Web page by clicking on Link 13.

The traces in each panel contain the external electric field derived from the field mill measurements by two different techniques, the M matrix and the K matrix approaches. The bottom panel of the figure shows Eq, the equivalent field due to charge on the aircraft, determined from the M approach and "K Slack", a parameter used in the K approach to show residuals unaccounted for in the K approach. After considerable scrutiny and examination by personnel at MSFC, the M matrix approach was determined to be much more reliable, primarily because the K approach sometimes does not correctly account for charge on the aircraft. In this report all reference to electric fields and all plots showing electric fields (other than time series plots of electric field, such as Figure 3.4) will be those extracted using the M matrix approach. For more information on the electric field measurements and a description of the M matrix approach see Appendix B. Field Mill calibration is also discussed in Citation Field Mill Calibration, D. Mach and on the ABFM Report Page. The K matrix approach is described in Koshak et al. (1994).

During the time period shown in Figure 3.4 the Ez component of the electric field is dominant. Both Ey and Ex contribute somewhat to the total resultant field, but the contributions are small. The dominance of the vertical component of the field was found to be true in almost all of the anvil penetrations even when a penetration was made quite close to the storm core.

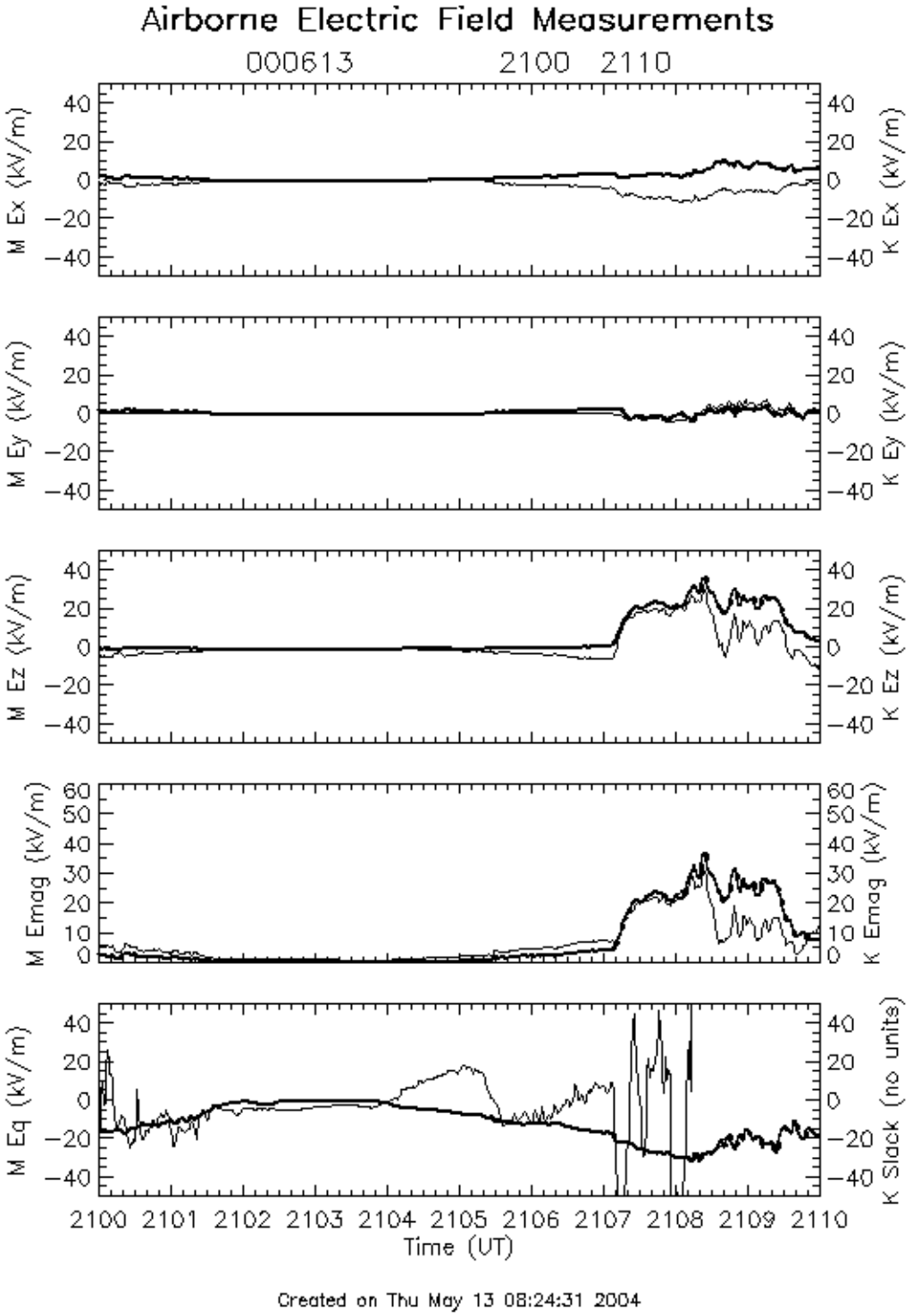

Figure 3.4 First four panels: the Ex, Ey and Ez electric field components (relative to the aircraft attitude) and the magnitude of the total electric field as determined from the M matrix solution (Bold line and left axis for all) and the K matrix solution (light line and right axis). Bottom panel: M_Eq, field due to charge on the aircraft from the M solution and K slack, residuals from the K solution.

Particle concentrations from different sensors and for different size ranges for this same time period are included in Figure 3.5. Plots for other time periods can be viewed via Link 14 on the Web page for this day. The concentration from all probes and in all

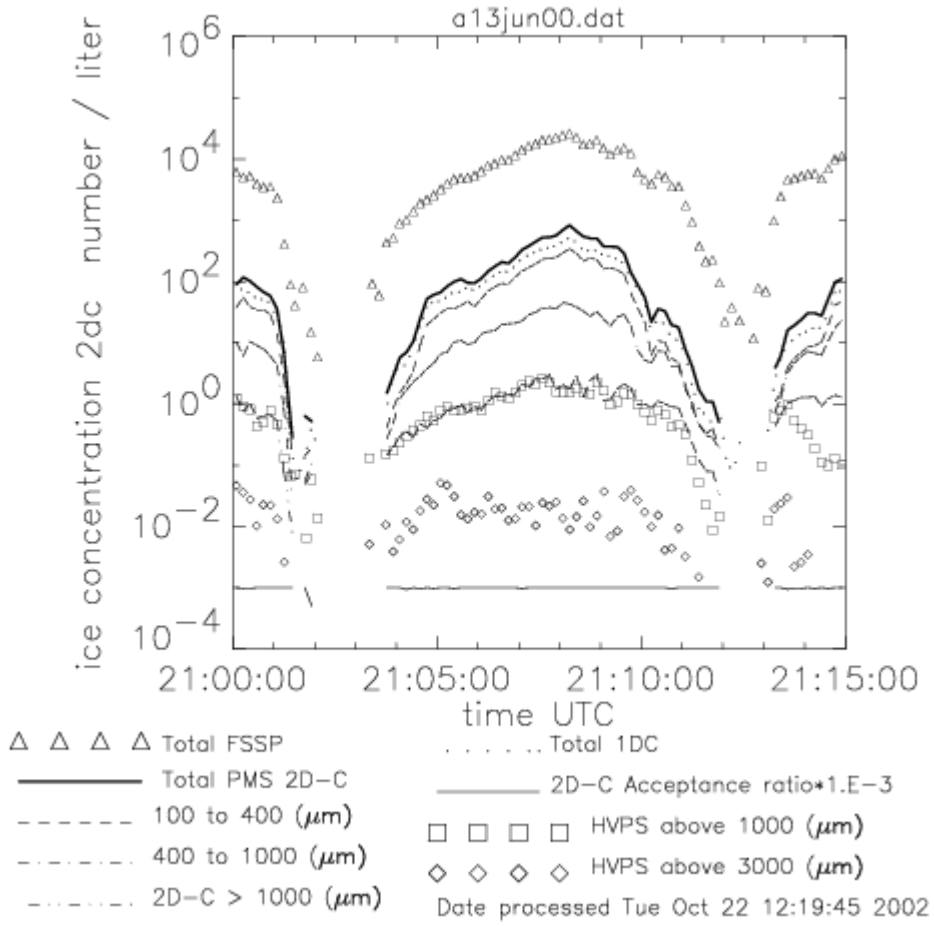

Figure 3.5 Time series plots of 10 second average values of particle number concentration for different probes and size ranges as indicated.

size ranges increase from 2104 to ~2109 as the aircraft approaches the higher reflectivity within the anvil and then decreases more rapidly as the aircraft flies toward the edge of the cloud on the west side. The relative increase in concentration is larger for the smaller particles (shown by the FSSP and the total concentration of the 1-DC and 2-DC probes) than for the larger particles (shown by particles > 1 mm from the 2DC and HVPS probes). Note that mm-sized particles exist even near the anvil edges. The quality of the microphysical measurements during ABFM was in general very good throughout most of the project. This figure shows excellent agreement between the 2DC and HVPS for particle >1000 μ. Even though the agreement for this time period is good, the HVPS sometimes performed marginally during the 2000 campaign. See Appendix C for descriptions of each of the probes and of the uncertainties in the microphysical measurements.

Even though this pass of the Citation is moderately close to the core of this storm (Figure 3.1) at a time that it was still producing lightning, the Rosemont Icing Detector showed no evidence of supercooled water being present. All anvil cases were examined for evidence of the presence of any supercooled liquid water in these anvils, but none was found. (MS Thesis UND, Schild, 2002). During penetrations of a few storm cores some supercooled liquid water was found so we have confidence in the ability of the Rosemont probe to detect supercooled liquid water if it is present. The absence of supercooled liquid water implies that the non-inductive charge separation process was unlikely to be occurring to any significant degree in these anvils.

Particle size distribution plots shown in Figure 3.6 illustrate both the agreement between the different probes as well as more details of the size distribution.

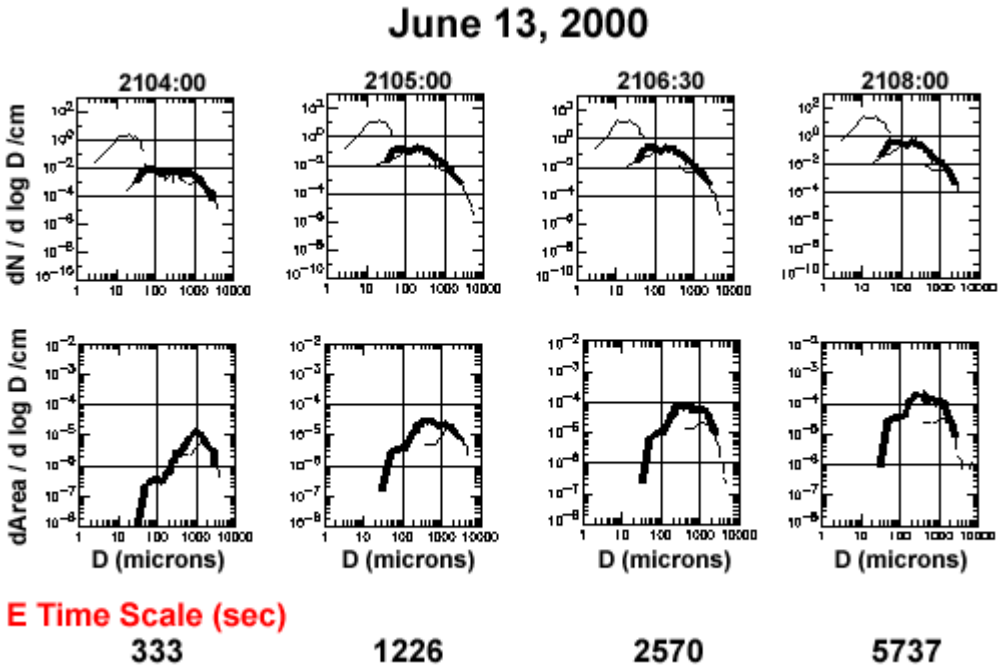

Figure 3.6 Top panel: Concentration size distributions (30 sec averages) for the indicated initial times during the Citation pass shown in Figure 3.1 and 3.3. **Bottom panel**: Particle cross sectional area size distribution for the same 30 sec time periods. Light line on the left side of each plot -- FSSP (off scale for area plots); Bold line – 2D-C; light line on right of each plot -- SPEC High Volume Particle Spectrometer, HVPS, (~400 μm to ~5 cm range).

As noted for the particle concentration time series plots, successive size distributions show increases in concentration over the entire size distribution as time progresses reaching a peak at 2108:00 to 2108:30 when the Citation was flying in higher reflectivity. Size distributions for other time periods are available via Link 15.

Examples of images (shadows) of particles measured by the PMS 2-DC probe are shown in Figure 3.7 for the time period 2105:53 to 2110:28, the time period of the Citation anvil penetration shown in Figures 3.1 and 3.3. Each row of particle images corresponds to one

buffer of data recorded by the 2-DC. 2D particle images can be viewed for each flight day of the June 2000 or May/June 2001 on the ABFM Web site. Go to:
http://www.mmm.ucar.edu/abfm/webpage/2-DC_Images
Select the year of interest, 2000 or 2001, then the flight day of interest. This brings up a list of frames from that flight in sequential order. Only 1 out of every 100 buffers is shown, hence the time gap between buffers in Figure 3.7. Images such as these are used to derive the particle number and area size distributions for the 2DC probe.

The first buffer in Figure 3.7 shows relatively more medium sized particles compared to buffers near 2108, because statistically there were more small particles than large near 2108 even though the concentration of large particles at 2108 was more than at 2105.

Figure 3.7 Buffers of particles imaged by the 2-DC probe. The vertical dimension of each row is ~ 1mm. Text across the top of each buffer designates flight day (M/D/Y); start time of first image in that buffer (row); start time of last image in the buffer; DeltaT: = elapsed time to fill the buffer; TAS = true airspeed of the aircraft. The TAS is used to determine the horizontal particle size.

The higher size resolution images from the Cloud Particle Imager (CPI) shown in Figure 3.8 illustrate the characteristics of the particles found in ABFM anvils. These selected images are for the time period 2151 to 2152 in a region in and near strong electric fields.

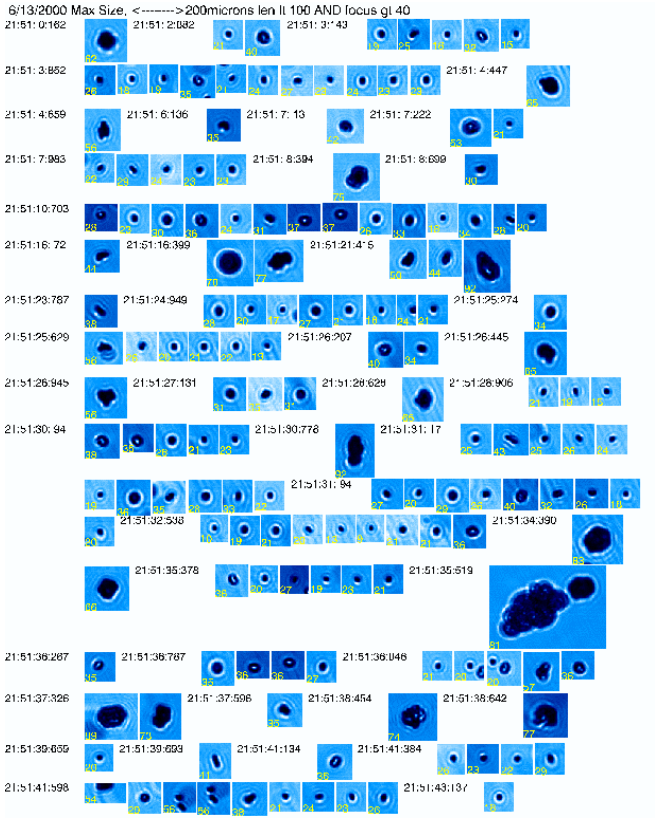
6/13/2000 Max Size, <-------->200microns len lt 100 AND focus gt 40

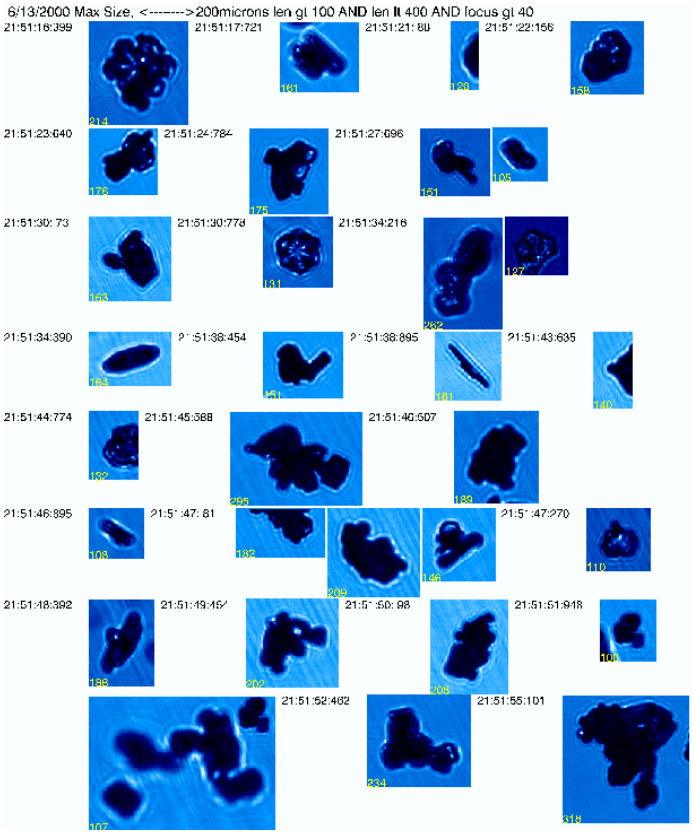
6/13/2000 Max Size, <-------->200microns len gt 100 AND len lt 400 AND focus gt 40

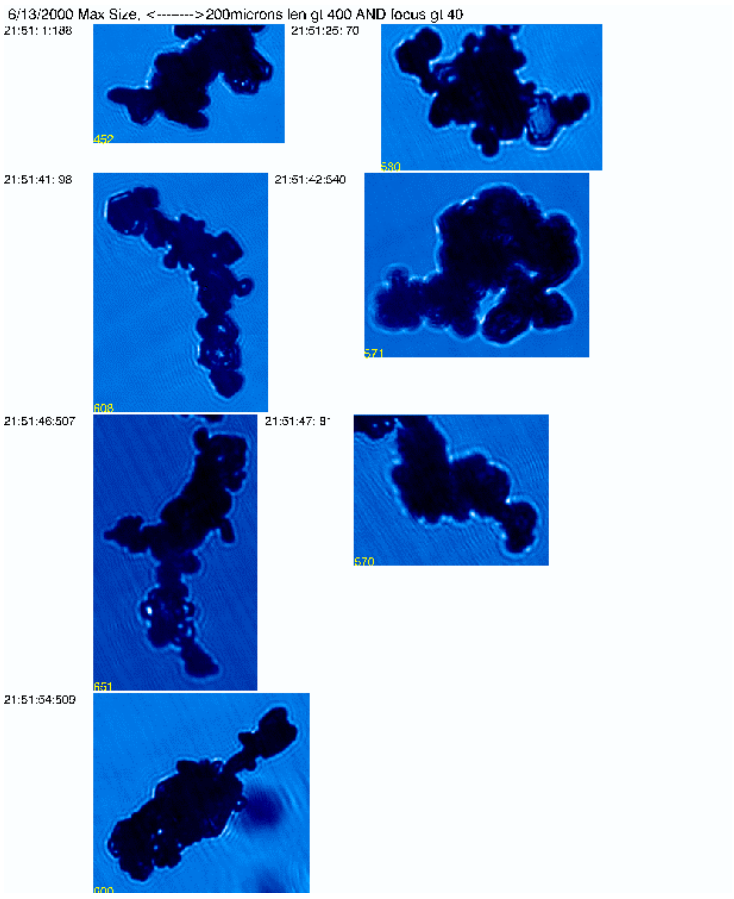

Figure 3.8 A, B and C from top to bottom. **A)** Particles < 100 µm. The smallest image in this frame is ~15 µm and the largest image is ~80 µm. **B)** Particles between 100 and 400 µm. The largest particle (on the lower right) is ~320 µm. **C)** Particles > 400 µm. The largest image is ~650 µm.

Analysis of the CPI images for several days by Paul Willis shows that most of the smallest particles appear to be frozen cloud droplets along with other irregularly shaped particles. The intermediate sized particles in this figure have irregular shape but a few appear to be plates imaged face-on or from the side. The largest particles in this example are long, highly irregular aggregates. Some of them are quite linear suggesting that strong electric fields aided the aggregation process. These long, linear aggregates were observed fairly frequently, but not always in regions of strong electric field. Once formed, sintering between the aggregated crystals can rapidly form a strong joint, allowing them to be carried downstream for long distances while maintaining this same basic shape.

Cross-sectional area distributions are shown along the bottom of Figure 3.6. These areas were determined from measured cross-sectional areas of individual particles, such as in Figure 3.7, by summing shadowed diodes (see Appendix C). The area in the 200 to 2000 µm size range progressively increases with time in this figure. The impact of the area distributions on the rate of decay of the electric field as determined with John Willett's simple anvil model (Willett, 2001 and 2003) is discussed below in Section 6. The E decay time scales (estimates of the time taken to decay linearly from an initial electric field of 50 to 0 kV/m assuming the "high limit" conditions) calculated from the model for

each of these area distributions is shown at the bottom of the figure. See Willett (2003) for details. On the edge of the anvil the time for this decay is a little more than 5 min while in the dense part of the anvil the time is > 1 ½ hr. Thus, the rate of decay is very dependent upon the particle size distribution, particularly of particles in the 200 to 2000 μm size range.

Figure 3.9 displays the particle cross sectional areas as a function of time for different particle size categories. The areas in these size categories are based on integration of specific portions of the detailed size distributions such as those of Figure 3.6. The largest contribution to accumulated area is for particles in the size range 200 to 1000 μ.

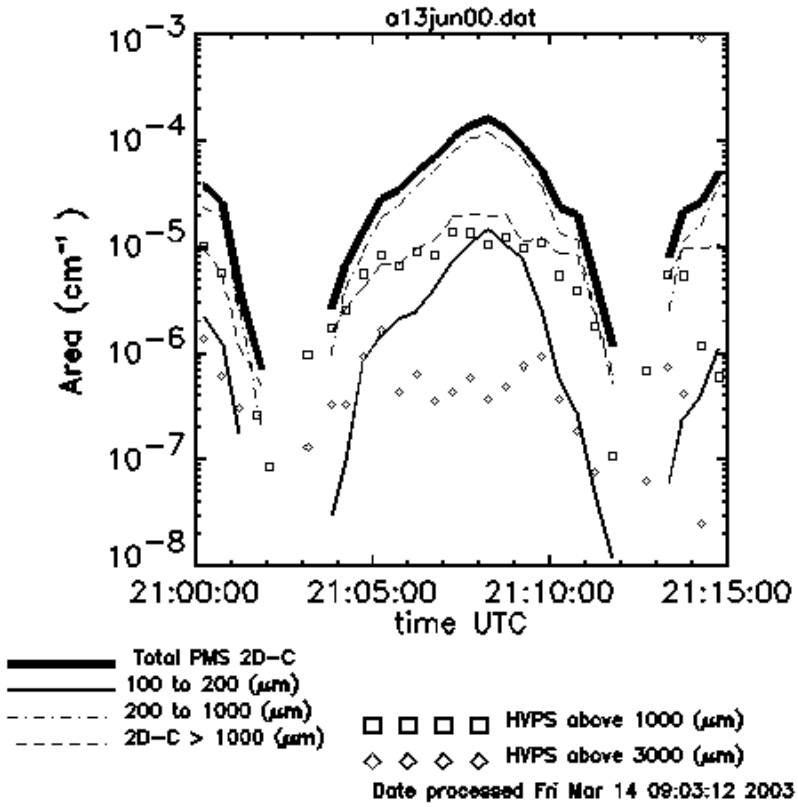

Figure 3.9 Time series plot of 30 second average values of particle cross sectional area for different probes and size intervals as indicated.

Towards the edges of the anvil (~2104 and 2111) the contribution from particles >1000 μ is almost comparable to the area of those particles 200 to 1000 μ. Note that the size categories for the time series area plots are different than those for the time series plots of particle number concentration in Figure 3.5. Time series plots of number concentration such as Figure 3.5 use 2DC categories of 100 – 400, 400 – 1000, and >1000 μ, whereas in the time series plots of area such as Figure 3.9, size categories of 100 – 200, 200 – 1000, and >1000 μ were used. The separation at 400 μ was selected for our initial analysis and display of number concentrations because this is the approximate size at

which riming of cloud droplets begins to occur on ice crystals. However, after examination of the area distribution plots for the electric decay time studies, it became apparent that a significant amount of particle area was contained between 200 and 400 μ and 200 μ would be a better separation for the area time series plots.

After lightning had ceased in the storm slightly before 2200, we started making passes along the axis of the anvil with and against the wind. The southern most part of two of these passes from the downwind tip of the anvil into higher reflectivity remnants closer to the storm core are shown in Fig. 3.10. The maximum reflectivities at the aircraft altitude

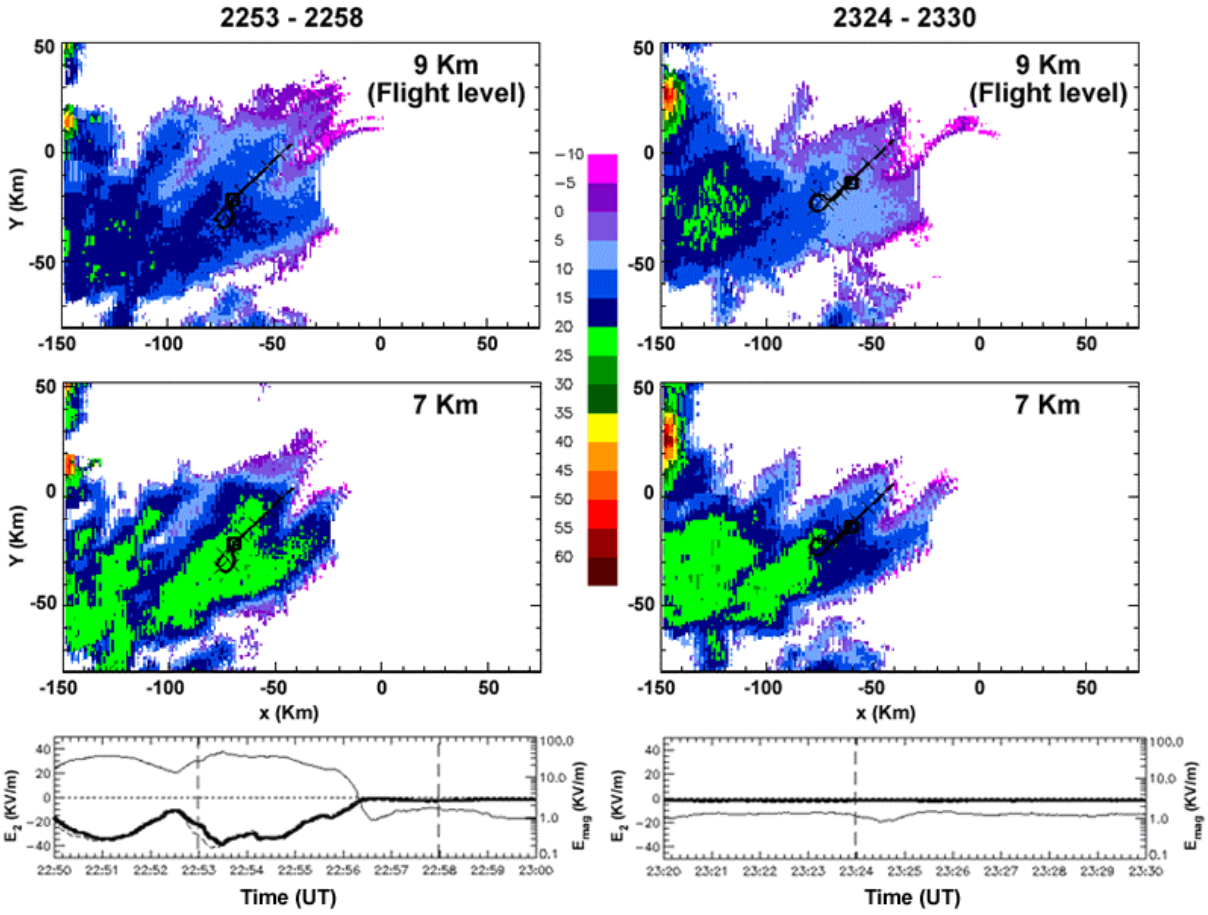

Figure 3.10 CAPPIS at 7 and 9 km for periods as indicated with 9 min of aircraft track overlaid (left: 2251 to 2300 and right: 2332 to 2341). Squares show start of track. **Lower Panels**: Ez, (bold line, left scale) and magnitude of total field, Emag, (light line, logartithmic right scale) for the periods 2250 - 2300 and 2320 – 2330. In this plot Emag is a light solid line, not the bold line used in MER plots.

were 14 to 17 dBZ from 2253 - 2258 and 12 to 15 dBZ from 2324 – 2330. From the vertical structure of the reflectivity along the aircraft track shown in the MER plots of Figure 3.11, we see that the reflectivity below the aircraft was greater for the first pass than for the second. In both passes the aircraft is above the altitude of maximum reflectivity.

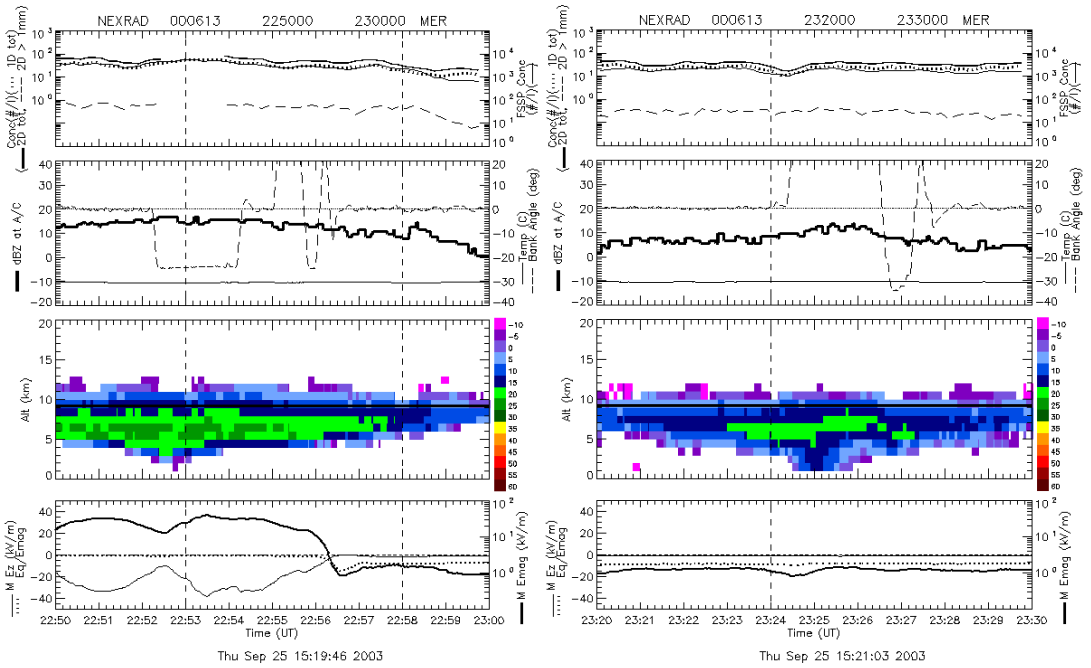

Figure 3.11 MER plots corresponding to the two passes show on CAPPIs in Figure 3.7.

The maximum electric fields observed during the first pass were 39 kV/m at 2253:30. During the second pass the electric fields had decreased to a maximum of 1.5 kV/m at 2325:30, a decay of 37.5 kV/m in 32 min (1920 s). By comparison the maximum in the calculated E time scale, $\tau_{E,}$ for the decay from 50 kV/m was 1711 s for the period 2253:30 to 2254:00. Using this time scale we calculate via equation 5) of Willett and Dye, (2003), a time of 1275 s for the electric field decay from 39 to 1.5 kV/m based on the 30 s average particle size spectra observed at 2253. In this case the model decay is consistent with the observations.

In summary for the June 13, 2000 case the anvil was investigated starting at a time when lightning was occurring frequently in the core to the time that the storm had dissipated and electric fields in the anvil had decreased to values <2 kV/m. This is one of the better cases investigated during ABFM but it exhibits characteristics typical of the other anvil cases and even debris clouds. Even when strong fields existed in the denser parts of the anvil, as the aircraft leaves reflectivity and approached the edge of the anvil, electric fields dropped to low values of 1 kV/m or less. These decreases in field strength are often abrupt, much more so than the decreases in particle concentration. Particle concentrations in all size ranges decrease as the aircraft flew to the anvil edge.

3.2 Classification and Lists of Different Storm Types

In following sections we explore the relationships between reflectivity, particle concentrations and sizes and electric fields for the ensemble of ABFM measurements. Before moving to other sections we wish to point out some information that is available for each flight day on the ABFM Web site. For each flight day there is a Daily Home

Page containing Links to various data displays and also data files such as those described for the June 13th case above. See Appendix H.

Near the top of each Daily Home Page there is a Synthesis Link that shows summaries and analyses done for that day, a Weather Summary for that day, the Citation Flight Track and Brief Notes pertinent to that day (sometimes the content overlaps with the synthesis). At the top of each of these Syntheses there is a Summary Table for each case on that day. This table shows the time period of the aircraft investigation of this case; the type of case; complexity; degree of convective activity; approximate location (usually of the core); estimate of storm motion; and a brief verbal description of the case. It also presents some statistical information on electric field, and particles. These statistics give a sense for the case but for most of the flights the variability is large, so average values tell only part of the story. Any analysis that has been written up for this flight day follows after the Summary Tables in reverse chronological order.

Near the bottom of the Daily Home Page there is a Link to the "MERGED" data files for both the 74C and NEXRAD. These MERGED files contain 10 sec averages of aircraft measurements of aircraft position and attitude, state parameters, microphysics and electric field time synchronized with various calculated reflectivity parameters. They are an important source of measurements for any analysis to be undertaken. There are also links to other measurements included the 1 s averages of the electric field measurements, LDAR and CGLSS lightning data, both 10 s and 30 s averaged particle measurements, KSC profiler and Rawinsonde measurements, and the Citation flight level data from the Univ. of North Dakota processing.

We have used the above information and tools on the Web site to examine each flight and have separated and listed each case into different categories: anvils, debris, convective, thick clouds, and stratiform. Table 3.1 gives a list of all anvil cases including times and a few words regarding the stage of decay. Similar information is provided for all debris cases in Table 3.2, for thick clouds in Table 3.3 and stratiform cases in Table 3.4.

Often there is ambiguity between the different cloud types. But for the purposes of separating and listing the cases in these tables we have used the following general guidelines. The classification of types for each day was determined by following the evolution of the storm using the CAPPI and MER plot displays.

Anvils are formed by divergence at the top of a convective core or by transport of material from the convective core(s) due to upper level winds. For our "In-Anvil" category a cloud was considered an anvil only if the cloud in question had a definable base without precipitation reaching the ground.

Convective generally meant that reflectivity of 35 to 40 dBZ or greater was evident on the 4 and/or 7 km CAPPIs with distinct cellular structure. Often lightning was occurring in the cell or nearby.

Debris clouds were considered to be cloud remnants from once active thunderstorms that grew in a low shear environment after strong cellular structure was no longer evident and lightning had stopped. The resulting radar structure at 4, 7 & 10 km tended to move as a block and remain vertically stacked with no obvious anvil formation. We also included stratiform regions that formed behind or adjacent to once active storms as debris clouds. Sometimes these regions advected over KSC from earlier deep convection to the west or east.

Stratiform clouds covered extensive regions (usually trailing the main system) without strong deep convection. They usually were attached to or formed by deep convective systems. Sometimes they moved into the area from earlier deep convection.

Thick Clouds were layered clouds, some part of which was in the 0 to –20C temperature zone. Precipitation might or might not be reaching the ground. The cases in Table 3.3 are ones that were distinctly thick clouds, but some cases in the debris or stratiform categories could also be considered as thick clouds.

There is ambiguity in trying to distinguish between debris, thick-layered clouds or moderate wide spread convection, such as a stratiform layer and even anvil. Operationally it is not feasible to uniquely categorize most clouds during convective weather. Most thunderstorm-derived clouds away from the core may have simultaneous characteristics of anvil, debris and thick-layered cloud. Operationally, all applicable rules are applied to the same cloud, and the most conservative result is used. But for the purpose of understanding the behavior of different kinds of systems and the relationship of electric field with reflectivity, it is useful consider the different types within the ABFM data set.

TABLE 3.1
LIST OF ANVIL CASES

Date/Type	Times		Comments
000604	2006 - 2340		
o Anvil	2059 – 2302	high E	Aircraft flew near cores but also near anvil edge.
000607	1755 – 1907		
o Anvil	1755 – 1907	low E	Mostly convective, some moments in anvils.
000611	1758 – 2000		
o Anvil	1810 – 1826	low E	Cell is in decay.
o Anvil	1828 – 1858	low E	Aircraft flew on the edge of a decaying anvil.
o Anvil	1901 – 1955	low E	This anvil was close to generating convection.
000613	2016 – 2424		
o Anvil decay.	2045 – 2405	mod E	Early stages of anvil development through
000614	2058 – 2424		
o Anvil	2127 – 2158	low E	Decaying anvil with no generating convection.
o Anvil	2212 – 2409	hi à low E	Good case for studying anvil decay.
000625	1702 – 1817		Cabin pressure lost at ~ 1730.
o Anvil	1730– 1811	low E	Below the anvil at 1.5 km MSL.
000628_2	1809 – 2135		
o Anvil	1815 – 1837	low E	Spiral up through anvil.
o Anv & Conv	1837 – 2000	mod E	Anvil only during turns, mostly convective.
o Anvil	2003 – 2118	mod E	Mostly close to a core, not a good anvil study.
010525	1829 – 2213		
o Anvil	1853 – 1913	mod E	A small anvil on the northern edge of a line.
o Anvil	2028 – 2200	low E	Aircraft was flying close to convection.
010527	2125 – 2437		
o Anvil	2135 – 2201	low E	Early stage of developing anvil.
o Anvil	2201 – 2222	low E	Perhaps anvil of Case 1, but maybe debris.
o Anvil	2222 – 2322	low E	More than one anvil finger, merger with case 2.
o Anvil	2409 – 2422	low E	Anvil associated with decaying cell of Case 4.
010528	1802 – 2202		
o Anvil	1806 – 21120	low E	Passes in an attached anvil cloud above KSC.
010529	1939 – 2248		
o Anvil	2006 – 2231	mod E	Small anvil attached to a long lasting active core

010602	1839 – 2258		Example of intervening precip. attenuation.
o Anv & Conv	1914 – 2238	hi E	Large system, one dominant, intense cell.
010604	1840 – 2314		
o Anvil	1901 – 1908	low E	Precip. going to the ground, but no cores.
o Anvil	1921 – 1928	low E	Anvil,perhaps from the cell of Case 1.
o Anvil	1928 – 2010	low E	Isolated cell, later a detached anvil.
o Anvil	2010 – 2259	mod E	Early anvil formation through decay. Develops large stratiform-like area downstream.
010610	1958 – 2346		
o Anvil	2042 – 2133	mod E	This was flown very close to the source.
o Anvil	2210 – 2311	mod E	To SW of above cell, same system.
010615	2106 – 2406		
o Anvil	2146 – 2252	mod E	anvil in weakening line of convection
010624	1757 – 2027		
o Anvil	1804 – 2024	hi E	Spatial decay of E for intense tornadic storm.
010625	1920 – 2220		
o Anvil	1952 – 204810	low E	Detached anvil in decay
o Anvil	204820 – 2215	low E	E cals over SLF below high anvil
010627	1434 – 1733		
o Anvil	1457 – 1615	low E	Growing anvil with turns near cores.
o Anvil	1615 – 1732	mod E	Another part of the above cloud system.

TABLE 3.2
LIST OF DEBRIS CASES

Date/Type	Times		Comments
000617	1551 – 1724		
o Debris	1604 – 1724	low E	maritime line, southern end weakens over KSC.
000620	2132 – 2349		
o Debris growth.	2150 – 2227	low à hi E	Initially debris from one cell, then new
000623_1	1636 – 1911		
o Debris	1718 – 1744	hi à low E	Decay of small cell. Much larger, active area nearby
o Debris	1748 – 1752	low E	This case never had a strong core.
o Debris	1756 – 1824	hi à mod E	On eastern edge of complex system
000623_2	2050 – 2115		
o Stratiform	2057 – 2110		A ferry flight. E observations, no microphysics.
000624_2	2044 – 2343		
o Debris	2100 – 2113	mod E	Aircraft passed through some debris at takeoff.
o Debris	2113 – 2225	hi E	Some areas of 40dBZ at 4 km, some lightning.
000628_1	1400 – 1511		
o Debris	1404 – 1425	low E	An hour after last lightning.
o Debris	1425 – 1456	low E	Aircraft arrived too late for decay studies.
010525	1829 – 2213		
o Debris	1913 – 1931	low E	There was convection in this area at 1834.
o Debris	1938 – 1944	low E	This might be the debris from case 2
o Debris	1944 – 2038	low E	This is debris from the convective part of case 1.
010604	1840 – 2314		
o Debris	1908 – 1921	low E	Rather small, very close to the radar void.
o 010605	1759 – 2154		
o Debris	1820 – 1846	low E	maritime debris, final decay
o Debris	1853 – 1928	hi E	very active maritime, offshore storm
o Debris	1938 – 2044	low E	advanced decay of once active convection.
o Debris	2044 – 2116	mod E	axial pass, pseudo-anvil of active storm
010606	1733 – 2035		
o Debris	1815 – 1921	low E	This debris cloud is in decay.
o Debris	1921 – 2005	low E	Decaying debris, different cell from case 2
010607	1717 – 2027		
o Debris	1937 – 1950	low E	Passes in Stratiform debris with embedded cells.
o Debris	1950 – 2008	low E	Passes in Stratiform debris with embedded cells.

010610	1958 – 2346		
o Debris	2133 – 2210	hi E	Debris to the SW of the anvil of case 2
010618	2007 – 2220		
o Debris	2032 – 2203	hi E	Small convective near Stratiform. Interesting. sign reversal of electric field

TABLE 3.3
LIST OF THICK CLOUD CASES

Date/Type	Times		Comments
010203	2051 – 2253		
o Thick Cloud	2125 – 2240	low E	Best thick cloud case; no electrification.
010210	2147 – 2417		
o Thick Cloud	2312 – 2345	low E	Very marginal thick cloud near Jacksonville.
010628	1917 - 2127		
o Thick cloud	1925 – 2032	low E	Cloud ~ 4 km thick; temp at A/C ~ --8C.
o Thick cloud	2032 – 2125	low E	A/C below layer doing E cals over SLF.

SOME STRATIFORM CLOUDS PROBABLY QUALIFY AS THICK CLOUDS.

TABLE 3.4
LIST OF STRATIFORM CASES

Date/Type	Times		Comments
000623-2	2050 - 2115		
o Stratiform	2055– 2110	hi E	Short, ferry flight. No microphysics.
000624-1	1637 - 1957		
o Stratiform	~1815 - 1957	hi E	Stratiform with weak convection. Land Orlando.
000624-2	2055 – 2342		
o Stratiform	2100 - 2342	hi E	Takeoff Orlando, Stratif. with weak convection.
010522	2128 - 0035		
o Stratiform	2137 - 0020	hi E	Band of stratiform with embedded convection.
010606	1940 – 2043		
o Stratiform	1810 – 2035	hi to wk E	Decay of weak convective band.
010615	2120 - 2406		
o Stratiform	2250 – 2346	hi E	Embedded convection. Over 74C at times.
010623	1825 _ 2005		
o Stratiform	2250 – 2346	hi and lo E	Behind a long convective line.
o			
010624	1804 – 2024		
o Stratiform	2250 – 2346	hi E	Behind intense convection, on return to PAFB.
010628	1925 - 2123		
o Stratiform	1935 – 2026	mod E	Widespread layer with precip to grnd at times.
o Thick Cloud	2030 – 2125	lo E	E cal over SLF, Thick cloud layer above.

4. ELECTRIC FIELDS, MICROPHYSICS AND RADAR REFLECTIVITY

In the previous section we presented the June 13, 2000 anvil case as an example of one of the better anvil studies. The goal of following sections is to examine measurements from all anvil cases to better understand the relationships between electric field, radar reflectivity and particle concentration and size in the Florida anvils investigated by ABFM.

The first step in this process was to determine times for which the Citation was flying within anvils. To be considered an anvil the cloud in question had to have formed by divergence at the top of the convective core or by transport of material from the convective core(s) due to upper level winds. This was determined by a detailed examination of the evolution of each storm using the CAPPIs and MER plots for each flight day. To be considered as "In-Anvil" the aircraft also had to have been flying in a region in which the anvil had a definite base. Regions in which radar reflectivity appeared to be reaching the ground were excluded from the In-Anvil classification. The list of days and times derived from this analysis are available at the ABFM Web site on the Reports Page via the Link "In-Anvil" Dates/Times as of Sept 4, 2003.

Further filtering of this data for each day was done to eliminate regions in which there was either wet radome or intervening precipitation attenuation of the 74C radar return. These dates and periods are listed on the Reports page of the ABFM Web via the Link Attenuation. Additionally, periods were eliminated when the aircraft was flying in the cone of silence (In Void) above the 74C or NEXRAD radar and for periods when the aircraft was flying at altitudes below 5 km MSL. The resulting data set (also listed on the web site) filtered to remove periods of radar attenuation, In Void, and for aircraft altitudes <5 km is referred to as minimum filtering. Filtering is discussed more in Section 6 where we explore different calculated reflectivity parameters for possible use as a radar-based LLCC. For his final report Willett (2003) produced and utilized a filtered file that he termed "minflt" (ie., In-Anvil with minimum filtering). His composite file was created using the MERGED files of radar parameters and 30 s averaged aircraft measurements available for each flight anvil day on the ABFM Web site. See In-Anvil" Dates/Times as of Sept 4, 2003. For days or periods during which 74C data were missing or periods when the aircraft was in the void above the 74C radar, he used the corresponding NEXRAD data. To be certain that the aircraft was actually flying in anvil he required that the flight level be ≥ 5 km, that the calculated E Decay time, τ_E, be ≥ 20 s and that there be no NaNs (our flag for no data) This yielded a composite data set for all periods during which the Citation was flying In-Anvil. No additional filtering was done to exclude regions with nearby lightning or convective cores, because we wanted to examine all anvil regions containing high electric fields as well as those in decay. We have used Dr. Willett's "minflt" data set for analyses in the following sections to be able to use his model determined E decay parameters and also to extend the results of his work. There were 2189 individual 30 s periods in this data set.

4.1 Electric Fields and Microphysics

Early examination of time series plots of the microphysical measurements in the different anvils showed that there was a lot of consistency of particle concentrations in different size ranges from flight to flight, especially when electric fields were high (≈>10 kV/m). This consistency in anvils is shown in Figure 4.1 in which particle concentrations from different probes or size ranges are plotted as functions of concentrations from other probes or size ranges.

The FSSP responds primarily to small particles. It has a nominal range of 3 to 45 μm for water droplets and a somewhat similar range for ice but with more uncertainty and scatter in sizing. In the presence of numerous large ice particles such as most of our anvil

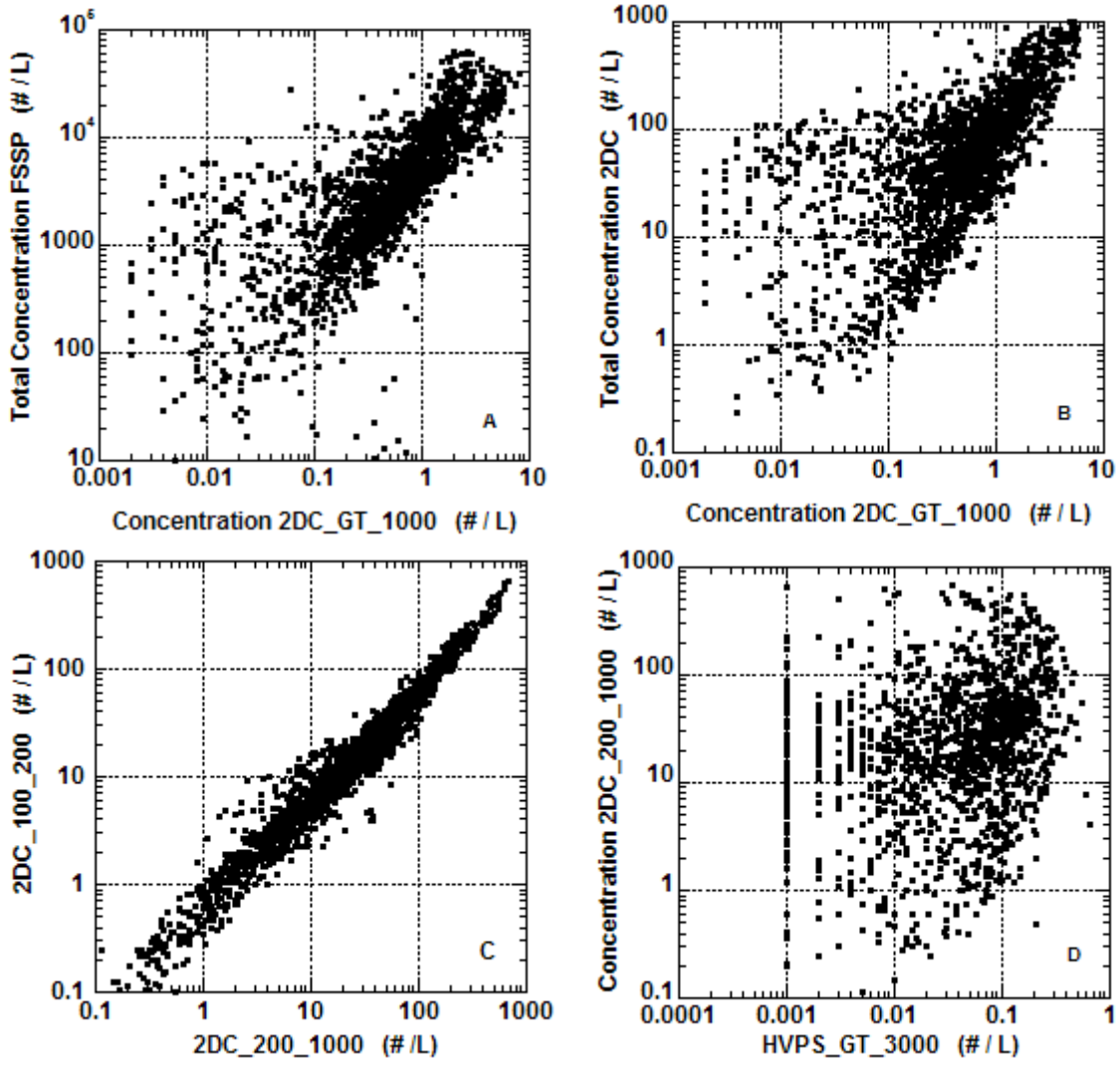

Figure 4.1 **(A)** Total FSSP concentration vs. concentration of particles from 2DC >1000 μ. (**B)** Total 2DC concentration vs. concentration of particles from 2DC >1000 μ. (**C)** 2DC concentration of particles 100 to 200 μ vs. concentration of 200 to 1000 μ. (**D)** 2DC concentration of particles 200-1000 μ vs. HVPS concentration of particles >3000 μ.

observations the concentrations could be as much as a factor of 2 too large due to breakup of the larger particles and possible specular reflections from ice crystal facets. The 2DC probe at the flight speed of the Citation has a nominal range of ~30 μm to a few mm, but seriously undercounts particles <100 μ in size and the sample volume is limited for particles ~>1 mm in size. The total concentration measured by the 2DC is dominated by particles of ~50 to~300 μ in size as seen in Figure 3.6. Measurement in the categories 100 to 200 μ and 200 to 1000 μ are in the optimum size range for measurements with the 2DC. The HVPS can detect and size particles in the size range of a few hundred microns to ~5 cm with an optimum counting and sizing range of ~1 to 10 mm. The upper end is primarily limited by the sample volume for these few, rare large particles. The HVPS operation was sporadic during the June 2000 campaign, but it performed very well during 2001. The good agreement between the 2DC and HVPS for particles >1 mm in Figure 3.6 and Figure 4.2E gives us confidence in the measurements of the larger particles. See Appendix C for additional discussion of the various microphysics probes, limitations and uncertainties. As readily seen in this figure as well as in the number concentration size distribution plots of Figure 3.6, the smaller particles are much more abundant than the larger particles.

Figure 4.1A and B show that the total particle concentrations measured by the FSSP and the 2DC, respectively, are well correlated with the concentration of particles >1000 μ observed with the 2DC, particularly at higher concentrations. As seen in Figure 4.2 the higher concentrations are primarily in regions containing stronger electric fields. Figure 4.1C shows a striking correlation between particles of size 100 to 200 μ and those 200 to 1000 μ. As seen in Figure 3.6 the 200 to 1000 μ sized particles contain the largest cross sectional area and hence are those that most influence the electric decay times, as will be discussed in Section 5. In Figure 4.1D we see that there is a poor correlation between particles of 200 to 1000 μ size and particles >3000μ. The particles >3000 μ in size dominate the radar reflectivity. Because there is a lot of scatter in this figure we should also expect a lot of scatter in the relationship between electrical decay time and reflectivity.

To investigate relationships between Emag and the different particle sizes, scatter plots of Emag versus particle concentration for different probes and size ranges are presented in Figure 4.2 for the minimum filter, “In-Anvil” data set. Although there is substantial scatter the shape of the relationship between Emag and concentration in different size ranges is surprisingly similar in spite of 4 orders of magnitude difference in concentration between the FSSP and those >1 mm from the 2DC and HVPS. For fields >3 kV/m the majority of particle concentrations from a given probe or given size range are within a factor of approximately 3 to 4 from the average value at a given value of Emag.

Probably the most interesting and perhaps surprising feature of these plots is the knee or change of slope at ~2 to 3 kV/m in the Emag vs concentration relationship seen in this log log plots. Whereas for electric fields >3 kV/m up to the maximum of ~45 kV/m there is not much change of concentration with increasing field, for Emag < 3 kV/m there are wide ranges of concentration for relatively small changes of field. This knee seen in the

plots of Figure 4.2 strongly suggests a change in physical processes (or perhaps balance between different physical processes) occurring in the high field and low field regions.

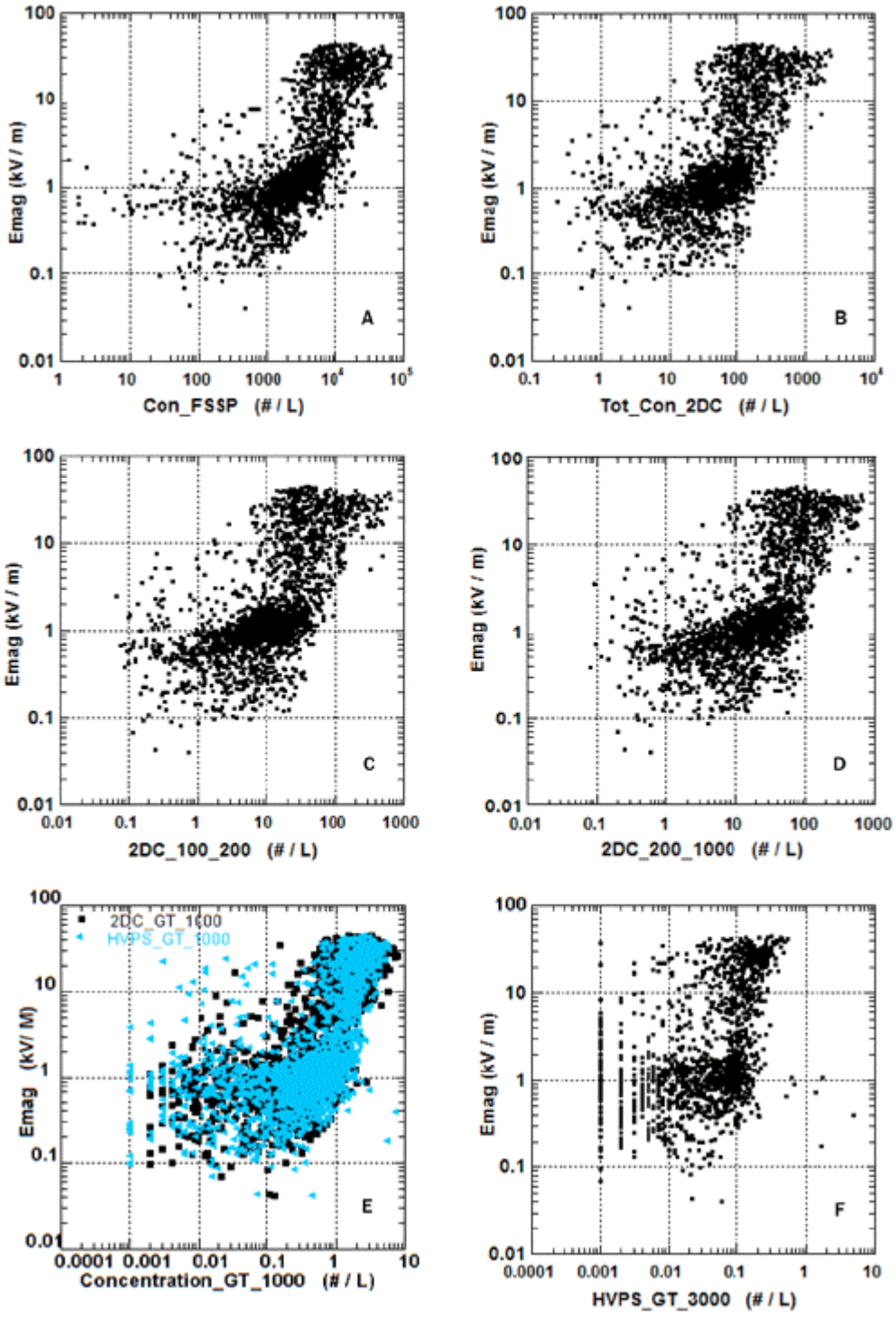

Figure 4.2 Plots of Emag as a function of concentrations measured by different sensors in different size ranges as labeled.

This change in character between regions of high and low particle concentrations may have important implications for the decay of electric field in these anvils. But the reason for this change is not clear. The sides, tops and bottoms of the anvils are primary places that turbulent mixing of clear and cloudy air will occur and hence evaporation of particles. Particle concentration and area will be decreasing significantly in these regions. Because the electrical decay time is primarily dependent upon the cross sectional area of the size distribution, the rate of electric field decay will be increasing in these same regions compared to the main body of the anvil. Is it possible that this shift occurs abruptly, leading to the character seen in Figure 4.2. This seems unlikely for as we see in Figures 3.3 and 3.11 the change in particle concentrations is gradual as the aircraft approaches the edge of the anvil. But the changes in electric field are abrupt. For example in Figure 3.3 Emag changes from about 4 kV/m to ~25 kV/m in ~15 s.

Another possible explanation is that as the electric field weakens the attachment of ions to hydrometeors by field driven attachment lessens. Attachment by diffusion gains in relative strength. This will be discussed further in Section 5, but also is unlikely.

4.2 Reflectivity and Microphysics

Plots of AvgCube3x3 (the average reflectivity in a 3 km cube centered on the aircraft position and altitude) versus particle concentration from different probes and size ranges are shown in Figure 4.3. These are produced from the same data set used for Figures 4.1 and 4.2 and use the same concentration ranges and categories of probes/sizes.

The average reflectivity in a 3 km cube was used in these plots for a couple of reasons. First, the 30 s averages of the aircraft data in the “minflt” file correspond roughly to 3 to 3.5 km of flight track. Additionally, the 3 km cube average helps to reduce variations arising from scan gaps compared to the individual 1 km pixel values of gridded reflectivity.

Even though there is a lot of point-to-point variation in these plots, unlike the plots of Emag vs concentration in Figure 4.2, the 3 km cube average reflectivity has a relatively well behaved and power law relationship with the particle concentrations on this log log plot. (Reflectivity is defined as 10log Ze, thus is also on a log scale.). The point-to-point scatter along values of constant reflectivity is greatest for the intermediate size particles. The scatter is less and the linear relationship is more apparent for the >1 mm and the >3 mm plots of 4.3 E and F), particularly Figure 4.2 F, which represents the largest particles. This is as expected because reflectivity is proportional to the 6^{th} power of particle size, the very largest particles are dominantly responsible for the radar return. Consequently the relationship is best between AvgCube reflectivity and concentrations for >3 mm sized particles.

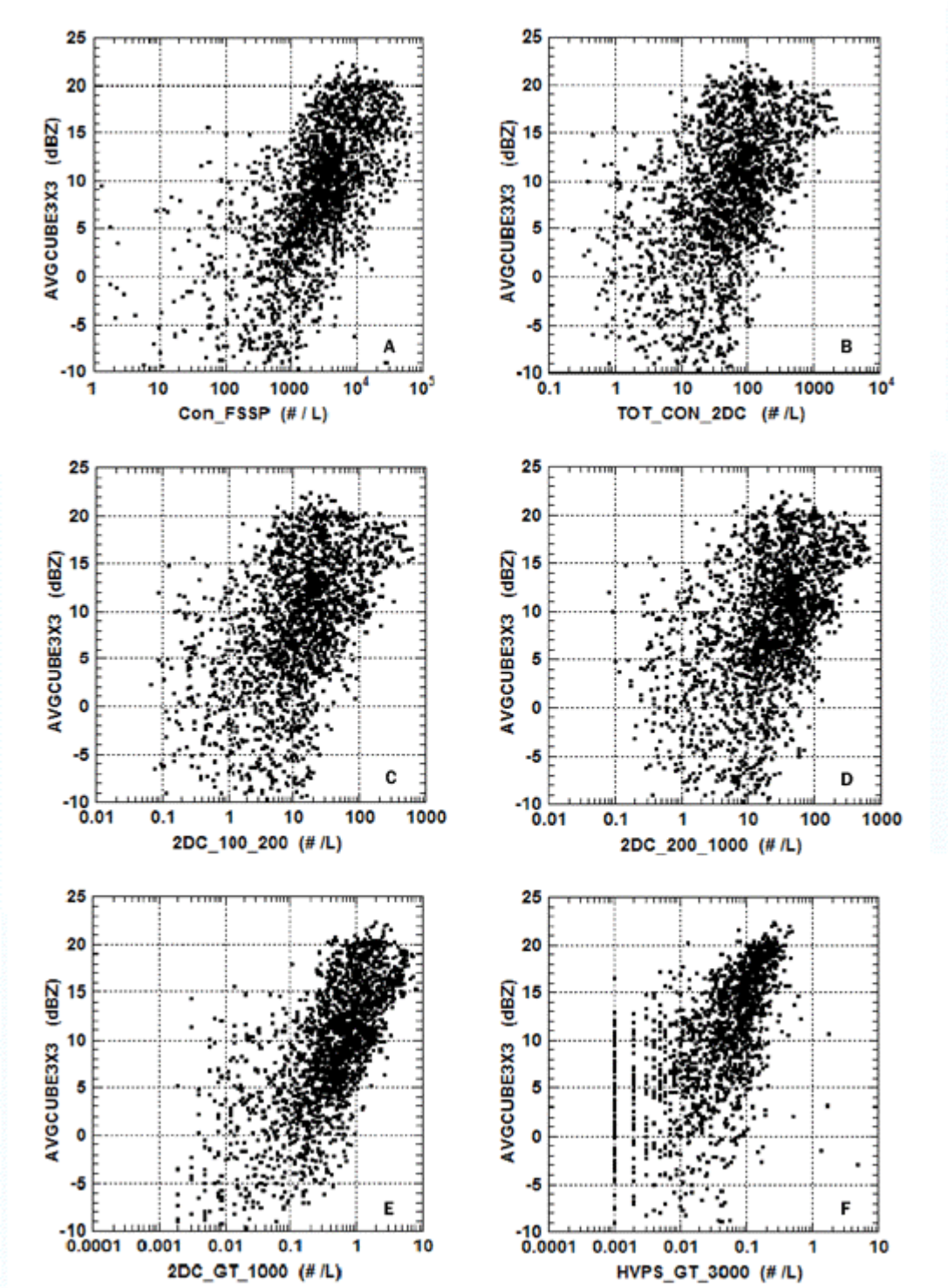

Figure 4.3 Average reflectivity in a 3 km cube centered on the aircraft position and altitude plotted as a function of particle concentrations for the same probes and size ranges as used in Figure 4.2.

4.3 Electric Field and Reflectivity

If we now use the "minflt" file to plot Emag as a function of AvgCube3x3 reflectivity, we obtain the plot in Figure 4.4. The plot shows an inflection or change in slope of the main clustered points at Emag ~3 kV/m in a similar fashion as the Emag vs. particle concentrations plots of Figure 4.2. It does not show the power law relationship seen in plots of AvgCube reflectivity versus particle concentration of Figure 4.3. Given the observed characteristics (Figure 4.2) of the relationship between Emag and particle concentration for all sizes categories and the direct calculable relationship between reflectivity and particle size, the characteristics of the Emag vs. reflectivity plot in Figure 4.4is a reflection of and results from the Emag vs. particle size distribution relationship.

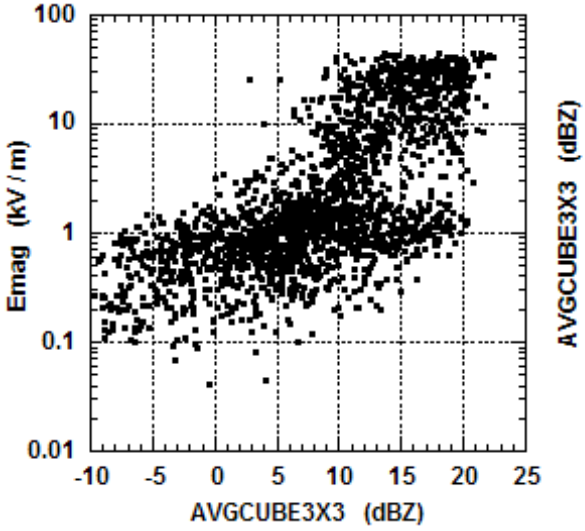

Figure 4.4 Emag plotted as a function of 3km Cube average reflectivity.

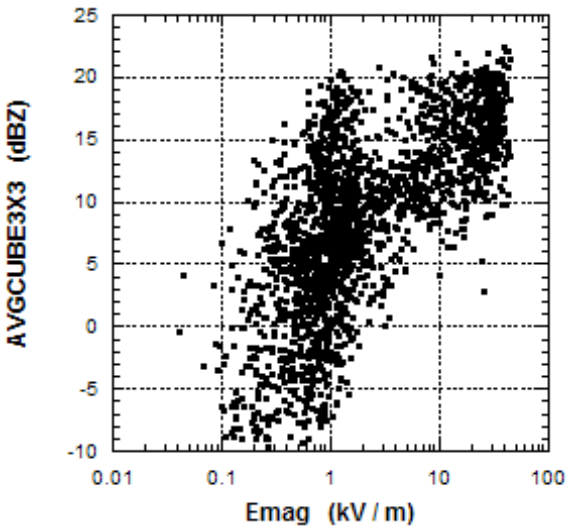

Figure 4.5 Same as Figure 4.4 except with reversal of the X and Y axes.

If we swap the X and Y axes of Figure 4.4, we obtain Figure 4.5 which is one of our familiar scatter plots of reflectivity parameter versus Emag, in this case for the CubeAvg3x3 reflectivity. The character of our many scatter plots of reflectivity parameter versus Emag originate from the character of the Emag vs. particle size distribution relationship. Physical processes producing the Emag vs. particle relationship lead to the Emag vs. reflectivity relationship.

We expect to find a power law relationship between reflectivity and particle concentrations, particularly for the largest particles, because for a given particle size, reflectivity is directly proportional to the concentration. The well behaved relationship of reflectivity with particle concentration over all size ranges as seen in Figure 4.3 is a result of the particle consistency from anvil to anvil. This consistency suggests that the particle size distribution is a result of the same physical processes (turbulent mixing, evaporation, aggregation, sedimentation, etc.) occurring at similar rates in the different anvils.

However, there is, *a priory*, no reason to have expected the particular relationship seen in Figure 4.2 between electric field and particle concentrations over all size ranges and especially the different character above and below Emag of 3 kV/m. In retrospect, perhaps we might have anticipated this result. Although particle concentration and size tends to vary smoothly in the anvil, the electric field usually shows abrupt changes, as seen in Figure 3.3. The character of this E versus concentration/size particle relationship must be the result of physical processes occurring in the anvils. The observations show that towards the edge of anvils the reflectivity and particle sizes and concentrations decrease, probably due to turbulent mixing with subsequent evaporation and possibly sedimentation. The decrease in particle concentration and size, and hence cross-sectional area, leads to a much more rapid decay of electric field in those regions. Perhaps the change in slope at Emag ~3 kV/m might be due to this increased rate of field decay as particle concentrations and sizes decrease in proximity to anvil edges. Additional work and thought is necessary to explain these observed results.

5. ELECTRIC FIELD DECAY AND MICROPHYSICS

To support the ABFM measurements and to better understand the decay of electric fields in Florida anvils, John Willett developed a simple model to estimate the decay of electric field with time in anvils. For a detailed description of this model see Willett (1991 and 1993a). These are available on the ABFM Web site Reports Page as Electrical Decay Model for Anvil Clouds No. I and No 2, J. Willett. In the final report for this study Willett (2003c) uses statistical and a case study approaches to compare the model with ABFM observations. (Electrical Decay Model Validation, Final Report, J. Willett).
An abbreviated description of the model and results can also be found in Willett and Dye, (2003) and a comparison of model results with observations in Dye et al. (2003).

The mechanism for field decay in the model is that ions produced by incoming cosmic rays attach to cloud hydrometeors by electrical drift and diffusion, thereby decreasing the bulk conductivity inside the cloud. Bulk current flow to the surfaces of the anvil reduces the charge contained in its interior. The model assumes a constant influx of cosmic rays, no turbulent mixing, no sedimentation of particles and the absence of active charge separation in the anvil. The model calculates electric-field decay time at a given time and location along the aircraft track based on the observed particle size distribution at that time and location and assumes that the given size distribution is uniform and constant everywhere in the model anvil during the decay of electric field.

The assumptions in the model provide upper bounds on the time to decay and lower bounds on the rate of decay of electric field. A "high-field limit" is identified, for ambient field intensities greater than a couple of kV/m, in which the model field decays linearly with time A decay time scale (τ_E in Willett's reports or ETmScl in the "minflt" and "MERGED" data files) is defined as the time required for the electric field to decay to zero from an arbitrary initial value of 50 kV/m. In this high field limit τ_E is found to be directly proportional to the particle effective electrical cross section (area), integrated

over the size distribution. Examples of these electrical decay time scale values for one transect of an anvil were presented at the bottom of Figure 3.6.

5.1 Electrical Decay Time Scale and Particle Size Distributions

The model shows that the particle size distribution primarily controls the time required for the electric field to decay to safe values at a given location, more specifically the particle cross sectional area at that location, along with the strength of the electric field at that location. This point was explored for different size categories with several figures in Willett's final report. As seen in Figure 3.6 particles in the size range of ~200 to ~1000 (or sometimes 2000) μ contain the largest fractional cross-sectional area per unit particle size as well as the largest total area for the different size categories (Figure 3.9). This finding is a direct result of the nature of the observed size distributions in these anvils. Particles of these sizes (200 to 2000 μm) have the dominant influence on electrical decay times, because EtmScl is proportional to cross sectional area. To illustrate the high degree of correlation between EtmScl and particle concentrations in this size range (Willett

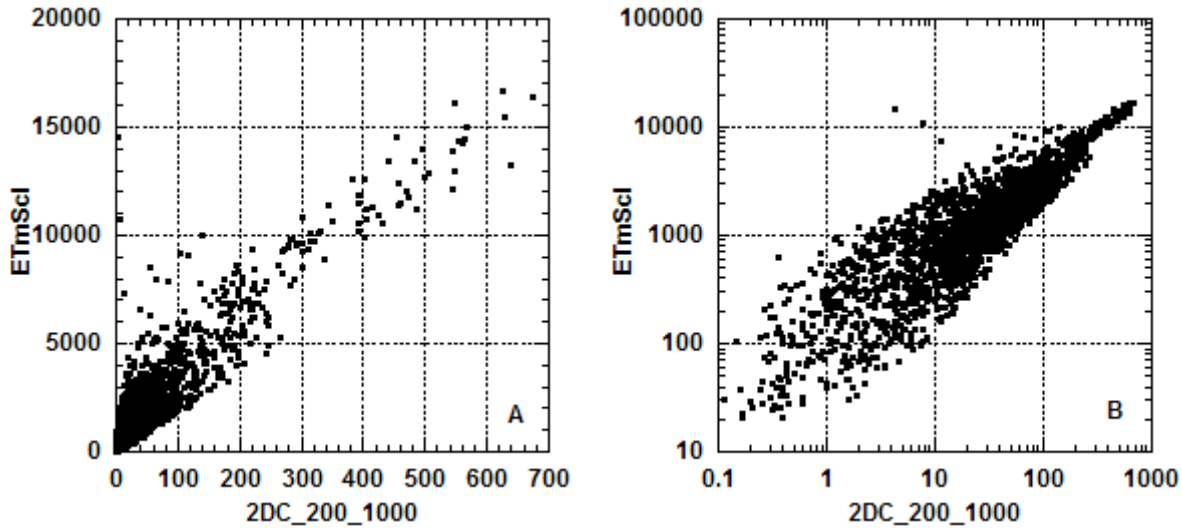

Figure 5.1 EtmScl (sec) as a function of particle concentration for 200 to 1000 μ measured by the 2DC. (**A)** EtmScl plotted on a linear scale. (**B)** Plotted on a log scale.

shows 0.92 for this same "minflt" data set), we present Figures 5.1 A and B. Figure 5.1A is the same as Figure 7 of Willett's final report and is plotted on a linear scale. Figure 5.2 B shows the same points but plotted on a logarithmic scale. Both the linear and log plots show the high degree of correlation. The apparent increase in scatter on the log scale at low particle concentrations is the result of variation of other parameters such as temperature and pressure in the calculation. Variations of this same magnitude are present for larger values of EtmScl but are contracted by the log scale.

5.2 Electrical Decay Time Scale and Reflectivity

Ideally for new LLCC rules we would like to find a proxy such as radar reflectivity to use as an indicator of the presence of strong electric fields. Figure 5.2 shows ETmScl plotted versus the 3 km cube average reflectivity. This figure is similar to Figure 14 in Willett

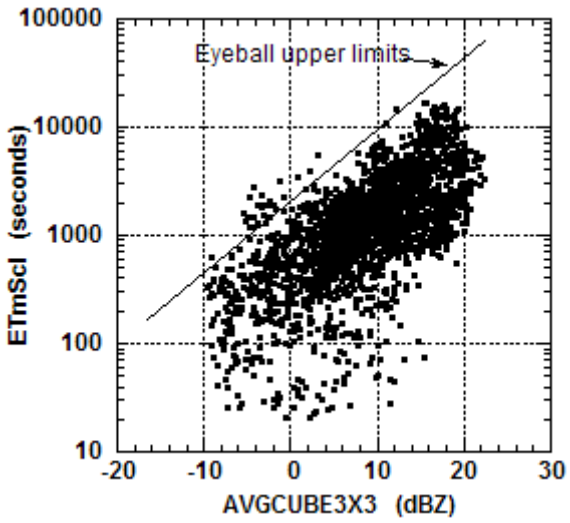

Figure 5.2 Electrical decay time scale (ETmScl in seconds) versus the average reflectivity in a 3km cube centered on the aircraft location and altitude. The diagonal line is an "eyeball" fit of the upper envelope of most points.

(2003). From the figure we see that for a constant value of reflectivity the electrical decay time scale varies over an order of magnitude. For example, for an average reflectivity of 10 dBZ the electrical decay time scale (ETmScl) of the majority of the points ranges from ~400 s (6.7 min) to >6000 s (100 min or 1.7 hrs). If we consider all plotted points the variation is even larger. Although reflectivity might be a useful indicator in some circumstances, it certainly should not be used as a direct proxy.

It is revealing to use the upper envelope of points in Figure 5.2 as upper limits on electrical decay time scales for different reflectivities. For this purpose a line has been drawn by eyeball as an upper limit to the vast majority of the points, but does exclude several outliers. Along this line, an upper limit of decay time scale for –10 dBZ would be ~450 s (7.5 min), for –5 dBZ would be ~1000 s (16.7 min), 0 dBZ would be ~2200 s (37 min), 5 dBZ --- 4400 s (73 min), and 10 dBZ --- 9600 s (160 min). This exercise illustrates vividly the large increase in decay time scale with increasing reflectivity. These times are estimates of electric field decay from 50 kV/m to 0 kV/m assuming that that the decay is linear and occurring in the "high field limit". They should not be interpreted as the actual time for electric field decay for the individual points of reflectivity.

5.3 Electrical Decay Time Scale and Electric Field

It is also instructive to examine the relationship between electrical decay time scale and electric field. This is done on both a linear and a log scale in Figures 5.3 A and B.

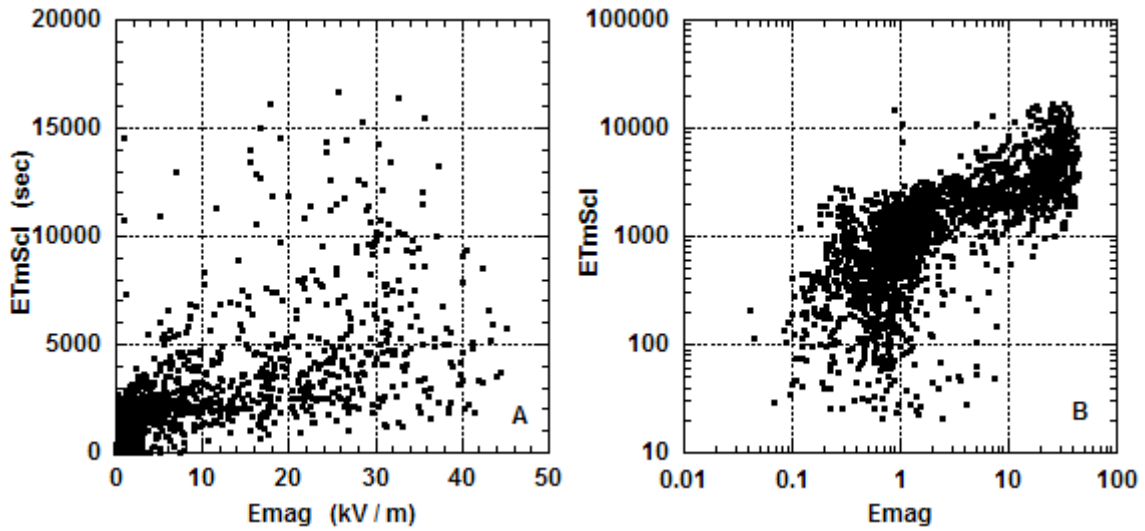

Figure 5.3 Electrical decay time scale plotted as a function of electric field using linear scales **(A)** and logarithmic scales **(B)**.

Figure 5.3 A is similar to Figure 15 in Willett (2003). As shown in his report the correlation between ETmScl and Emag is 0.68. Willett also shows an expanded plot (his Figure 16) of the lower, left portion of his Figure 15. His figure 16 shows that for decreasing values of electric field <~2 kV/m, ETmScl decreases rapidly. This can be seen in more detail on the log scale plot of Figure 5.3 B. For points with values of Emag <3 kV/m, ETmScl is almost independent of Emag.

If we interchange the X and Y axes in Figure 5.3 B in order to more easily compare with the plots of Emag versus particle concentration of Figure 4.2 we obtain Figure 5.4. Figure 4.2 D is copied on the right side of Figure 5.4 for comparison purposes. The similarity between Figure 5.4 and Figure 4.2 D is striking. Because ETmScl is strongly dependant upon particle cross-sectional area this similarity should not be surprising.

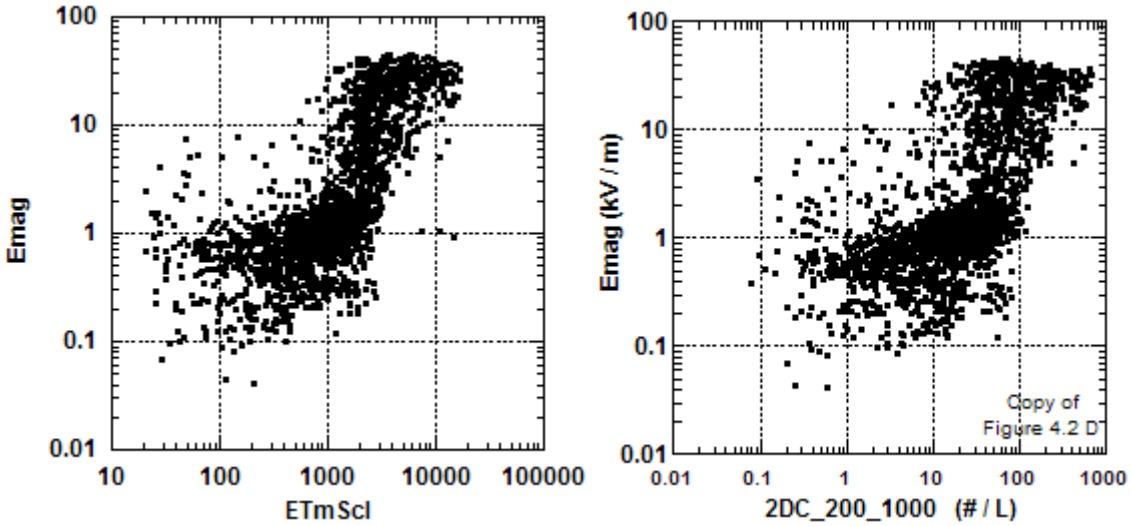

Figure 5.4 **Left side**: Same as Figure 5.3 B except with the X and Y axes interchanged. **Right side**: A copy of Figure 4.2 D for comparison.

On the far, upper right side of both Figure 5.4 and 4.2 D there are a number of points with very strong electric fields and very high particle concentrations (or ETmScl in Figure 5.4). An examination of the points with concentrations >200 per liter in Figure 4.2 D showed that these points are almost all from the June 24, 2001 intense tornadic case when the aircraft was close to the core and sometimes even flying in regions containing LDAR sources. The particle concentrations (and hence ETmScl) are larger for this case than for any of the other flight days. The only other points in this part of the plot besides those of June 24th are also when the aircraft was very near strong convective cores. A similar examination of the points with values of Emag <0.4 kV/m in Figures 5.4 and 4.2 D showed that these points are primarily from cases of detached anvils in advanced stages of decay such as 000611, 000615 (case I) and 010625.

With the exception of the points in the upper, far right and the lowest points with low values of Emag, the great majority of the points in Figures 5.4 and 4.2 D are distributed throughout all of the anvil cases. Thus the knee in these curves is not from any particular case but is a characteristic that is representative of all of the ABFM anvils.

For a broad range of strong to moderate electric fields from ~45 kV/m down to ~ 3 kV/m, ETmScl shows relatively little change with decreasing field. But for values of Emag <3 kV/m there is little change in Emag with decreasing ETmScl, especially if we remove the lower points from the greatly decayed, detached anvils. This behavior is similar to the behavior we see in Figure 4.2D or other plots in Figure 4.2 for particle concentrations in other size ranges. Since ETmScl is primarily dependent upon the particle cross-sectional area, this is to be expected, but again illustrates the control that the particle size distributions have on electric field decay.

As pointed out by Willett (2003) most cases in Figure 5.4 with low ETmScl (say, < 1000s) also have low Emag and most cases with high ETmScl (say, >3000 s) have moderate to high Emag. The concern is that for intermediate ETmScl, Emag can

apparently take on any value including some points with Emag > 3 kV/m. In an attempt to remove some of these "violators" (points with ETmScl <1000 and Emag >3000), Willett (2003) did further filtering of the data set to remove points for the aircraft flying near the cores, for nearby lightning, and for anvil types < 8 (See the in-anvil times link on the ABFM report page for discussion of anvil types) but the results were not much different than without this additional filtering.

This change in character must have important implications in terms of the decay of electric fields in the ABFM anvils. Figures 5.3 and 4.2D definitely show that once the electrical fields have decreased to roughly 2 to 3 kV/m, the decay time scale takes on a different behavior. Given the abrupt changes in electric field seen, such as those in Figures 3.3 and 3.11 for June 13, 2000, it appears that the decay from ~ 3kV/m to much smaller values is very rapid. Physically we do not yet understand what is happening, but there must be a shift in the physical processes that are acting.

5.4 Discussion

Although we have no explanation currently for the observed change in behavior of the electric field versus particle concentration (or electrical decay time scale), there are a couple of possibilities that we have considered.

As discussed earlier in this section it seems unlikely that changes in particle concentrations and sizes is responsible for the observed "knee" seen in several of our plots. Although electric field often changes rather abruptly, the concentration in different size ranges are much more smoothly varying. We can rule out this possibility.

After the electric field has decayed substantially, attachment of ions by diffusion to the hydrometeors begins to become important and eventually becomes the dominant mechanism of attachment. This is termed the "low field limit". The value of electric field at which field driven and diffusional attachment become equal for individual size distributions has been determined in the model and has been called E_{trans}. In Figure 5.5 a plot of E_{trans} versus Emag shows the electric field values of E_{trans} at this crossover. Almost all of the values lie between 200 and 800 V/m and show little variation with the magnitude of the electric field. Although the actual decay of electric field will begin to depart from the linear decay estimated by the "high field limit" at values larger than E_{trans}, these values are significantly below 2 kV/m, the kink of the main cluster of points in Figure 5.4.

In actuality the value of electric field at which diffusion begins to become more important than field driven attachment is a function of particle size. Table 5.1 gives a few examples of crossover as a function of sized based on Equation 2 of Willett and Dye (2003).

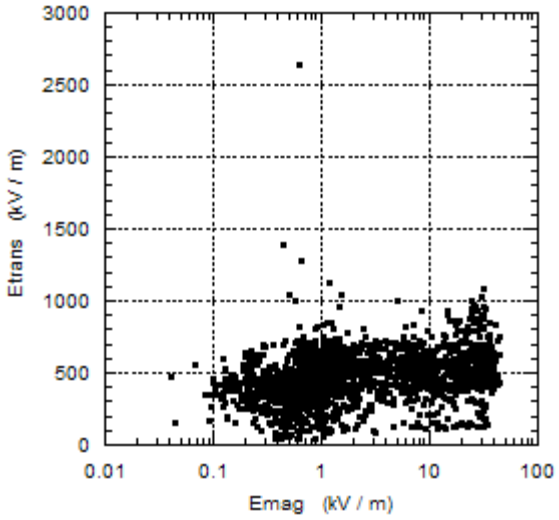

Figure 5.5 The electric field value (E_{trans}) at which attachment of ions to hydrometeors by diffusion becomes equal to that by field driven attachment is plotted as a function of the magnitude of the electric field (Emag).

Table 5.1 E_{trans} as a function of Particle Diameter

Diameter (μm)	E_{trans} (kV/m)
10	5.17
15	3.00
50	1.03
200	0.258
2000	0.0026

Even this more detailed look doesn't help in identifying a local physics change at 2 to 3 kV/m. Thus, the transition from field driven to diffusional attachment as an explanation for the kink in the ETmScl vs Emag plots also seems unlikely.

Many of our anvil passes were across the anvil, i.e. roughly perpendicular to the airflow in the anvil. Is it possible that the behavior across the anvil is different than along the direction of airflow in the anvil and this is the cause of the knee in our plots such as Figure 4.2 or others? Figures 3.1 and 3.3 are from a pass across the anvil of the June 13th storm. In Figure 3.3 we see that the electric field is <2 kV/m for the first 2 min (~14 km) before the electric field abruptly increases. Not all of the material exiting the storm contains sufficient charge to produce a strong electric field. We have seen similar patterns for other cross anvil passes. But we also had many anvil penetrations approximately parallel to the airflow direction. An example of a pass parallel to the wind can be seen for the June 13th storm in Figure 3.10 and also Figures 6.1 and 6.2 of the next section. For this case as for the across anvil pass of Figures 3.1 and 3.3 there is an abrupt increase in electric field even though particle concentration is gradually increasing. An examination of many along axis penetrations showed that this behavior of an abrupt increase in

electric field is characteristic of the along axis passes as well as the cross anvil passes. This cannot be the explanation for the knee in our many plots.

Another explanation that we have considered is the nature of how charge is exhausted from the convective core and main electrical generator of the storms. There is ample evidence in the literature, e.g. Dye et al. 1986; French et al. 1996, to show that the main charge separation mechanism occurs in or near updraft regions. Additionally we know that the charge separation mechanism can "turn on" very rapidly". Breed and Dye (1989) observed a case in New Mexico with an instrumented sailplane inside a growing cumulus congestus cloud in which the electric fields increased from values of ~ 1 kV/m to sufficiently large to produce lightning within 5 min. This rapid turn on might lead to the first charged particles being injected into the anvil rather rapidly and perhaps lead to abrupt changes in electric field, although it's hard to imagine it being so rapid that it can create the abrupt increase in Emag seen in Figure 3.3. But, in Florida the updrafts are often short lived as different updraft and convective cells grow and decay. In some of our observations near convective cores we clearly see substantial lumps in electric field that could be explained by the exhausting of pockets of charge into the anvil in separate pulses. Could the abrupt changes in electric field that we see such as in Figure 3.3 be a result of this phenomenon?

To properly address this question we would need to follow the decay of electric field in individual parcels as they move downstream in the anvil. We attempted to do this in ABFM but with limited success. In his Final Report Willett (2003) examines the few cases where this was attempted. The conference preprints of Willett and Dye (2003) and Dye et al., (2003) compare model and observational results of E time decay for the June 13th case. One of the problems encountered for the June 13th case as well as other cases is that the aircraft was not always at the altitude of maximum reflectivity. (See Figure 3.11.) Therefore the ETmScl calculations are lower estimates of decay time, because they are based on particle size and concentrations that are less than those existing in the larger reflectivities. As in the June 13th case, the different cases were not inconsistent with the decay of electric field as predicted by the model, but only in once case (June 14, 2000) were the observations sufficiently good to be able to compare with confidence. This case showed agreement between the model and observations. Overall, the results were not very conclusive. See Willett (2003) for presentation and discussion of the different case studies.

6. POSSIBLE REFLECTIVITY PARAMETERS

During the field campaigns we became aware than radar reflectivity often had prognostic value in telling when the aircraft might be entering or leaving strong electric fields. There often was a transition from weak to strong fields at reflectivity of very roughly 10 dBZ at the location of the aircraft. This was not always the case, but it occurred frequently enough to give us hope that a radar parameter might be suitable for use as a proxy for strong electric fields. However as shown in Figure 4.4 or 4.5 there is a lot of variation in the relationship between electric field and the 3 km Cube average reflectivity. It is not well behaved and reflectivity cannot be a direct proxy.

One problem in considering a reflectivity parameter is that both the WSR74C and NEXRAD have gaps in their elevation sweeps particularly at altitudes above 15,000 ft over the KSC range. An example of scan gaps near KSC is readily seen in the 10 km CAPPI in Figure 6.1 for the June 13th 2000 flight. Figure D1 in Appendix D shows where scan gaps exist as a function of elevation and range for the 74C radar including over the SLC 17A and SLC 39B launch pads. These scan gaps occur over the KSC range for both

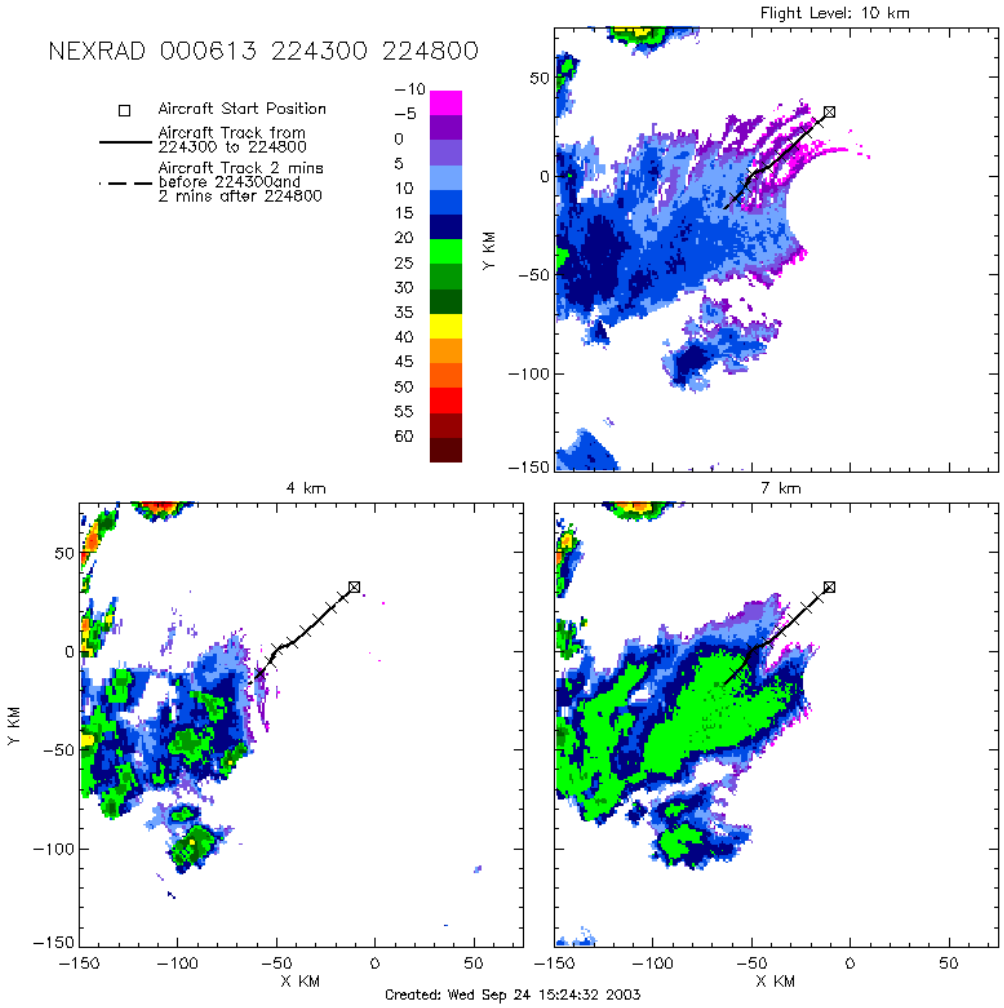

Figure 6.1 As in Figure 3.1 except for the period 2243 to 2248.

the 74C and NEXRAD radars at the altitudes of most concern for the possible existence of strong electric fields and possible electrification, ie. at altitudes greater than the freezing level.

The MER plot corresponding to this time period is shown in Figure 6.2. Note in the reflectivity curtain of this figure that as the aircraft first starts to penetrate this anvil, the reflectivity at the aircraft location (the bold, solid line in panel 2) shows large variations.

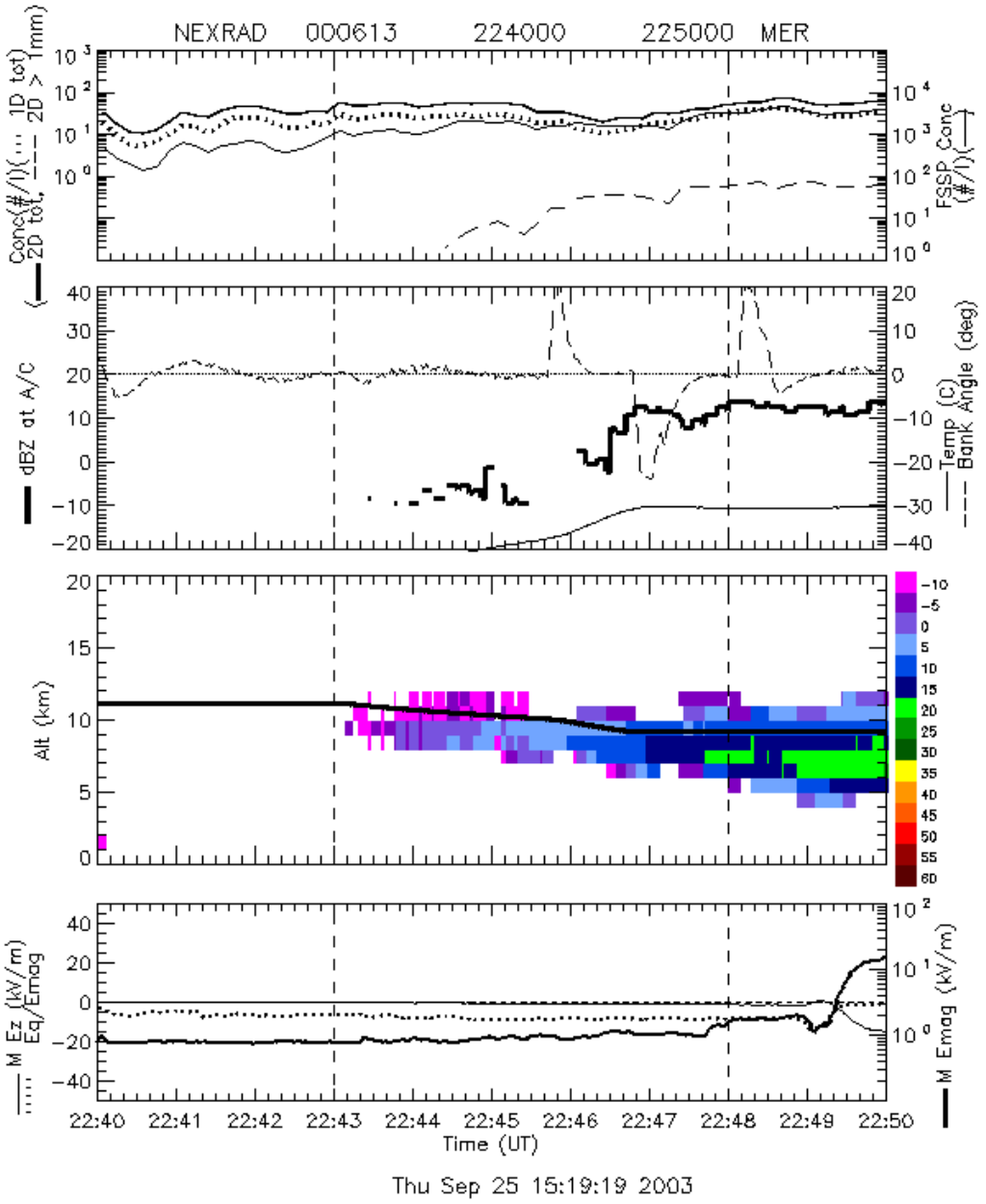

Figure 6.2 As in Figure 3.3 except for the time period 2240 to 2250.

Much of this variation may be due to scan gaps. As a result of these scan gaps and also because temperature gradients can distort the radar beam the ABFM team concluded that the reflectivity at the aircraft (dBZ at AC) would not be a suitable parameter for use in a radar based rule. This plot also serves to so that even along the axis of the anvil the increase in electric field is often abrupt, much more so than the gradual changes in particle concentrations for different sizes.

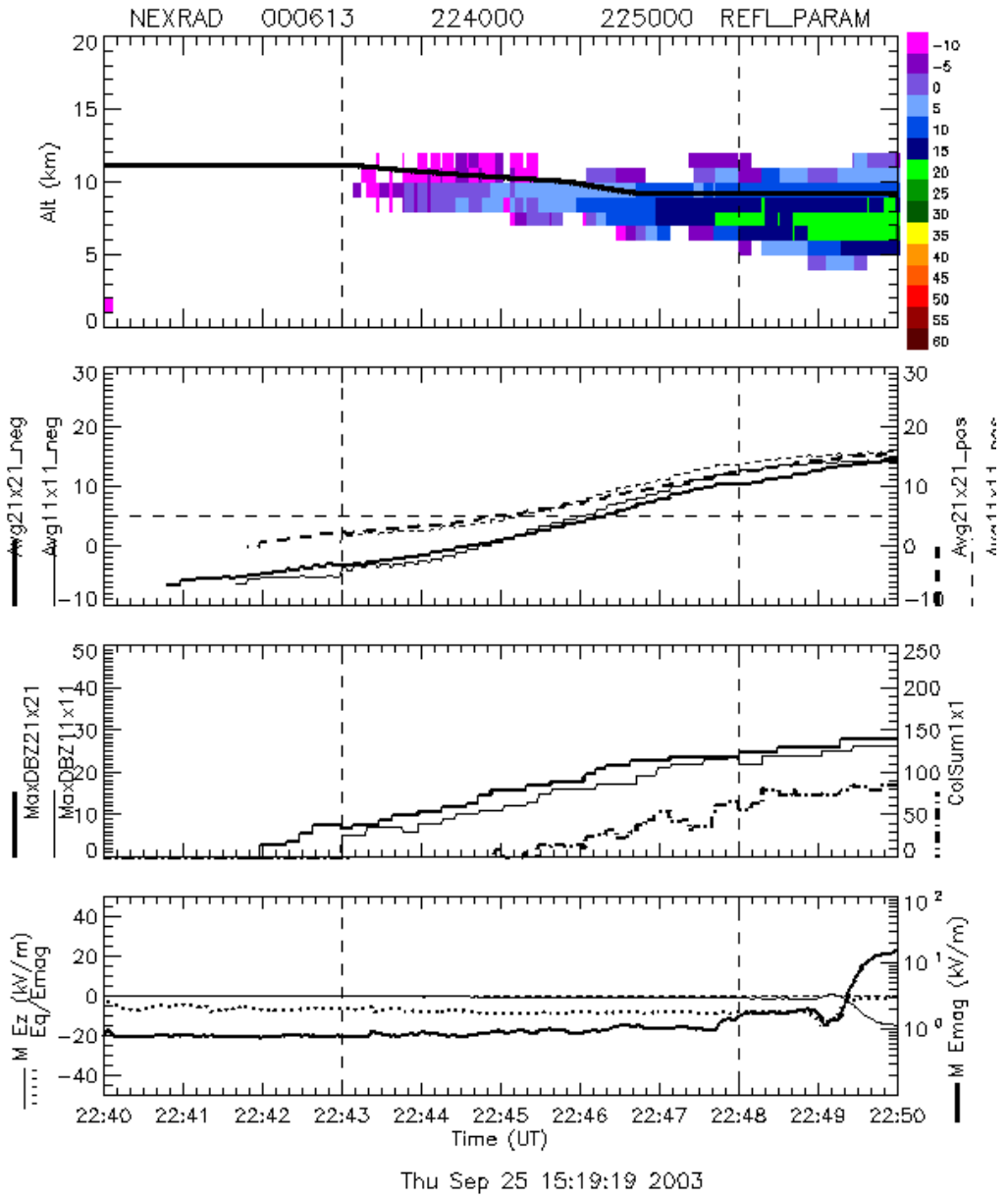

Figure 6.3 Top panel: Reflectivity curtain above and below the aircraft with aircraft altitude shown by the bold line. **Second Panel**: Column average reflectivity for 11x11 and 21x21 columns using –10 dBZ cutoff (left axis) or 0 dBZ cutoff (right axis) as indicated. **Third panel**: Maximum reflectivity in the 21x2 or 11x11 columns (left axis) and Column sum of dBZ values in the 1x1 km column containing the aircraft position.

The 1x1Column Sum was another parameter that we considered in our early discussions. An example of the 1x1Column sum is shown in Figure 6.3 (a dash-dot line in panel 3). It is the sum of values of dBZ in each 1 km cube pixel of the gridded radar data summed from 5 km (approximately the freezing level) to the top of the cloud. The first ABFM (ABFM I) project used a similar parameter that they referred to it as VIR0C (Vertically Integrated Reflectivity above the 0C level).

Similar plots to that in Figure 6.3 for other times and other days can be found by going to the Daily Home Page for individual flight days and clicking on Link 4 for the WSR74C radar or Link 9 for the NEXRAD radar. In addition to plots such as displayed in Figure 6.3, there are similar time series plots showing the standard deviation, the skewness and the number of pixels for the 11x11 and 21x21 column averages along the aircraft track.

We debated whether the column sum should be the arithmetic sum of dBZ values or a geometric sum, ie. convert the dBZ values to Z, average the results, then convert back to dBZ. We concluded that an arithmetic sum of dBZ would be preferable because the geometric sum is dominated by the very few pixels with the very largest reflectivity. The scan gaps also influence the column sum in an undesirable manner. Note that, like dBZ at AC in Figure 6.2, the column sum jumps around a lot from one 10 s period to the next.

6.1 Reflectivity Averaging

In order to overcome the artificial variations caused by scan gaps in values in both dBZ at AC and 1x1ColumnSum, we began to explore averages of reflectivity over larger volumes. Because electrification primarily occurs in the mixed phase zone containing both ice and supercooled water, we limited these averages to altitudes above the freezing level, ~5 km MSL in Florida during the summer. All averages, maxima and sums are for altitudes $\geq$ 5 km. Examining a reflectivity variable over a larger volume has the advantage that if substantial charge exists nearby, but not at the aircraft position, the variable would include nearby regions of higher reflectivity and perhaps give warning of nearby charge. We considered areas 5 km or 10 km to the N, S, W and E of the aircraft location, thus areas of 11x11 and 21x21 km, respectively. We refer to these volumes over which the averages are calculated as the 11x11 Column and the 21x21 Column. (Initially we referred to the 11x11 Column as the 5 km box and the 21x21 Column as the 10 km box. Some of the early plots on the Web site may contain this terminology.) Figures 6.4 and 6.5 show two examples of these early scatter plots for the June 13th case, one for dBZ at AC and the other for a 5 km box average (now called 11x11 Column Average). Comparison of the plots shows that dBZ at AC is noisy with more outliers, particularly in the lower left corner for weaker reflectivity but with moderate values of 3 to 5 kV/m for Emag. Furthermore, as we saw during the campaigns and from plots such as Figure 3.3, as a result of the rapid change of electric field, there is a floor in reflectivity between 5 and 10 dBZ below which the electric field is weak. This is especially apparent in the 11x11Column average.

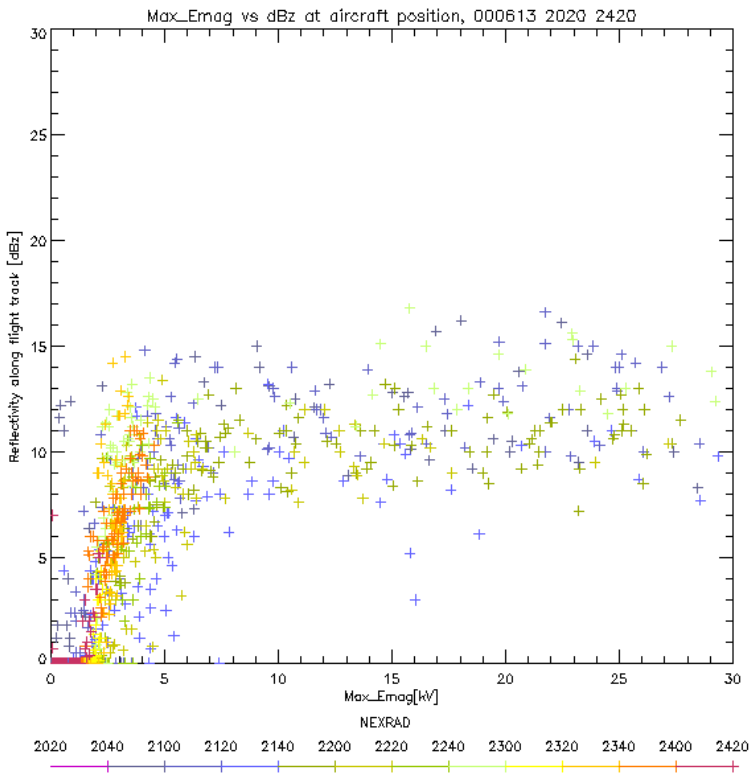

Figure 6.4 Reflectivity at the aircraft versus Emag for entire flight of June 13, 2000.

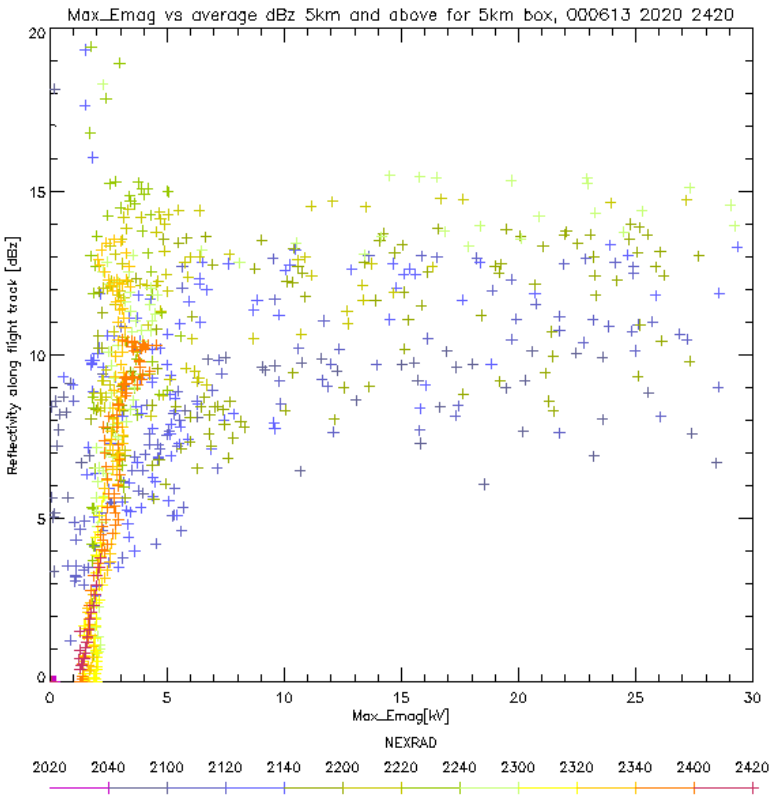

Figure 6.5 Same as Fig. 6.4 but for 11x11Column average reflectivity vs. Emag. and subsequent scatter plots 10 second averages of Emag were used to approximately match the 1 km grid spacing of the reflectivity data. At the flight speed of the Citation of 100 to 120 m/s, 10 sec represents 1 to 1.2 km of flight path.

There has been a lot of discussion among participants of benefits and disadvantages of the 11x11 and 21x21 column averages. A plot of the 21x21 column average versus Emag (not shown) gives similar results to Figure 6.5. In cases where the variations of reflectivity are on a smaller scale, for example near convective cores, the differences between the 11x11 and 21x21 Column averages are sometimes greater. We debated if an arithmetic or geometric average should be used and if a reflectivity cutoff of 0 dBZ should be used rather than –10 dBZ. We also asked if the maximum reflectivity within the 11x11 or 21x21 column might be used. These issues are discussed in two reports available on the ABFM Web site.

1) Reflectivity Averaging: A Monte Carlo Study *by F. Merceret*
   and
2) Why we average dBZ rather than Z *by S. Lewis*

Quoting from Frank Merceret's report: "*The peak value* (maximum reflectivity) *is probably too sensitive to the whims of sampling to make a good indicator for operational decisions. Although in the aggregate over a large number of runs, it is related consistently to the input distribution, the individual cases examined in the verification of the lognormal computations showed peak values differing by more than 10 dBZ from the same population. To a considerable extent, the Z-average process also shares this disadvantage.*

The truncated average (i.e. the average using 0 dBZ reflectivity cutoff) seems to have no real advantages over any of the other methods and it has the serious disadvantage of being a biased estimator of the process.

Thus, the outcome of this study suggests that the best methodology of the candidates here for generating a radar box parameter is to use a straight average of dBZ values including all points down to the noise level in the average."

6.2 Scatter Plots of Emag versus Different Reflectivity Parameters

As we worked with the data set and various scatter plots we became aware that attenuation of the 74C radar return by either intervening precipitation or by wet radome attenuation was a problem for some cases and times. An analysis was performed to identify times when attenuation would be a problem. A description of how the determination of attenuation was made and a list of times that should be filtered for attenuation are provided on the Web at the ABFM Report page at the Link Attenuation. This Link also summarizes and links to two reports written by Frank Merceret, one on intervening Precip Attenuation and the other on Wet Radome Attenuation for the 74C and NEXRAD radar. There is also a link to a 3rd report on Wet Radome Recovery Time for the 74C by Frank and Jennifer Ward.

We also became aware that the aircraft at times flew in the cone of silence above the 74C or NEXRAD radars. Each case study was examined to determine when this occurred and to generate a list of times that should be filtered. These times can also be found on the ABFM Report Page by going to Times A/C near Cores for Anvils. Additionally we filtered for periods when the aircraft was flying at altitudes lower than 5 km MSL. All of our reflectivity parameters are calculated for data from 5 km and above and we wanted the aircraft and radar data to be consistent.

The following plots illustrate the effects of the different stages of filtering on the ABFM data set for anvils for the 11x11 Column average, the 21x21 column average, the 1x1 column sum and the 3x3x3 Cube average reflectivity. The entire ABFM data set is shown in Figure 6.6 but data points have been filtered out for times during which there was attenuation of the 74C radar, for times when the aircraft was flying in the cone of silence above the 74C radar, and for times when the aircraft was flying at altitudes lowered than 5 km MSL. We refer to this as minimum filtering.

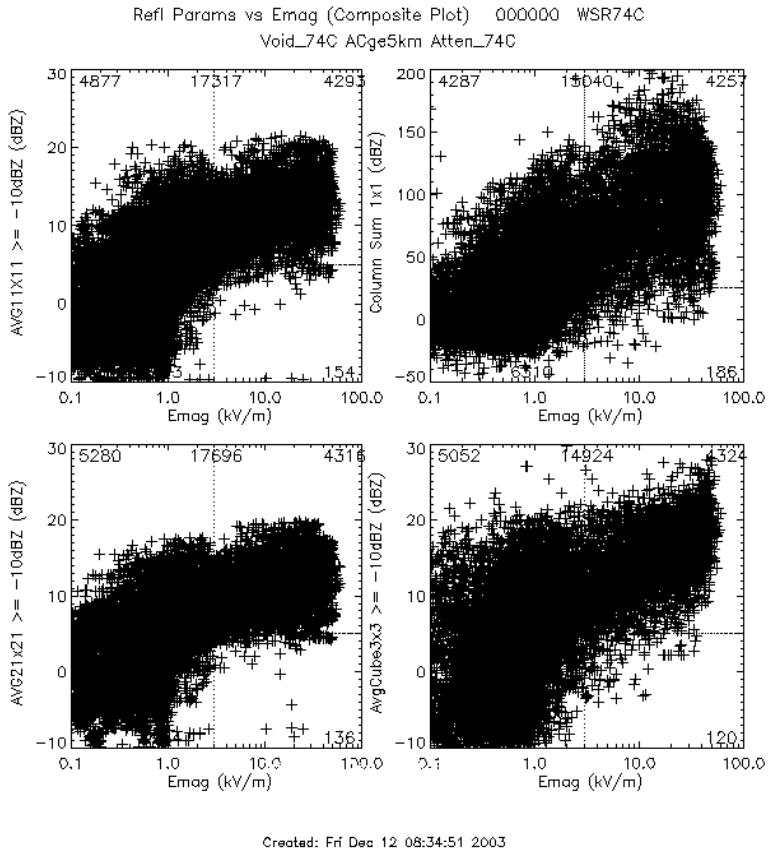

Figure 6.6 The entire ABFM data set for the WSR74C radar filtered to remove points with attenuation, aircraft in the radar void, and aircraft at altitudes <5 km MSL.

In Figures 6.6 through 6.10 we have used a threshold cutoff for the radar data for the reflectivity parameter calculations at –10 dBZ. The 74C radar has the capability of

detecting –10 dBZ out to a range of a little less than 100 km (See Appendix D), so for most of the 74C results the data are not significantly truncated. However, at a range of 50 km the NEXRAD data has a threshold of –8 dBZ and beyond 75 km truncation occurs at 0 dBZ. (See Appendix E). For an example, view the 7 km CAPPIs from ~1830 to 1930 for the June 28, 2001 case. Therefore, for many ABFM cases the NEXRAD effectively truncated at 0 dBZ or more. The issue of whether the reflectivity parameter calculations should use a cutoff of –10 or 0 dBZ is discussed later.

Each flight day was examined to determine if the aircraft flew in any anvils on a given day. Furthermore, we categorized the type of anvil according to criteria described on the Reports Page in the Link In-Anvil Dates/Times as of Sept 4, 2003. A list of times in which the aircraft was flying in anvils is also given in this same link.

Figure 6.7 is for the same data as in Figure 6.6, but we now have only accepted times during which the aircraft was flying "In-Anvil", i.e. the cloud feature in question had to

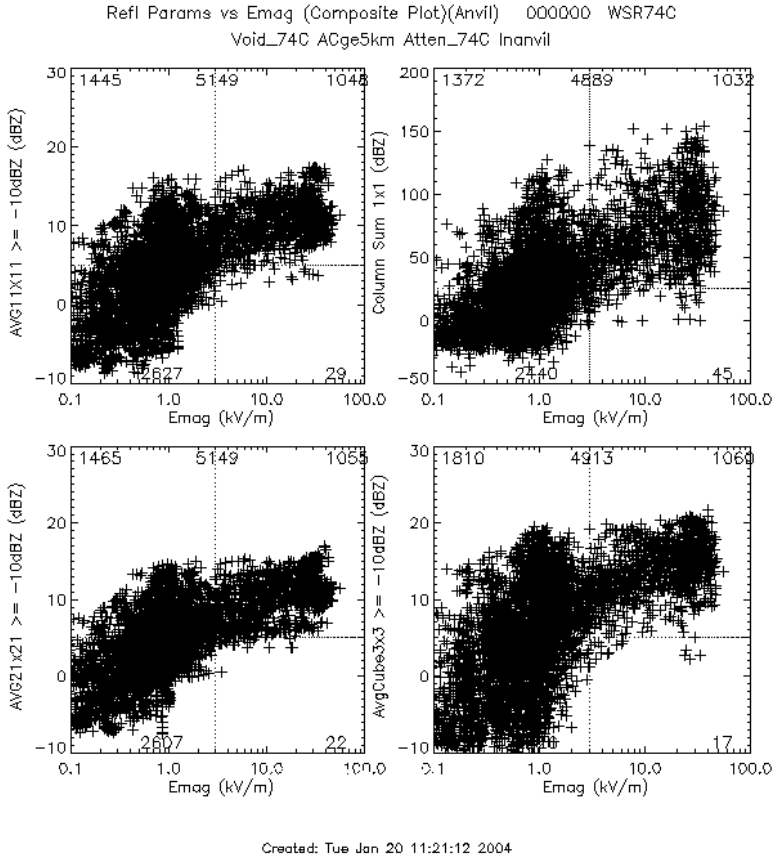

Figure 6.7 Same as figure 6.6 but only for periods "In-Anvil". The number at the top, middle of each plot shows the total number of points in the plot with the four numbers in each corner indicating the number of points in each quadrant defined by the dotted horizontal and vertical line.

have formed by divergence from the top of the convective core or transport of material from the convective core(s) by upper level winds. It also had to have a definable base without precipitation reaching the ground.

Some of the early scatter plots of column averages and column sum for the anvil cases were presented at the Nov 2002 ABFM/LAP workshop. The LAP found these encouraging but requested that we filter the data set for nearby lightning. Consequently one of the filters that we have employed to remove points when the aircraft was near lightning is the lightning filter. We explored a couple of different possibilities but soon settled on filtering the data at any given 10 s data point if there had been any CG flashes from CGLSS or 2 or more LDAR sources detected within 20 km during the previous 5 min period. Later the LAP also requested that we filter the data so as to avoid regions near convective cores. The plots in Figure 6.8 have been filtered to remove points with nearby lightning or times when the aircraft was within 20 km of a convective core with reflectivity of 35 to 40 dBZ, particularly on the 4 km CAPPI.

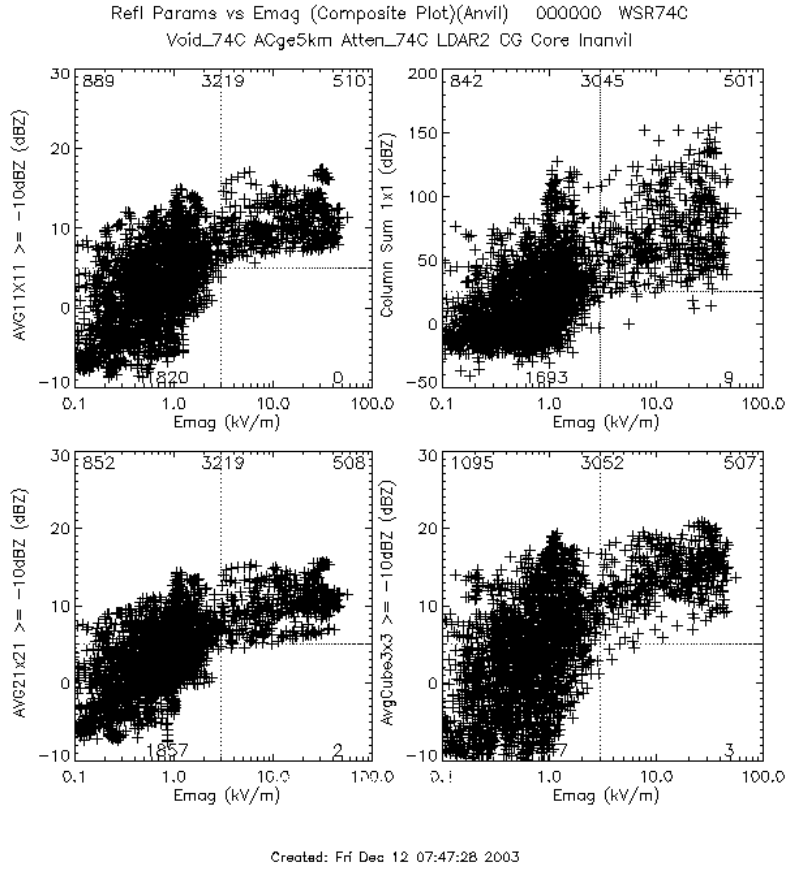

Figure 6.8 Same as figure 6.7 but filtered to remove data when the aircraft was flying near lightning or convective cores.

When the aircraft flies near a cloud/anvil edge the 11x11 or 21x21 column boundaries can extend beyond the cloud or anvil. In these circumstances even though a column average can be calculated, the average may contain relatively few pixels with a detectable radar return. To be able to determine when this occurs, we have calculated Frac, the number of pixels with detectable return divided by the total possible pixels. For an 11x11 Column average the maximum possible number of pixels is 11x11x16 (16 is the

maximum possible altitude difference in kilometers). But because of scan gaps and also because anvil tops seldom extend up to the top of our gridded radar data (20 km), typical values of Frac even in the interior of a thick anvil are often about 0.4 to 0.45. An examination of scatter plots showed that data points with Frac < 0.05 were often outliers. In Figure 6.9 we have arbitrarily filtered the anvil data set to remove points with Frac <0.05. Later analysis of volume integral parameters suggested that filtering for Frac <0.1 might be even better, especially for the NEXRAD data set.

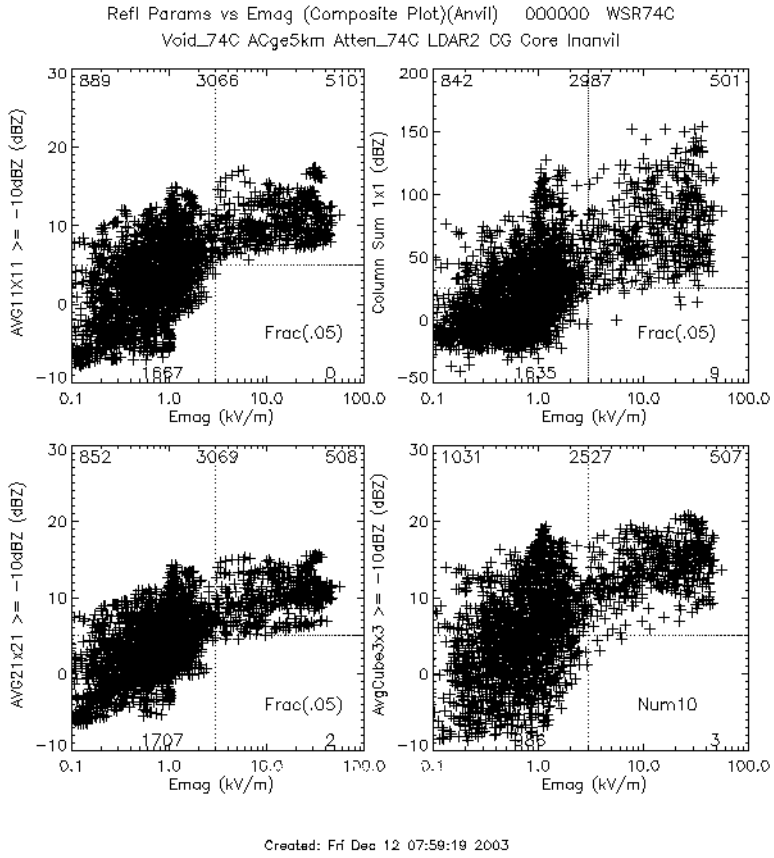

Figure 6.9 Same as 6.8 but filtered to remove data points with Frac <0.05 for the column averages and column sum and for number of pixels <10 for the 3x3x3 Cube average.

6.3 Volume Integrals of Reflectivity

During the November 2002 workshop and in recent white papers Bateman and Mach (2004) (On the ABFM Reports page go to Reflectivity Parameter Selection Discussion, then select Choosing An Algorith I, Choosing An Algorith II, and Choosing An Algorithm III) point out that averaging the reflectivity within a box or column throws away potentially important information on the depth of the anvil. A thin anvil can have the same average reflectivity as a much deeper anvil, but deeper anvils are more likely to contain charge than shallower anvils. In Figure 6.9 on the upper right hand side we have substituted the 1x1Column Sum of previous figures, such as Figure 6.8, with the 11x11

Volume Integral. In contrast with the 11x11Column average on the left of this figure that shows little change of average reflectivity with increases in Emag >3 kV/m, the 11x11Volume integral shows a trend of an increase in values of Volume integral with increases in Emag and a larger dynamic range than the 11x11 average reflectivity. The 1x1 Column Sum in Figures 6.7, 6.8 or 6.9 also shows the column sum reflectivity to tend to increase with increasing electric field and a greater dynamic range. But because the different flight cases are at different ranges, the radar observations contain varying degrees of missing pixels due to scan gaps. Thus column sums of the individual 1x1 columns can be biased for different cases and at different ranges, a concern we expressed earlier.

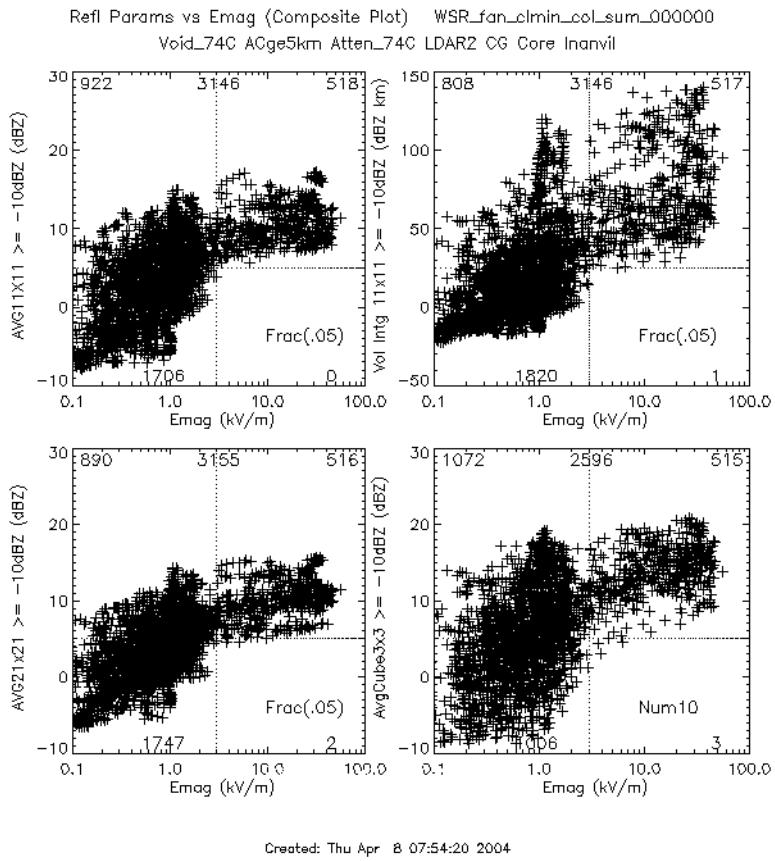

Figure 6.10 Same as figure 6.9 but 11x11 Volume Integral instead of 1x1ColSum.

The Volume integral in Figure 6.9 was calculated by multiplying the Column average by the average thickness of the 11x11 column. Beside the larger dynamic range, volume integral has the additional benefit that it provides an approximate correction for the scan gaps. The column average is the total sum of the dBZ values of all 1 km cube pixels divided by Nm, the number of pixels in the box with detectable radar return. But Nm/(Nt)(121) is an estimate of the fraction of pixels with detectable return compared to the total number the anvil would have contained if scan gaps were not present. The volume integral is effectively dividing the total sum of dBZ of the measured pixels by a correction factor for scan gaps.

Bateman and Mach (2004) conclude that a slightly better way to calculate an integrated reflectivity in a column is to determine the column sum for each individual 1x1 column, calculate the average reflectivity for that column, then multiply this 1x1 column average by the anvil thickness for that specific 1x1 column. Bateman and Mach refer to this calculated parameter as the Average Column Integrated Sum (ACIS). Merceret (2004) (On the ABFM Reports page go to Reflectivity Parameter Selection Discussion, then select CANDIDATE RADAR VARIABLES SUPPLEMENT) examined both the Volume Integral and ACIS and concluded that although there are slight differences in value, Volume Integral and ACIS are nearly the same. A comparison of these two parameters is shown in Figure 6.11. The figure also presents the Total Sum of all pixels with detectable return divided by 121 and the Sum Average, the sum of the average reflectivity for each 11x 11 km horizontal plane. Although there are slight differences between the different parameters the scatter plots are very similar.

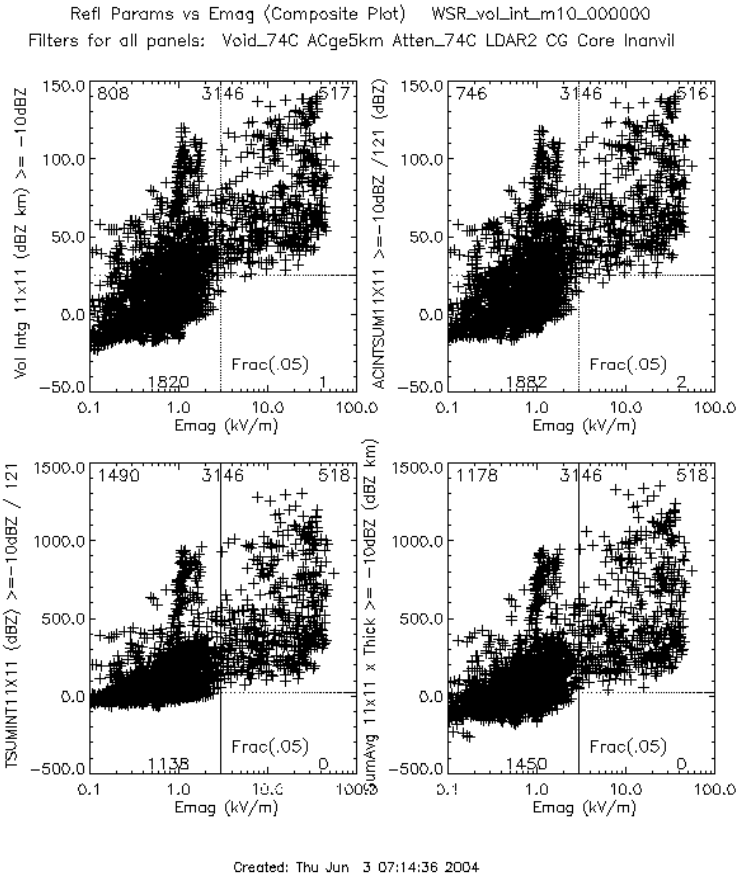

Figure 6.11 Scatter plots of various 11x11 column integrated volume reflectivities. **Upper left**: Volume Integral, (11x11ColumnAvg x Avg 11x11Thickness). **Upper right**: ACIS, (Integrated Sum of 1x1 km AvgColumn reflectivity). **Lower left**: TSum Integrated Reflectivity ([sum of dBZ for all 1 km pixels in the 11x11 Column]/121). **Lower right**: SumAvgInt (average dBZ in each 11x11 plane summed over each altitude x Avg 11x11Thickness).

There has been a series of exchanges on the pros and cons of various reflectivity parameters during the last couple of months. The interested reader can find them at the link **Reflectivity Parameter Selection Discussion** in the lower right side of the ABFM Web site.

The issue of what cutoff reflectivity, -10 dBZ or 0 dBZ is also discussed in some of the reports on this Link. The proponents for 0 dBZ feel that including pixels with reflectivity < 0 dBZ only serves to introduce noise into the scatter plots. Points with reflectivity <0 dBZ are not electrified. Proponents for –10 dBZ feel that excluding these points presents a statistical bias to the calculated parameters. Furthermore, the values being considered for a possible LLCC rule are near or only slightly above 0 dBZ, so inclusion of more of the range of dBZ values is desirable.

6.4 Scatter Plots for NEXRAD Radar

Similar procedures to those above for the 74C data were also followed for the NEXRAD data set and are shown in Figure 6.12. Data in this figure were filtered for In-Anvil, lightning, cores, and Frac. The results look very similar to those obtained from the 74C.

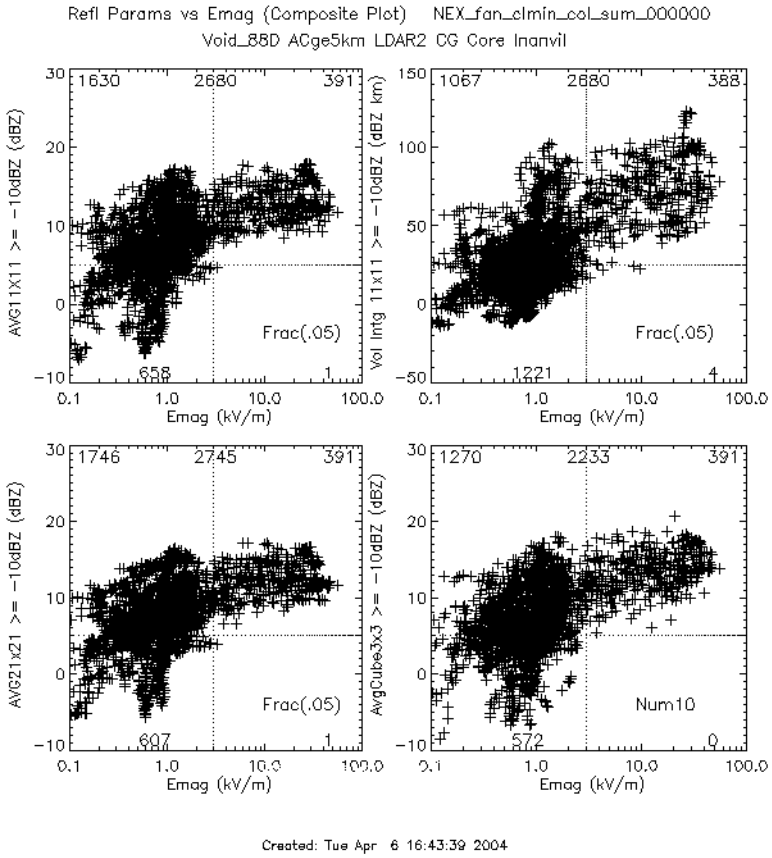

Figure 6.12 Same as Figure 6.10 but for NEXRAD rather than WSR74C. Minimum, In-Anvil, lightning, core, and Frac filters have been applied to the data set.

If we want to use the same LLCC rule for both the 74C and NEXRAD radar we want to assure ourselves than the reflectivity measurements are equivalent from the two radars. The results in the following three figures are by Merceret (2004) and can be found in the Reflectivity Parameter Selection Discussion link on the ABFM Reports page. The data set was the same data set used to produce Figures 6.10 and 6.12, ie. there was filtering for attenuation, voids, aircraft at > 5 km altitude, In-Anvil, lightning, cores, and Frac. See Examining Candidate Radar Variables in the above Link for more information. Figure 6.13 compares the 11x11Column Average reflectivity from NEXRAD with that from 74C using a cutoff of 0 dBZ. 0 dBZ rather than –10 dBZ was used because NEXRAD effectively truncated many of our ABFM measurements at 0 dBZ. Although NEXRAD is as much as 5 dBZ greater than 74C for some points, the correlation is high and the difference between the 1:1 line and the best fit line is within ~ 2dB at 15 dBZ and much less at lower values of reflectivity, those that will be of most concern for any anvil rule.

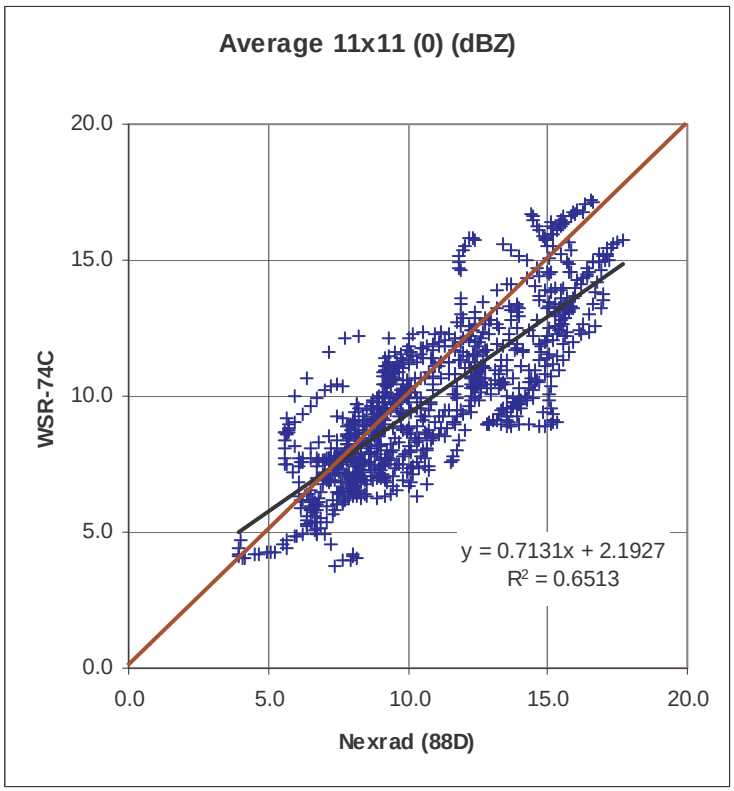

Figure 6.13 11x11 Column Average reflectivity from the WSR74C radar at Patrick Air Force Base compared to the WSR88D NEXRAD radar at Melborne Florida.

These differences are within typical uncertainties found for well calibrated radars in the meteorological radar community. The same comparison using a –10 dBZ cutoff (not shown here but available in the Candidate Radar Variables Supplement by Merceret at the Link above), shows the NEXRAD Column averages to be ~2 to 3 dB smaller than those from 74C, because of the higher dBZ cutoff for NEXRAD at most ranges.

Merceret also compared the 11x11 average Thickness measured by the two radars. The results presented in Figure 6.14 show that the 74C consistently shows a greater thickness than NEXRAD by 1.5 to 2 km, even though a cutoff of 0 dBZ was used for both radars. There is a tendency for slightly greater differences for greater anvil thicknesses. For smaller thickness somewhat greater differences were found between 74C and NEXRAD if a –10 dBZ cutoff was used instead of 0 dBZ, but only slightly larger.

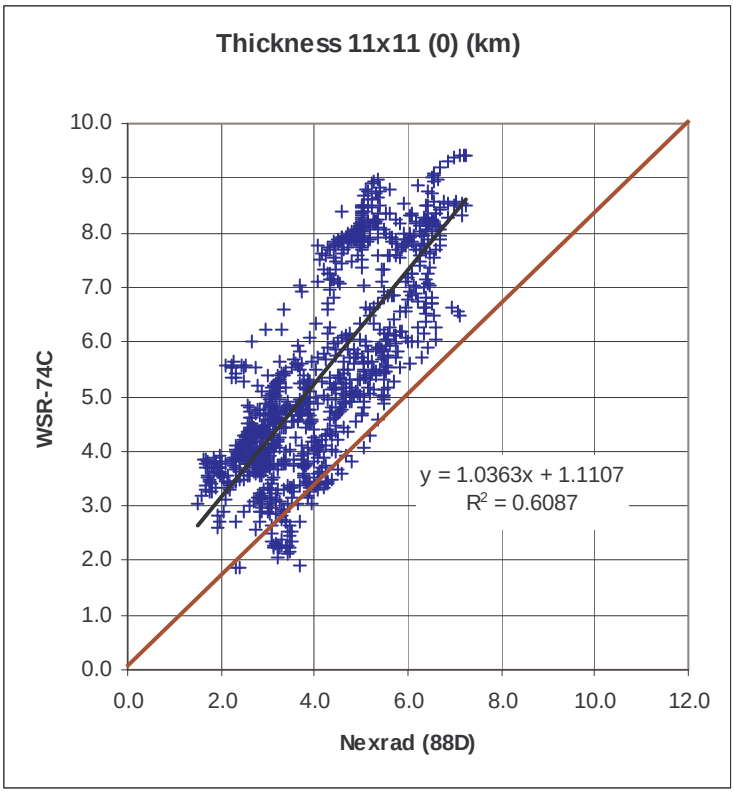

Figure 6.14 Comparison of anvil thickness determined from 74C and NEXRAD measurements using a 0 dBZ cutoff.

A comparison of the 11x11 Volume Integral determined by the 74C and NEXRAD radars is shown in Figure 6.14. The comparison shows good agreement. The slightly greater column average reflectivity from NEXRAD offsets the shallower thickness determined by NEXRAD. The same behavior occurs when the cutoff of –10 dBZ is used.

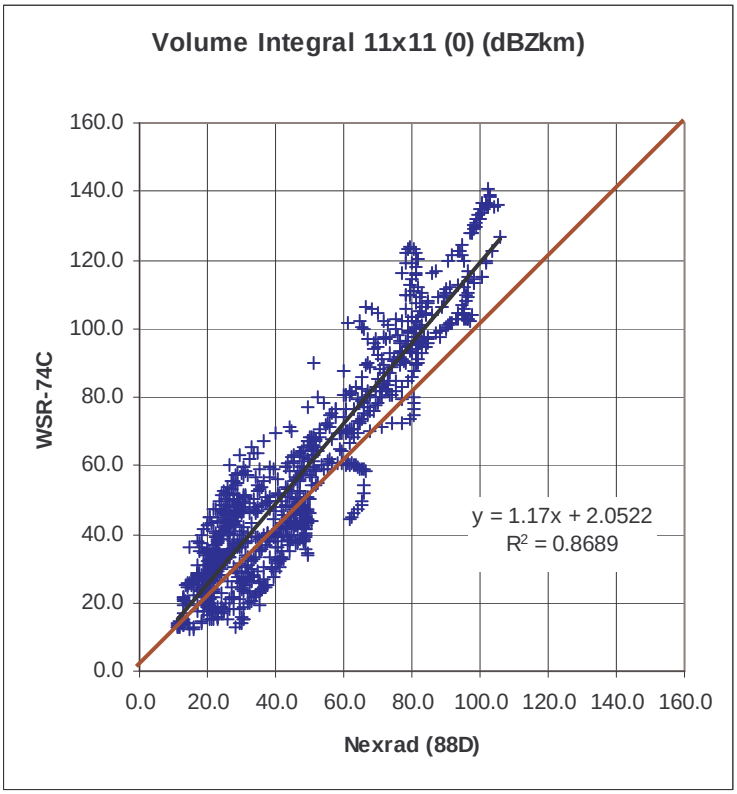

Figure 6.15 Comparison of the 11x11Volume Integral determined by 74C and NEXRAD.

6.5 Receiver Operating Characteristics (ROC) Curves

Both Merceret (2004) and Boccippio (2004) have suggested the use of ROC curves for identifying parameters from the scatter plots that would have the highest Probability of Detection (POD) with the lowest False Alarm Rate (FAR). At the Reflectivity Parameter Selection Discussion link see Exploring Candidate Radar Variables by Merceret for more of a description of ROC curves and their use. Also see Boccippio's ROC Analysis , Summary by Monte Bateman at the same link.

An example of ROC curves taken from Merceret (figure 5 in his report "Examining Candidate Radar Variables) is reproduced in Figure 6.16. These curves were generated with a reflectivity cutoff of –10 dBZ. The results show that 11x11Volume Integral gives a higher probability of detection than does the 11x11Column Average for both 74C and NEXRAD radars. A surprising finding from his study was that anvil thickness also had a high probability of detection.

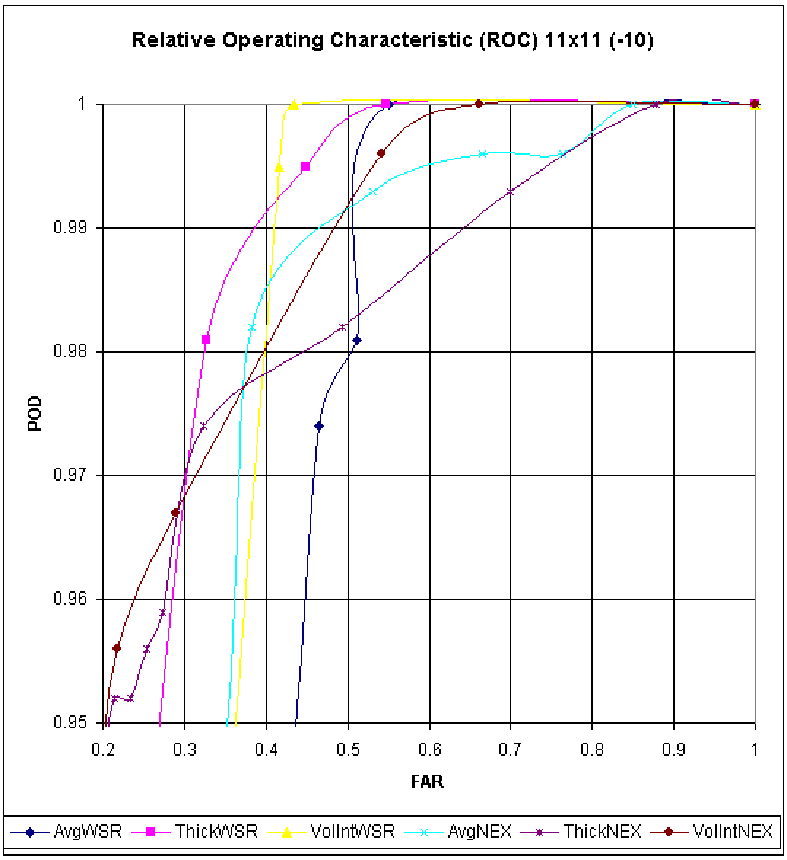

Figure 6.16 ROC curve for 74C and NEXRAD for 11x11ColumnAverage, 11x11 Average anvil thickness, and 11x11VolumeIntegral. Copied from Merceret (2004).

In the Reflectivity Parameter Selection Discussion link, the summary of Boccippio's ROC Analysis work reports that the 0 dBZ cutoff performed better than a cutoff of –10 dBZ for variables that were available. A figure showing this was unavailable at the time of this writing.

Further work by Merceret (See Candidate Radar Variables Supplement) showed that Volume Integral was less sensitive to the reflectivity cutoff than average or thickness because the effective cutoff for NEXRAD overestimates the Column Average but underestimates the 11x11Thickness. Since the Volume Integral is the product of Average and Thickness, the two biases offset each other. He concludes that the Volume Integral is a more robust parameter than the average in part because it is not as sensitive to the reflectivity cutoff.

Work by Boccippio shows that the FAR could be decreased by using a bi-variate analysis with 2 selected parameters such as Column average and Anvil Top (or Thickness), Volume Integral and Thickness or Volume Integral and Frac or a few other combinations. He has tested all possible variable pairs but a presentation of this work is beyond the scope of this report. His bi-variate analysis of the anvil data set does suggest that if we use one parameter as the primary variable (such as Column average), by using a 2nd

variable (such as anvil Top with Column Average), for different circumstances we might be able to increase/decrease the threshold value used for warning by the primary variable. For example, in the Reflectivity Parameter Selection Discussion go to Frame #6 in Boccippio's Bivariate Illustration. The threshold value of 11x11Column Average indicative of hazard could be greater when the anvil top is relatively low compared to when the anvil top is high. At the time of this writing the ABFM TEAM and LAP decided that the 11x11Volume Integral is probably the preferred parameter to consider for an LLCC rule. The group was divided on whether a reflectivity cutoff of –10 dbZ or 0 dBZ should be used. But in all likelihood it will not make a significant difference. The next step in trying to set a threshold for the radar parameter and also the threshold for the electric field at which triggering becomes hazardous is beyond the scope of the ABFM project and this report. Further consideration of these issues will be the work of the LAP.

7. ADDITIONAL OBSERVATIONS FOR POSSIBLE LLCC APPLICATION

7.1 Electric Field Decay Away from Cloud Edge

The distance from cloud edge at which the electric field is no longer hazardous (sometimes referred to as standoff distance) is included in many of the present LLCC. The observed electric fields plotted as a function of distance from cloud edge for both the ABFM I and the ABFM II data sets has been examined by Merceret and Ward (report not yet written) and are presented in Figure 7.1. Both the average and maximum values of electric field are greater for ABFM I than for ABFM II. The ABFM I data set was gathered for active, growing cumuli. The aircraft approached very near cloud edge, then

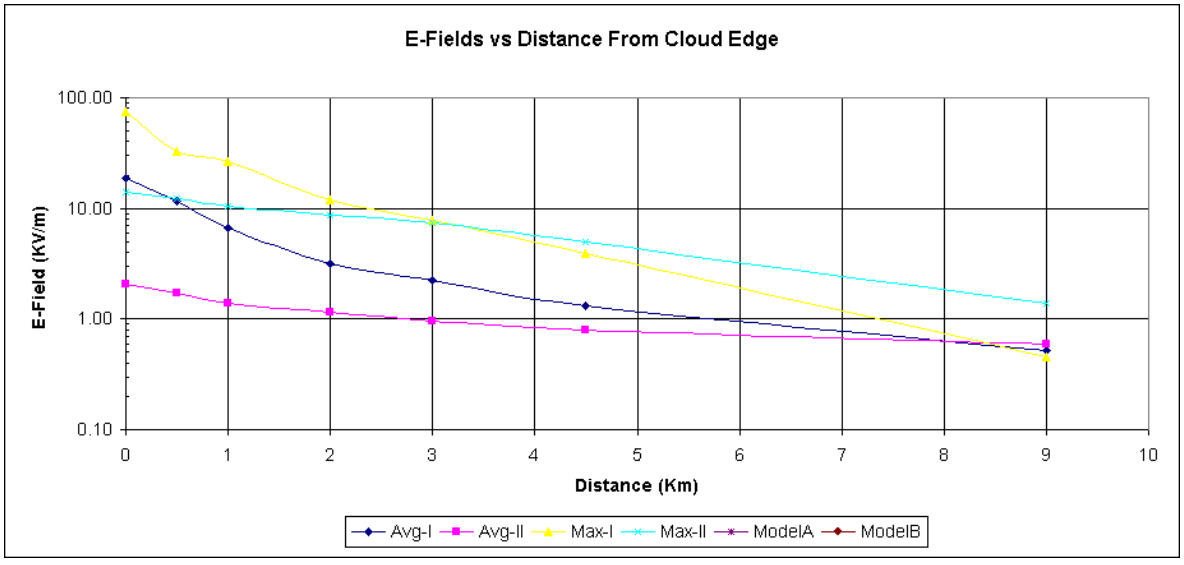

Figure 7.1 Electric field plotted as a function of distance from cloud edge. Avg I and Max I are average and maximum measurements from ABFMI, respecively and Avg II and Max II are from ABFM II.

retreated. Most of the ABFM II data set are from anvils or decaying systems but does include penetrations through some convective cores of moderate intensity. But for both

sets of observations by 9 km from the in-situ measured cloud edge both the average and maximum electric fields had decreased to <1.5 kV/m.

7.2 Debris Clouds

Although most of the analysis we have conducted and the attention in this report has focused on anvils, there were flights in debris clouds that warrant further consideration. As an aid in future investigations we have included files for debris clouds on the ABFM web site at http://www.mmm.ucar.edu/abfm/webpage/Scatter_Plots/Cutoff_m10/Data/ . This directory contains files for both anvils and debris clouds with different types of filtering. The file naming structure first shows the radar, then m10 stands for a radar cutoff of –10 dBZ, then codes for different filters. Files for debris clouds start with a "d". For example, WSR_m10_dclmin_000000 is the file from the 74C radar with –10 dBZ cutoff for debris clouds (d) with core (c), lightning (l) and minimum filtering. An example of scatter plots for debris clouds is shown in Figure 7.2 without filtering for lightning or nearby cores.

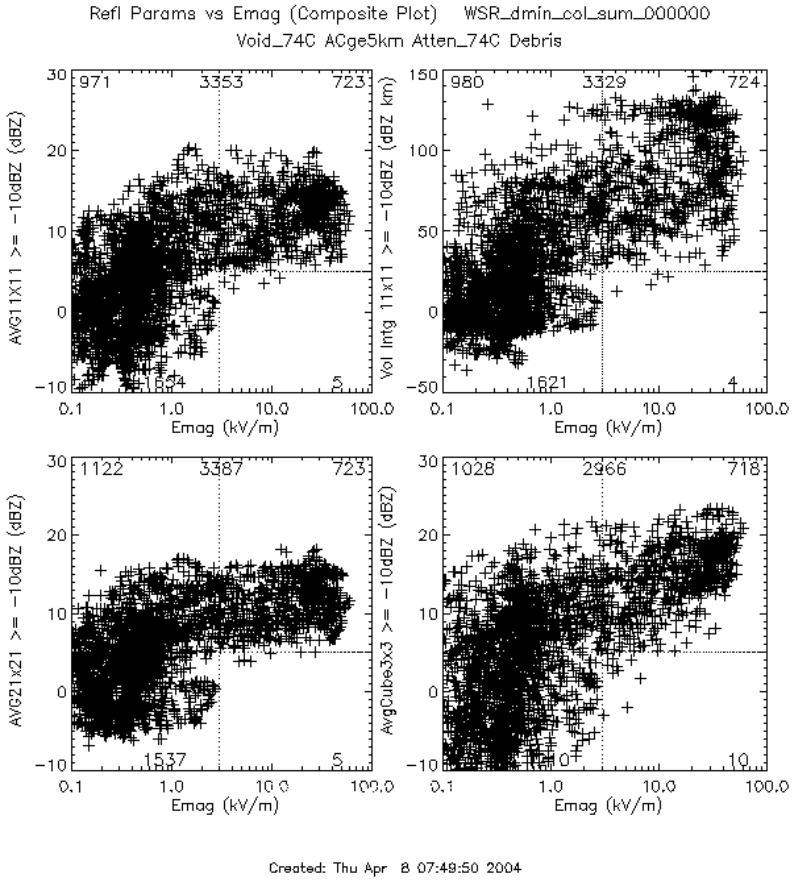

Figure 7.2 Scatter plot of reflectivity parameters as indicated versus Emag for debris clouds with minimum filtering for 74C attenuation, periods when the Citation was flying in the cone of silence above the 74C radar, and when the aircraft was at altitudes < 5 km MSL.

In the ABFM data set we have identified the following types of conditions as debris for the purposes of producing these scatter plots and Table 3.2 in Section 3. We consider "debris" as radar detected material remaining after lightning stopped in a once active thunderstorm that grew in a low shear environment. The resulting radar structure at 4, 7 & 10 km remains vertically stacked with no obvious anvil formation. We also included cases in which an individual convective cell grew and decayed leaving material in place, but successive convective cells propagate away from previous convective cells thus leaving a trail of "debris". Case 4 of June 5, 2001 is a good example. A vertical section through the line of cells for case 4 looks very much like an anvil (See MER plot 2050 to 2100 for this day or the AGU poster by Dye et al. 2002 on the Reports page), but the formation mechanism is different than an anvil. We also considered as "debris", stratiform regions that formed behind or adjacent to once active storms. Sometimes these regions advected over KSC from earlier deep convection over central Florida. There is ambiguity in trying to distinguish between debris, thick-layered clouds or wide spread embedded convection, such as a stratiform layer. Operationally it is not feasible to uniquely categorize most clouds during convective weather. Most thunderstorm-derived clouds away from the core may have simultaneous characteristics of anvil, debris and thick-layered cloud. Operationally, all applicable rules are applied to the same cloud, and

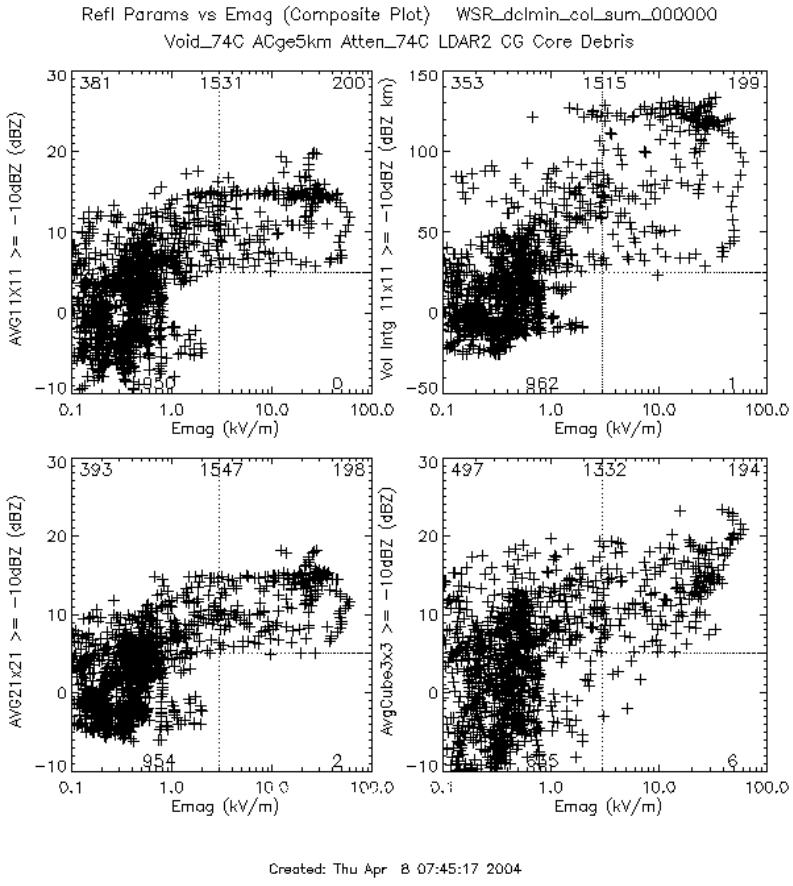

Figure 7.3 Same as figure 7.1 except the debris cloud data set has been filtered for nearby lightning and convective cores.

the most conservative result is used. But for purposes of understanding the behavior of different kinds of systems for ABFM and the relationship of electric field with reflectivity, it is useful to examine debris as a category separate from anvils.

Filtering the data in Figure 7.2 for nearby lightning and convective cores we obtain the results shown in Figure 7.3. It is apparent in Figures 7.2 and 7.3 that the scatter plots of different reflectivity parameters versus Emag for debris clouds have the same character as similar plots for the anvil data set. It would appear that a similar radar based rule might also be applied to debris cloud.

7.3 Correlation and Spectral Analysis of the ABFM Data Set

An initial correlation and spectral analysis of the entire ABFM data set was performed by Frank Merceret and is summarized in the Correl. & Spectral Analysis of Merged Data, F. Merceret on the ABFM Reports Page. The goal of this work was to get an overview of the correlations and spectral features of the electric field, particle concentration and 3 reflectivity parameters (reflectivity at the aircraft and 11x11 and 21x21 Column Averages) for possible future cloud type stratifications. The correlation analysis was performed to assess the degree of independence of the 10 s data points used in the Merged files.

The power spectral analysis showed that there is no dominant or preferred scale for cloud particle concentration, whether measured *in situ* or remotely by radar, or for electric field in the range from 2 to 32 Km. Indeed, the power spectra have the same characteristics as spectra of wind, temperature or humidity in random, turbulent flow. The spectral slopes are consistent with an Autoregressive 1 model having the same parameter values as obtained in the correlation analysis. The spectra support the use of the Autoregressive1 model to estimate the effective sample size for a given actual sample size. This further confirms that at the scales of interest here, we are dealing with scale-independent random red-noise processes. The values of the autoregressive parameter suggested that the effective sample size is about 10% of the raw number of 10 s samples used for computing mean quantities for electric field and cloud physics measurements, and about 4% for the 11x11 Column Averages. For standard deviations the effective sample size is larger -- about 20% and 8%, respectively.

The coherence analysis provided considerably less guidance. The confidence limits are so large that only limited conclusions may be drawn. Certainly the results indicate that at scales smaller than 10 km there is no significant coherence between any of the variables discussed. At scales approaching 30 km, the electric field appears to become somewhat coherent with cloud particle concentration and with the radar reflectivity at the position of the aircraft. This occurs at the long wavelength end of the analysis range and the number of points showing this tendency is too small to attempt fitting any kind of model to the data

8. SUMMARY OF RESULTS

Three field campaigns were conducted during the Airborne Field Mill Project II (ABFM) to investigate the relationships between electric field intensity, reflectivity and particle microphysics. The June 2000 and May/June 2001 campaigns were very successful in providing many measurements in anvils, convective debris, weak to moderate intensity deep convection and stratiform situations. The February 2001 campaign, conducted during conditions of severe drought in central Florida, provided limited measurements in thick clouds. As a result most of the analysis of ABFM observations have focused on anvils. We have gathered over or near KSC an excellent, unique data set, hitherto unavailable in the scientific community, with 3-dimensional electric field and detailed microphysical measurements in coordination with radar measurements. This data set is valuable for use in developing new Lightning Launch Commit Criteria rules but also for scientific investigations.

The primary results from ABFM II for anvils are as follows:

8.1 Electric Fields and Microphysics

- In regions of anvils with strong electric fields (in large degree also for debris cases), there was a surprising degree of consistency of observed particle concentrations in different size ranges from flight to flight.
- When strong electric fields (> 10 kV/m) occurred, the particle concentrations in all size ranges from tens of microns to several millimeters were high, but higher particle concentrations did not necessarily indicate regions of strong electric field.
- The smaller ice particles in the anvils (<50 μm) are primarily spherical thereby suggesting frozen cloud droplets. Almost all particles >100 μm are irregular with little evidence of riming except near storm cores. Pristine ice crystals were observed infrequently. Most particles > 500 μm have the appearance of aggregates. Long chains of aggregates were frequently seen suggesting enhancement of aggregation by the strong electric fields. Additional research could be done on this topic using this unique data set.
- Scatter plots of the anvil data set showed an unexpected, complex relationship between electric field and particle concentrations for all size ranges. For electric fields >3 kV/m up to the maximum of ~45 kV/m there is not much change of concentration with increasing field, but for Emag < 3 kV/m there are wide ranges of concentration for relatively small changes of field and a knee or inflection point in the plots.
- At this time, we have no explanation for the change in character of the electric field and particle concentration relationship near 3 kV/m.
- There was no evidence of supercooled liquid water being present in the anvils. This suggests that active electrification via the non-inductive charging mechanism is probably not occurring to any significant degree in these anvils.
- However, in several cases we observed the transition of anvils into a secondary development, a stratiform-like layer. During this secondary development electric fields persisted for extended periods of time and perhaps even intensified. Reflectivity persisted for long periods and sometimes increased, especially near the 0C level but

also aloft. (See Dye et al., (ICCP2004 preprint) for the example of the June 4, 2001 case and J. Willett's Final Report on the ABFM Web Report page). This topic warrants further investigation.

§ Even though this stratiform-like development occurred in some anvils, Column Averaged or Volume Integral reflectivity continued to provide good guidance on the presence of strong electric fields. The behavior of the Emag vs. reflectivity scatter plots was the same when these secondary development regions were included as well as when they were not.

8.2 Reflectivity and Microphysics

§ The relationship between reflectivity (of a 3 km cube near the aircraft) and particle concentration was found to be consistent with a power law in all size ranges from the smallest to the largest, but with more variation for the small and intermediate-sized particles than for the particles > 1mm.

§ The particles > 3mm, our largest size category, exhibited the best correlation with reflectivity, as expected.

§ The scatter plots of reflectivity versus particle concentration did not exhibit a complex behavior, unlike the scatter plots of electric field versus particle concentration.

§ Measurements near anvil edge clearly showed that particles extend out to or beyond the 0 dBZ radar contour and well beyond the 10 dBZ radar contour. As a result of ABFM observations the LAP changed the definition of "anvil edge" in the LLCC rules from +10 dBZ to 0 dBZ.

8.3 Electric Field Reflectivity

§ Strong electric fields were found to be associated with regions of higher reflectivity (>~5 to 10 dBZ) above the freezing level (assumed to be >= 5 km MSL), but higher reflectivity did not necessarily indicate regions of strong electric field.

§ The change in behavior of the character of the electric field and particle relationship near 3 kV/m carries over to and impacts the relationship of electric field with reflectivity and with electrical decay times.

§ Reflectivity at the aircraft location or in the 1x1 km column above the aircraft measured by the 74C and NEXRAD radars at anvil altitudes over KSC is not a suitable parameter for comparing to electric field strength. because of scan gaps between antenna sweeps of both radars. Additionally, strong temperature gradients can at times cause significant refraction of the radar beam.

§ A reflectivity parameter, the 11x11 or 21x21 Column average, was developed to minimize the effects of scan gaps and also to detect possible sources of strong electric fields in the large volume near but not at the aircraft location.

8.4 Electrical Decay Time Scale, Microphysics, Reflectivity and Electric Field

§ A simple model was developed to estimate the decay of electric field in the ABFM anvils based upon the observed particle size distributions. (Willett, Final Report,

2003). Because the model assumes constant microphysics during the field decay, the model times are considered upper limits.

- An electrical decay time scale, ETmScl (or τ_E in Willett's reports) is calculated for each 30 s average of aircraft data in anvil to estimate from the model the time for the electric field to decay from 50 to 0 kV/m. In the high field limit, ie. for fields approximately > 2 kV/m, the decay is linear.
- The particle cross sectional area, particularly in the size range 0.2 to 2 mm, largely controls the calculated electric field decay time scales for anvils in the model.
- The optical extinction coefficient (as well as electrical decay time) is also weighted toward mid-sized particles 200 to 2000 μm. See Willett (2003b) on Optical Extinction Coefficient.).
- The observed particle size distributions yield calculated electric field decay time scales ranged from 3 hours near the core of active storms to only a few minutes near the edge of anvils.
- Plots of the electrical decay time scale versus electric field show a large change in the plots near 3 kV/m similar to those of electric field versus particle concentration. This is a result of the change in character of the electric field and particle concentration relationship.
- Comparisons for case study days of electric field decay time scale from the model with observed decay times were generally consistent, but only one ABFM anvil case permitted a meaningful comparison.
- Neither reflectivity nor electrical time scale are a suitable proxy for electric field.

8.5 Consideration of Possible Radar Variables for an LLCC Rule

- Scatter plots of the 11x11 or 21x21 Column average versus the magnitude of the electric field, Emag have been useful for considering a possible radar based LLCC rule. Such plots have the behavior that for reflectivity less than some threshold value, no points with moderate or strong electric fields (> 3 kV/m) were observed.
- The 11x11 column is preferable to the 21x21 column for the purpose of calculating either average or another radar variable for use in an LLCC.
- The arithmetric average of dBZ values is preferable to a geometric average (in which dBZ is converted to Ze, averaged, and then converted back to dBZ), because the geometric average gives most weight to the very largest reflectivity. Similarly this is true for the maximum reflectivity.
- The11x11Volume Integral (the product of the 11x11Column average and the average 11x11Thickness) was found to have a smaller False Alarm Rate than the 11x11Column average. The volume integral was also less sensitive to the reflectivity cutoff being used, -10 or 0 dBZ and therefore more robust.
- At this time, the 11x11Volume Integral appears to be the most promising radar variable for use in an LLCC rule.
- If the primary consideration is to prevent statistical bias, a cutoff threshold for the radar measurements of –10 dBZ is preferable to a 0 dBZ cutoff for use in calculating column average or anvil thickness.

- There was considerable debate about whether a cutoff of –10 dBZ or a cutoff of 0 dBZ was preferable for use in an LLCC. This is a topic for further investigation and discussion.
- An examination of the entire ABFM data set (not just anvils) showed that electric field falls off rapidly from cloud edge. By 9 km distance from the cloud edge electric fields are <1.5 kV/m.
- For debris clouds, the scatter plots of reflectivity parameters versus electric field were very similar in nature to the scatter plots for anvils. A radar based LLCC for debris clouds might be very similar to the one presently being developed for anvils.

ACKNOWLEDGEMENTS

We gratefully acknowledge support from the National Aeronautics and Space Administration (Kennedy Space Center) and the National Reconnaissance Office, and the help and encouragement of John Madura and Frank Merceret of the KSC Weather Office. We wish to thank Eric Defer, now at the National Observatory of Athens in Greece, for his help in the field campaigns and being instrumental in the early development of the ABFM Web site and processing and display of measurements. We thank Bill Hall for development of software and processing of the particle measurements. Geoff Dix, Michael Dye and Dan Adams made the ABFM Web site an exceeding useful tool. Mike Stewart, Scott Podgorny, and Bill Koshak of MSFC provided superb support with the field mill measurements and calibration. We thank Dennis Boccippio for his insight and work on ROC and Bivariate analysis. We thank David Delene, Martin Brown and Jeff Schild for help in processing and making available the UND Citation data. We thank Penny Warfel for turning a poorly spelled and formatted collection of sections into a neat, presentable document. And last but definitely not the least, we acknowledge the fantastic help of the entire ABFM team for untiring help in the field campaigns and later analysis and especially for stimulating discussion throughout.

REFERENCES

Breed, D. W., and J.E. Dye: The Electrification of New Mexico Thunderstorms, Part 2. Electric Field Growth during Initial Electrification. *J. Geophys. Res*., **94,** 14,841-14,854, 1989.

French, J.R., J.H. Helsdon, A.G. Detwiler, and P.L. Smith, 1996: Microphysical and Electrical Evolution of a Florida Thunderstorm. Part I: Observations. J. Geophys. Res., 101, 18961-18977, 1996.

Dye, J.E., J.C. Willett, W.D. Hall, E. Defer, S. Lewis, D.M. Mach, M. Bateman, H. Christian, C.A. Grainger, P. Willis and F.J. Merceret, The Decay of Electric Field in Anvils: Observations and Comparisonwith Model Calculations, Proc. 12th Internat. Conf. on Atmosph. Electr., Versailles, France, June 9-13, 2003.

Dye, J. E., J. J. Jones, W. P. Winn, T. A. Cerni, B. Gardiner, D. Lamb, R. L. Pitter, J. Hallett, and C. P. R. Saunders: Early Electrification and Precipitation Development in a Small, Isolated Montana Cumulonimbus. *J. Geophys. Res*., **91**, 1231-1247, 1986.

Koshak, W.J., J.C. Bailey, H.J. Christian, and D.M. Mach; Aircraft electric field measurements: Calibration and ambient field retrieval; J. Geophys. Res., **99**, 22781-22792; 1994.

Mach, D.M. and W.J. Koshak, General Matrix Inversion Technique for the Calibration of Electric Field Sensor Arrays on Aircraft, Proc. 12th Internat. Conf. on Atmosph. Electr., Versailles, France, June 9-13, 2003.

Schild, J. J., Liquid Water in Thunderstorm Anvils over Kennedy Space Center, Florida during the Summer 2001 ABFM Field Campaign, Master of Science Thesis, University of North Dakota, Grand Forks, North Dakota, August 2003

Willett, J.C., Electrical Decay Estimates in Anvil Clouds, Report No. 1 of 2 under contract No. CC-90233B, submitted to NASA Kennedy Space Center Dec 28, 2001.

Willett, J.C., Electrical Decay Estimates in Anvil Clouds, Report No. 2 of 2 under contract No. CC-90233B, submitted to NASA Kennedy Space Center, Apr 11, 2003.

Willett, J.C., Electrical Decay Estimates in Anvil Clouds No. 3, Final Report under contract No. CC-90233B, submitted to NASA Kennedy Space Center, Oct. 31, 2003.

Willett, J.C., Electrical Decay Estimates in Anvil Clouds, Report No. 3, Final Report under contract No. CC-90796B, submitted to NASA Kennedy Space Center, Oct. 31, 2003.

Willett, J.C. and J.E. Dye, A Simple Model to Estimate Electrical Decay Time in Anvil Clouds, Proc. 12th Internat. Conf. on Atmosph. Electr., Versailles, France, June 9-13, 2003.

Appendix A
UNIVERSITY OF NORTH DAKOTA
CESSNA CITATION II RESEARCH AIRCRAFT

C. A. Grainger
University of North Dakota

1. INTRODUCTION

The University of North Dakota owns and operates a Cessna Citation II aircraft (N77ND) for the purpose of atmospheric research. This aircraft type has a number of design and performance characteristics that make it an ideal platform for a wide range of atmospheric studies. The Citation II is a twin-engine fanjet with an operating ceiling of 43,000 feet (13.1 km). The turbofan engines provide sufficient power to cruise at speeds of up to 340 knots (175 m s-1) or climb at 3300 feet per minute (16.8 m s- 1). These high performance capabilities are accompanied by relatively low fuel consumption at all altitudes, giving the Citation an on-station time of up to 4 hours or more, depending on mission type. Long wings allow it to be operated out of relatively short airstrips and to

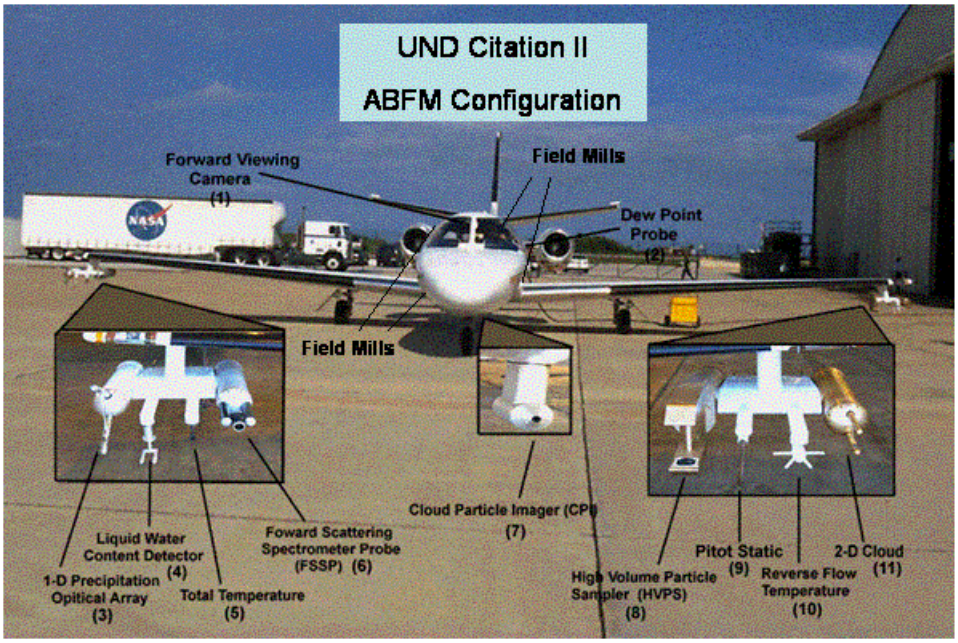

Figure A.1 Photograph of the UND Citation as configured for ABFM

sbe flown at the slower speeds (140 kts/72 m s-1) necessary for many types of measurements. The Citation is certified for flight into known icing conditions. The cabin measures approximately five feet in diameter and more than 16 feet in length. The

minimum flight crew is pilot, co-pilot and data system operator. Two additional seats are available for scientific observers or additional instrumentation specialists.

A series of structural modifications have been made to the basic airplane. These include the following: 1) pylons under the wing tips for a variety of probes in the undisturbed air flow away from the fuselage; 2) a heated, 5-port radome for wind measurement; 3) and an air inlet port and manifold for air sampling inside the pressurized cabin. A summary of the operating characteristics of the aircraft is given in Table A.1.

TABLE A.1
Operating Characteristics of the Citation II

Ceiling	13.1 km	(43,000')
Endurance (plus reserves)	up to 4.5 hours	
Empty Weight (including Std. instrumentation)	3888 kg	(8554 lbs)
Max Takeoff Weight	6591 kg	(14,500 lbs)
Range (not including reserves)	2500 km	(1350 nm)
Top Speed (True air speed, in research configuration)	630km h^{-1}	(340 kts)
Typical Sampling Speed (indicated)	80 m s^{-1}	(160 kts)
Fuel Consumption (Typical cruise configuration)	362 kg h^{-1}	(800 lbs h^{-1})
Time to Climb from Sea Level to 3.0 km at Max Takeoff Weight	4 min	
Time to Climb from Sea Level to 7.6 km (25,000') at Max Takeoff Weight	13 min	
Time to Climb from Sea Level to 10.7 km (35,000') at Max Takeoff Weight	24 min	
Takeoff and Landing Distance (most airports)	less than 1.9 km	(6000')
Total Power Available for Instrumentation	450A at 28 VDC	
Research Power Available	35A 60 Hz 15A 400 Hz 160A 28 VDC	

2. INSTRUMENTATION

The research instrumentation configuration used during the ABFM is listed in Table 2. The Instrumentation is described in more detail in Table 3. Typically, the equipment carried on any given research project will differ somewhat from the description given here. The installation of instruments provided by other investigators can be accommodated, subject to space, weight and electrical requirements. A variety of 19-inch racks are available to accommodate standard instruments.

Table A.2
Summary of Measurement Capabilities as used in ABFM

State Parameters	
Temperature	Rosemount Total Temperature
Dew Point Temperature	EG&G Cooled Mirror
Static Pressure	Rosemount
Cloud Microphysics	
Cloud Droplet Spectrum	PMS FSSP
Cloud Particles	PMS Optical Array 1D-C
Cloud Particles	PMS Optical Array 2D-C
Cloud particles	SPEC Cloud Particle Imager
Precipitation Particles	SPEC HVPS
Liquid Water Content	PMS King
Supercooled LWC	Rosemount Icing Rate Meter
Air Motion and Turbulence	
Horizontal, Vertical Wind	Ported Radome, Inertial Navigation System
Attack and Sideslip Angles, Airspeed	Ported Radome, Differential Pressure Transducers
Aircraft Parameters	
Heading, Pitch, Roll, Ground Speed, Position, Vertical Acceleration	Applanix POS-AV Strap-down Gyro and Accelerometers with integrated GPS
Cabin Pressure	Setra
Electric Fields	
Electric Fields	Six NASA Electric Field Mills

Meteorology

The basic instrumentation package measures temperature, dew point temperature, pressure, wind and cloud microphysical characteristics along with aircraft position,

attitude and performance parameters. The three-dimensional wind field is derived from measurements of acceleration, pitch, roll and yaw combined with angles of attack and sideslip and indicated airspeed. The aircraft parameters are supplied by an Applanix POS-AV strap-down gyro system with integrated global positioning system (GPS). Strap-down accelerometers provide lateral and longitudinal aircraft accelerations. Turbulence intensity can be derived from differential pressure transducers and accelerometer outputs. Cloud microphysical measurements are made with an array of Particle Measuring Systems probe s (FSSP, 1D-C, 2D-C) mounted on the wing-tip pylons. These probes measure concentrations and sizes of particles from one micrometer to several millimeters in diameter. In addition, there are probes to measure both liquid water content and icing rate.

For the ABFM project, an array of six electric field mills was installed on the aircraft. Four of these mills were located just aft of the cockpit and two more near the tail of the airplane. The output from these mills, when put into a solution matrix, yielded the three components of the electric field relative to the aircraft.

3. REMOTE SENSORS

A forward or side-looking video camera is also used to provide a visual record of flight conditions. A Bendix-King vertical profiling forward-looking weather radar can be viewed in the cockpit and recorded on video tape.

4. DATA ACQUISITION DISPLAY

The data are sampled at various rates from 4 to 200 sec^{-1}. The sampling is controlled by the on-board computer system which also displays the data in real time in graphic and alphanumeric formats while recording them on magnetic tape. The data can also be telemetered to a ground station and displayed in real time, or data may be telemetered from the ground to the aircraft. The data system is based on a project-customized windows system to allow flexibility in data acquisition and instrumentation in order to accommodate specific research demands.

5. AIR PARCEL TRACKING

The data system can also run a "pointer" algorithm that can be set to track the three-dimensional advection of up to three separate air parcels. This allows the aircraft to sample in a Lagrangian frame of reference.

6. FIELD SUPPORT

When in the field, the Citation is accompanied by a mobile operations support trailer. This vehicle houses technical support facilities, including calibration equipment for on-site quality control, and computer systems. The meteorological data collected on a research flight can thus be processed and examined within a few hours.

Table A.3
UND Citation Instrumentation Specifications

Parameter Measured	Instrument Type	Manufacturer & Model #	Range	Response Time	Accuracy	Resolution
Temperature	Platinum Resistance	Rosemount Model 102 Probe	-65°C to +50°C	1 s nominal	0.5°C	0.03°C
Dew Point	Cooled Mirror	EG&G Model 137	-50°C to +70°C	2°C S^{-1}	0.5°C>0°C 1.0°C<0°C	0.03°C
Static Pressure	Absolute Pressure	Rosemount 1201F1	0 to 1034 mb	15 ms	3.1 mb	0.25 mb
Altitude	GPS	Applanix	0 to 20 km	10 msec update	0.1 km	1 m.
Attack Angle and Sideslip	Differential Pressure	Validyne P40D	34.5 mb	20 ms	0.09 mb (0.05°)	0.02 mb (0.01°)
Indicated Airspeed	Differential Pressure	Rosemount 1221F	0 to 172 mb m^{-2}	10 ms	0.55 mb (0.8 m s^{-1})	0.04 mb (0.06 m s^{-1})
Heading	POS	Applanix	0-360°	10 ms update	12 arc min	6 arc min
Pitch, Roll	POS	Applanix	-90° to +90°	10 ms update	2 arc min	0.25 arc min
Vertical Acceleration	POS	Applanix	-10 to 30 m s^{-2}	42 ms	0.1 m s^{-2}	0.01 m s^{-2}
Lateral, Longitudinal Acceleration	POS	Applanix	5.0 m s^{-2}	10 ms	0.1 m s^{-2}	0.002 m s^{-2}
Ground Speed	POS	Applanix	0 to 500 m s^{-1}	10 ms update	0.5 m s^{-1}	0.05 m s^{-1}
Position	POS	Applanix	90° Lat 180° Long	10 ms update	0.1 km	1 m
Liquid Water Content	CSIRO Liquid Water Detector	PMS	0-9 g m^{-3}	0.05 s	5%	0.005 g m^{-3}
Icing Rate	Vibrating Cylinder	Rosemount Model 871FA	0-0.0251 cm before recycle	7 s recycle	±.013 cm	0.003 cm
Cloud Droplet Spectrum	Forward Scattering Spectrometer Probe	Particle Measuring Systems (PMS) FSSP-100	0.5-47μm	4 Hz sampling	-	0.5-3.0μm variable
Cloud Particles	Optical Array Probe 1D-C	PMS OAP-230X	20-600 μm	4 Hz sampling	-	20 μm
Cloud Particles	Optical Array Probe 2D-C	PMS OAP-2DC	30-960 μm	4 Hz sampling	-	30 μm

Appendix B

ELECTRIC FIELD MEASUREMENTS

Monte Bateman and Douglas Mach
NASA Marshall Space Flight Center

1. INTRODUCTION

Measuring electric field with an aircraft is a particularly tricky measurement to make. The electric field is the only airborne measurement where the aircraft itself becomes part of the sensor. Thus, the challenge is to measure the vector electric field as if the aircraft was not present. Through careful calibration and various mathematical techniques, we can recover that field and remove the contaminating contribution from the aircraft. The aircraft alters the ambient electric field because: (1) it is a conductor, and (2) it accumulates electrical charge when it impacts cloud particles. The electric field due to charge on the aircraft must be accounted for and removed from the measurements. This contaminating field is modulated by the geometry of the aircraft and is complicated because aircraft are inherently non-spherical. In order to characterize the field from a thunderstorm, we need to measure all the vector components of **E** (Ex, Ey, and Ez) and account for the field due to charge on the aircraft (Eq). Thus, to measure all 4 components we need at a minimum 4 sensors. However, making redundant measurements allows us to test and see if any sensors are being fouled by local effects, such as a transient cloud of charge that the aircraft happened to be emitting. During this program, the Citation carried 6 electric field sensors, called field mills.

2. INSTRUMENTATION

An electric field mill is an instrument that measures the vector component of the electric field that is normal to the sensor. The type of mills that were used are rotating-vane field mills physically similar to those described by Winn [1993]. Our mills were designed by Mike Stewart (NASA/MSFC/UAH) to be deployed on aircraft. They are built to be tolerant of the environmental extremes encountered outside an aircraft flying in a thunderstorm. The NASA/MSFC mills are especially low noise, high dynamic range, and have digitization inside the instrument. The low noise properties come from careful manufacture of the front-end sensor, internal shielding to protect against RF noise or electrical noise from other aircraft systems, and carefully balanced analog signal processing prior to digitization. These mills achieve a dynamic range of 120dB by using two separate amplifiers with different gains, which have overlapping ranges. This allows us to measure fields of less than 1 V/m up to 150 kV/m. The high resolution comes from using 16-bit A/D converters, which gives us 0.25 V/m per bit resolution on the high gain channel. The data are digitized inside the mill, close to the sensor source, so as to not introduce aircraft electrical noise in the measurements. The mills are commanded and synchronized by a central data collection computer. They are synchronized to within 16ms of each other; the overall timing knowledge is within 50 ms of UTC. The data are recorded by the central computer each second.

3. CALIBRATION

3.1 Mill Calibration

Before any field program, each mill is calibrated by placing it in a known electric field in the lab. This field is created using two parallel conducting plates across which a known high voltage is applied. The sensor end of a field mill is placed in a hole in one of the plates, such that the top of the mill head is flush with the plate. This keeps a known, uniform field between the two plates. Each mill is then subjected to about 10 different known field values across both polarities. The field mill voltage out for each field value is recorded and then used later in processing the data. Each mill is assigned a serial number when manufactured (the number is burned into the mill's firmware) and is recorded in the data stream. So no matter where a mill is on the aircraft, its absolute calibration can follow, based on the mill serial number recorded in each data stream.

3.2 Mill Placement

The 6 mills are located on the aircraft as follows: The front 4 mills are in a ring around the fuselage between the cabin door and the cockpit window. The upper two mills face port and starboard at an angle that is about 30 degrees above the horizontal. The lower two mills face port and starboard at an angle that is about 20 degrees below the horizontal. There are two aft mills. One is located on top of the fuselage, about halfway between the vertical fin and the port (left) engine nacelle. It looks upwards at roughly a 45 degree angle. The other aft mill is on the bottom of the fuselage, nearly on the centerline, about 1m aft of the trailing edge of the wing. As previously mentioned, when in cloud, the aircraft charges, and because the aircraft paint is an insulator, (meaning that charges are not free to move around) the paint on the aircraft can trap charge and hold on to it for long periods of time. To mitigate this effect close to the mills, the aircraft has been painted with conductive paint in a 1-m-diameter circle around each mill location.

3.3 Geometric Calibration

We need to be able to determine the external field from the multiple mill outputs. To do this, we must derive a geometric calibration (form factor) for the specific aircraft. This consists of two steps, relative and absolute calibrations. These calibrations accomplish two things: (1) Convert 6 mill outputs to vector field components, Ex, Ey, Ez, and Eq (in an aircraft-relative coordinate system), and (2) “cancel out" the field component due to charge on the aircraft, Eq. The details of these calibrations are beyond the scope of this document; see Mach and Koshak [2003] for details.

4. UNCERTAINTY

Once the aircraft is calibrated, the major source of errors in field determination is due to slight errors in the aircraft charge component (Eq). When the aircraft is out of cloud, the charge on the aircraft is usually very small and we are quite certain about the electric field (within +/- 10%). When the aircraft penetrates a cloud, however, the errors increase

significantly. The greatest problems are when the actual fields are very low and the field due to charge on the aircraft (Eq) is very high (say ten times the ambient electric field). In those cases, even small errors in the calibration can become significant. In extreme cases, the errors can be as large as the actual fields. But the data can be quality controlled by monitoring the Eq component from the solution. This gives us an idea how much charge is on the aircraft, and we can gauge the uncertainty in the solution for the ambient field. From examinations of the fields produced during the ABFM program, we estimate that when Eq is low, the typical field errors are no more than about 20% overall. Individual vector components will react to errors in the charge determination differently. If there are several mills that contribute to a component (which is the case for Ey and Ez), errors in individual mill outputs have a tendency to cancel out. For vector components that essentially use only one or two mills (like Ex), errors in a mill output are more likely to create problems for that field component. So, the Ey and Ez field components are most accurate (within 20%) and that the Ex component to the electric field is much less accurate (errors much greater than 20%).

REFERENCES

Mach, D., and W. Koshak, General matrix inversion technique for the calibration of electric field sensor arrays on aircraft platforms, in Proc. ICAE, Paris, 2003.

Winn, W. P., Aircraft measurement of electric field: Self-calibration, *J. Geophys. Res*, **98**, 6351 - 6365, 1993.

Appendix C

DESCRIPTION OF THE MICROPHYSICAL INSTRUMENTS USED FOR ABFM

Jim Dye

A number of different probes were used to measure particles during the ABFM project. The following is a very brief overview of the different instruments, how they performed and some issues to consider when examining the time series plots of particle concentration that exist on the NCAR ABFM Web Site. For most instruments discussed here there are links to Bulletins from the NCAR Research Aviation Facility that give a more complete description of that instrument.

The instruments used were:

1. PMS Forward Scattering Spectrometer Probe (FSSP)

Nominal range 3 to ~50 microns in 15 bins The FSSP sizes and counts particles by measuring light scatter in the forward direction. The voltage pulses produced are sized and sorted into 15 bins in a pulse height analyzer. The instrument was designed to count and size cloud droplets which are spherical and water. In recent years some researchers believe that the FSSP output gives a reasonable idea of total concentration in clouds wholly composed of ice, but not mixed phase. We include the total concentration from the FSSP as a measure of the smallest ice in the cloud. Uncertainty in the total concentration measurement is unknown, but could be a factor of two or perhaps more. Paul Field has recently shown that artifacts can be produced by breakup of ice particles colliding on the tips of the FSSP, but estimated that the uncertainty is probably less than a factor of two.

ISSUES: The FSSP often has noise in the first bin or two, because the threshold for the first bin is set close to the signal noise level (which can be variable in different conditions). Hence out of cloud you might see some response from the FSSP even though the 2D shows nothing. I have seen this for a couple of days in 2000 and in 2001. Additionally, during the early part of the May/June 2001 campaign there was an intermittent power supply that sometimes functioned and sometimes not.

For more detailed description of the FSSP go to: fssp100.html

2. Particle Measuring Systems (PMS) 2D-Cloud Probe (2D-C)

Range 33 um to ~1 mm on the UND Citation The 2D-C produces shadows of particles passing through a collimated laser beam by recording the time sequence of diodes of a 32 element diode array which are shadowed by passage of the particle. By scanning the array at a speed proportional to the aircraft true airspeed, an image of each particle is generated. The sample volume is size and true airspeed dependent, and must be accounted for in processing. Substantial processing must occur to determine

concentrations and size distributions. The probe has 2 buffers, which allows one buffer to collect data, while the previously filled buffer is downloaded. On the UND system 4 buffers/sec can be recorded.

ISSUES: In both 2000 and 2001 there were some power supply problems, meaning loss of data. Frequently every other buffer is difficult to read and sometimes lost. This was particularly true in June 2001 for all flight days after the lightning strike on 10 June 2001. On occasion when the Citation was in strong E fields the probe tips apparently go into corona. When this happens artifacts are generated and the timing words which are essential for interpreting the data record are corrupted. The data cannot be recovered for those periods. These artifacts were fairly common during flights in which high fields were encountered, but did not always happen when the fields were strong. Undersampling of particles in the lower range of the 2D probe is well known. It is a result of poor electronic time response and probability of detection when particles are near or only a little larger than the size of the elements of the diode array. Concentrations of particles for sizes less than ~100 microns are underestimated and sometimes this portion of the size distribution is not included in size distributions. We have included them for completeness, but the absolute concentrations should not be trusted.

For further description of operation of the 2D probe go to: 2d Probes

For samples of 2D particle images for each flight day of the May/June 2001 campaign go to: 2D samples. Then select the year of interest and then the flight day. This brings up a list of images from that flight. The image of every 1/100th particle image of each 2D buffer is shown.

3. PMS 1D-Cloud Probe (1D-C)

Range ~20 to 600 microns
The 1D probe, like the 2D probe, has a 32 element diode array. But instead of scanning the array and recording occulted diodes, the 1D electronics determines the maximum number of diodes occulted by each particle. This information is sorted and counted into different size bins of a pulse height analyzer. The first and last diodes are used to determine if a particle is wholly in the beam. Thus functionally only 30 diodes are used for sizing. Particle size distribution are recorded but without images of the particles.

ISSUES: We only recently started processing the 1D data, so we are not fully aware of any issues. Like the FSSP, there can be noise in the first couple of size bins, but so far I have not noticed this in the ABFM measurements. My impression is that for the ABFM project, the 1D probe may be the most reliable indicator of when the aircraft enters and leaves cloud. Like the 2D, under sampling of particles in the lower range of the 1D probe is well known. It is a result of poor electronic time response and probability of detection.

For more information on principles of operation of the 1D probe go to: 1D Probe

The 1D probe described in the above link is a probe with a 60 element array whereas the Citation probe has only 32 elements. Other features are much the same.

4. King Liquid Water Sensor

The King liquid water probe maintains a wire element at a constant temperature and senses the power necessary to keep the element at a constant temperature. Because heat loss occurs in clear air as well as cloud, a "dry" term correction must be made.

ISSUES: Measurements by others in clouds containing only ice particles (no liquid particles) have shown that this sensor does respond fractionally to ice as well as water. Thus, its measurements should not be used as a measure of the supercooled liquid water in our anvil clouds.

For more information on this instrument go to: King LWC

5. Rosemount Ice Detector

This sensor is a small cylinder of a couple centimeters length and a few millimeters diameter which when in supercooled water becomes iced. A magnetostriction circuit determines the change in resonant frequency of the cylinder and the signal output is proportional to accumulated ice mass. When a preset threshold is reached the cylinder is heated to remove any accumulated ice and a new icing cycle is begun. This is the best measure we have for the possible presence of supercooled water in ABFM anvils.

ISSUES: At times spikes are observed in the signal. These are perhaps due to graupel or other large ice particles impacting on the cylinder.

For more information on this instrument go to: Ice Probe

6. SPEC Cloud Particle Imager (CPI)

This is a relatively new instrument, which in the hot, humid Florida environment required a lot of attention. When operating properly it produces spectacular images of ice particles and water drops. The CPI uses two crossed continuous laser diodes to sense when a particle is in the intersection of the two beams. Then a 30 mW laser diode is pulsed at ~20 nanosecond to capture the image of the particle (and any others in the path) on a 1024 x 1022 CCD array. Each element of the array is ~2.5 microns, so particles in focus show great detail including particle habit and any evidence of riming.

ISSUES: The sample volume of the CPI is small, roughly 2.5 x 2.5 mm square. Thus it captures images primarily in the range of ~20 microns to a few hundred microns, because the probability of triggering on larger ones is so small. Additionally this instrument is sufficiently new that so far we are not able to determine concentration independent of other measurements. Also processing and analysis of the data are extremely time

consuming. For ABFM we are using the measurements primarily for the images and information on particle types encountered during selected flights.
For more information on the CPI go to: CPI

7. SPEC High Volume Precipitation Spectrometer (HVPS)
This probe was designed to greatly increase the sample volume for larger particles. It's operation is somewhat similar to that of the 2D but is much more complex. It uses two linear arrays of 256 elements each with each element corresponding to 200 microns width in the sample volume. Thus, the entire width of the beam is almost 5 cm, meaning that particles as large as 5 cm can be imaged. The scan rate for sampling the array is slaved to the true airspeed so that the resolution along the line of flight is roughly 400 microns for airspeeds under 96 m/s.

ISSUES: During the June 2000 campaign the HVPS worked poorly, apparently due to misalignment of optics. However, during the Feb. 2001 and the May/June 2001 campaigns the HVPS worked very well and gives us excellent information on the large particles of the spectrum. In principal, determination of the sample volume and hence concentration should be relatively straightforward, but only a few investigators have used the HVPS so it is hard to address uncertainties at this time. In general there is relatively good agreement between the 2D and the HVPS in the crossover region of the two instruments. Like the 2D and 1D probes, the HVPS undersamples the small end of it's size range because the probability of detection is reduced when the particle size is not significantly larger than the distance between the elements of the array.
For more information on the HVPS go to: HVPS

EXAMPLE of a Composite Particle Size Distribution

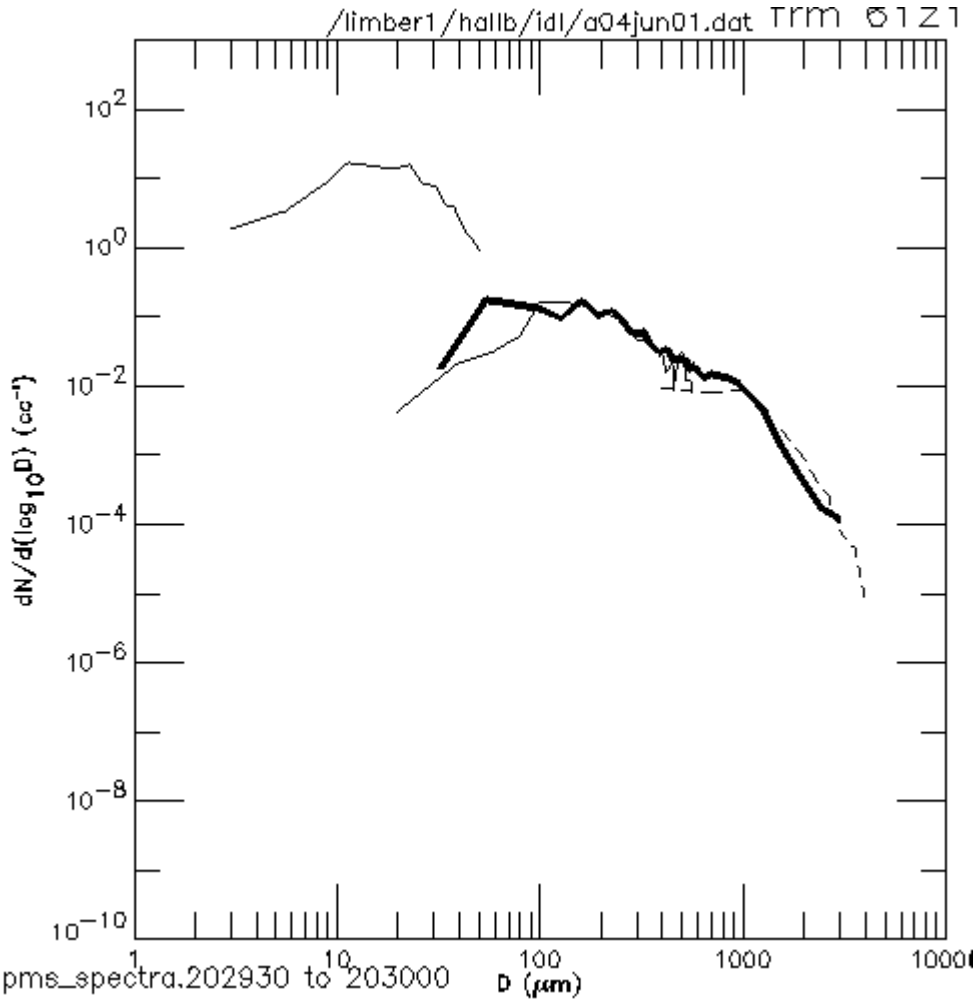

Figure C.1 Combined particle size distribution from measurements of the FSSP, 1D, 2D and HVPS for June 4, 2001 from 2029:30 to 2030:00. solid, light line in upper left is from the FSSP; solid, BOLD line is from the 2D; solid, light line near the 2D line is from the 1D; dashed line is from the HVPS.

Statistical Uncertainty in Particle Concentration Measurements

The following three particle size distribution plots for the 24June2001 case span a range of particle concentrations encountered during ABFM. The first case (1851:00) is one with relatively low concentration near the radar edge of the anvil, the second one (1852:30 is with intermediate concentrations and the last one (1856:30) is with large concentrations, particularly for sizes from 100 to 1000 microns. These three plots show statistical uncertainty in particle concentrations from the different particle probes as a result of counting statistics. The uncertainty was calculated following Cornford (1967) and is

based on poisson statistics. There are three traces for each instrument. The middle line is the best estimate, and the upper and lower lines (when distinguishable from the middle line) are the upper and lower 95% confidence limits. In many cases for our distributions the 95% confidence limits are no wider than the line width. Uncertainties appear mostly at the upper and lower size limit of each instrument where the number of counts are smaller.
NOTE: These are the uncertainties due to counting statistics. There are additional sources of uncertainty inherent in each instrument.

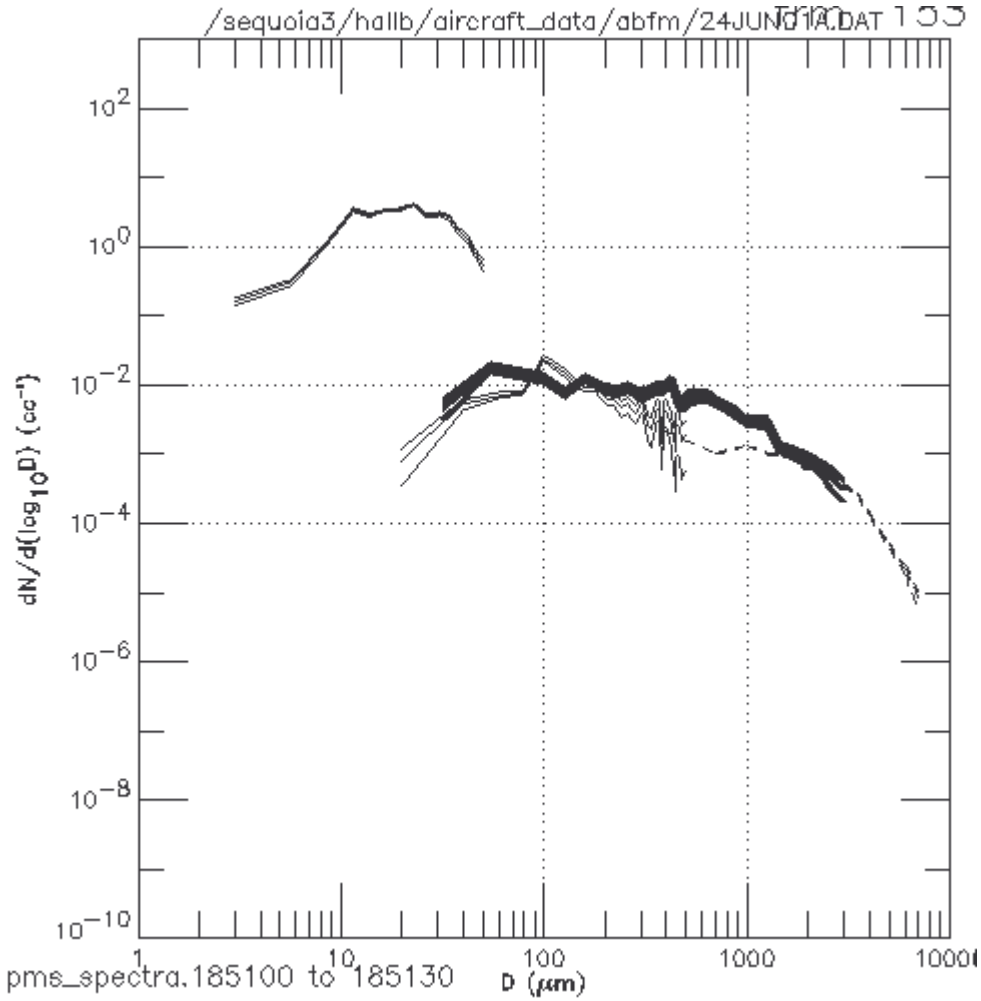

Figure C.2 An example for June 24, 2001 from 1851:00 to 1851:30 -- low concentrations

The uncertainty of the concentration measurements in any size interval (instrument defined bin limits) of the distribution is 1 +/- [1/sqrt(Ci)], where Ci is the number of counts measured by a given instrument in the size interval i. For example, if the measured number of counts in a given size interval is 100, the 95% confidence limits of that measurement are 110 to 90, i.e. 100(1 +/- [1/sqrt(100)]).

If the number of counts is 10, the uncertainty range is 13.2 to 6.8. If only 1 particle is detected in a give size interval, the 95% confidence limits range from 2 to 0.

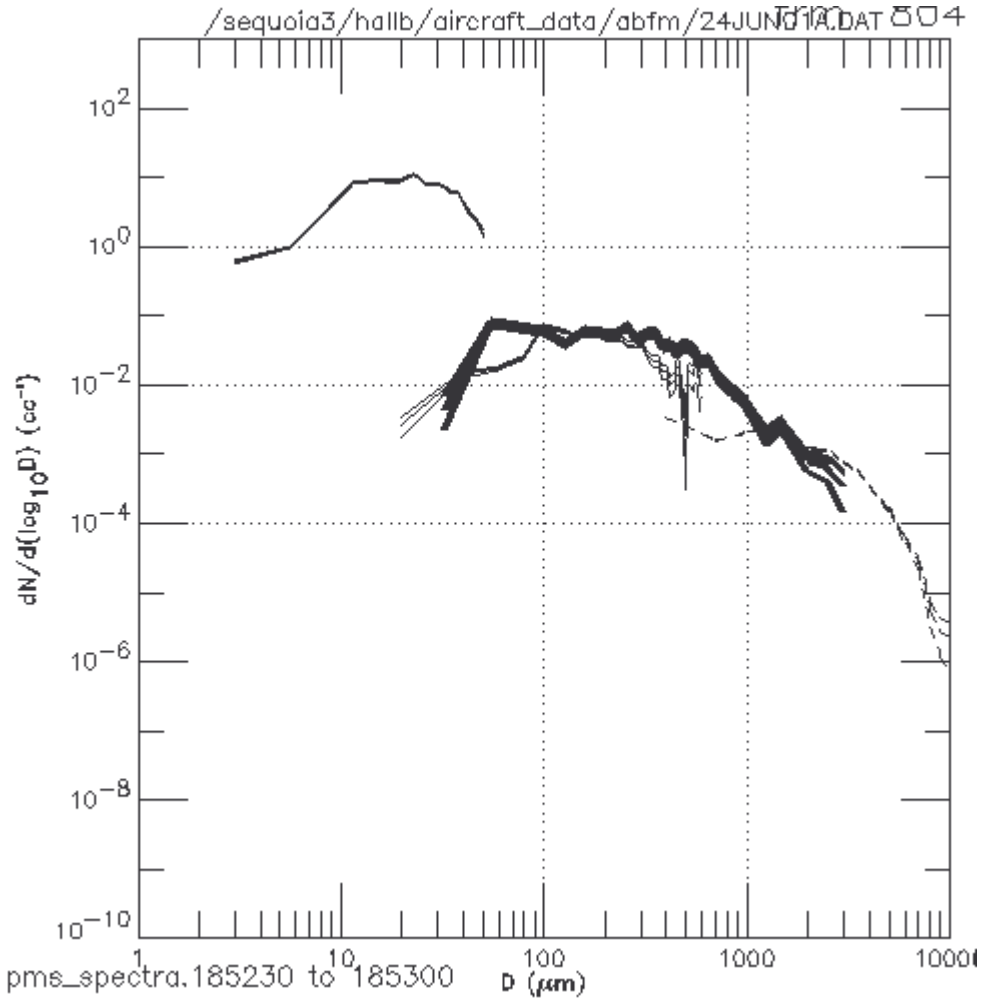

Figure C.3 An example for June 24, 2001 from 1852:30 to 1853:00 -- intermediate concentrations

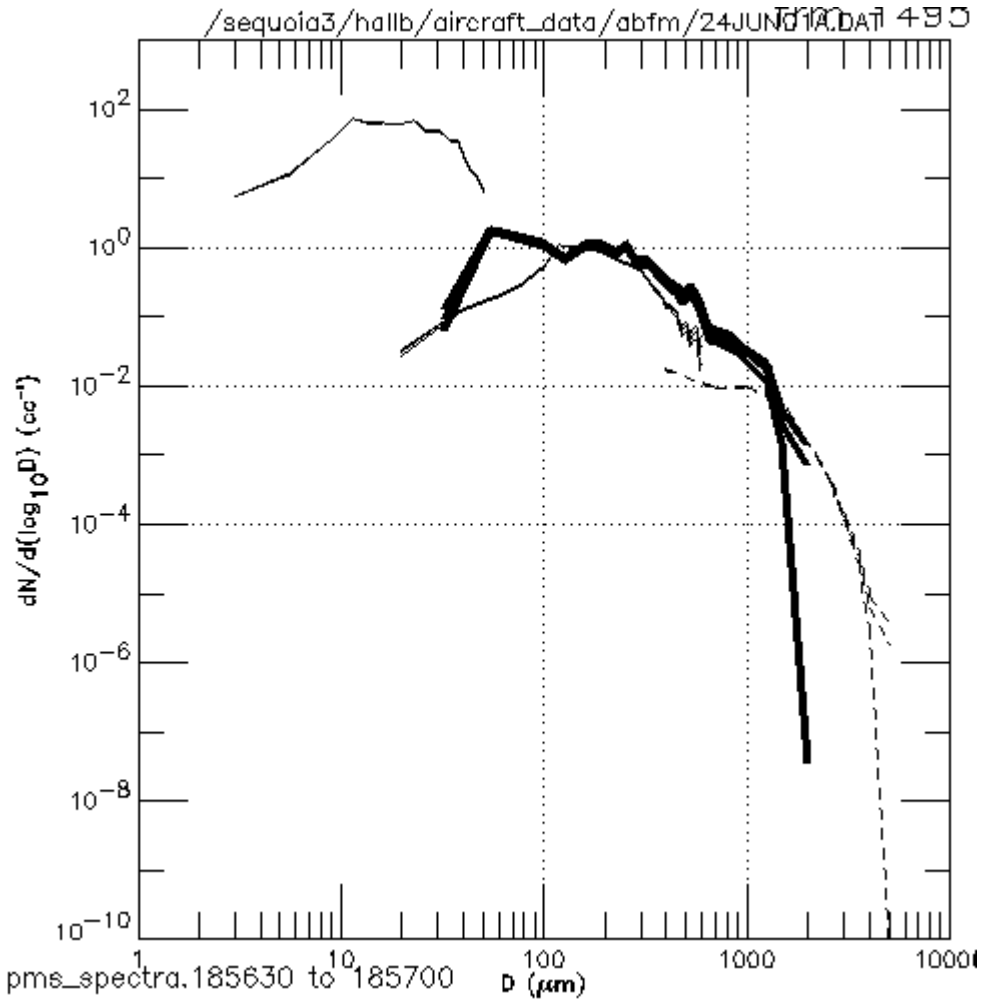

Figure C.4 An example for June 24, 2001 from 1856:30 to 1857:00 -- large concentrations

REFERENCE

Cornford, S. G., 1967: Sampling errors in measurements of raindrop and cloud droplet size concentrations. *Meteor. Mag*., **96**, 271-282.

Appendix D
WSR-74C RADAR

Frank Merceret and Sharon Lewis
Version 3 May 04 12:45

1. DESCRIPTION OF THE RADAR

1.1 General Description

The Eastern Range WSR-74C weather radar is located at Patrick Air Force Base (PAFB) about 30 km SSW of the launch complexes at Cape Canaveral Air Force Station (CCAFS) and Kennedy Space Center (KSC). The coordinates are 28 deg 15m 20.49s N, 80 deg 36m 19.87s W. The base of the antenna is 20m above mean sea level. It is used to support all operations at CCAFS and KSC (Boyd *et al.*, 2003)

The radar is a C-band (5.3 cm) horizontally polarized weather radar without Doppler capability. The peak power is 250 kW. The beam width is 1.05 degrees and the pulse width is 4 μs. The pulse repetition frequency (PRF) is 160 Hz. (CSR, 2000, Section 10.4). Each sample provided to the data processing software is an average reflectivity from sixteen pulses with four bin radial smoothing. The maximum range is from 256 km with a resolution of 2.5 km. The reflectivity is range normalized with 8 bit resolution. The least significant bit is 0.4 dBZ. (*ibid.*) Each scan is time tagged with the time the scan began using the Eastern Range GPS-based UTC timing system. A full volume scan takes about 2.5 minutes.

Operational radar products are generated in near real-time using the SIGMET/IRIS(r) system (*see* ibid.*;* Short, 2000). The ABFM program generated its own products rather than using the operational ones.

1.2 Scan Strategy

The scan strategy can be easily changed by modifying tables in the radar configuration file. The current operational scan strategy for the WSR-74C is shown in Figure D1 below taken from Short (2000). It was the one used for the ABFM program flights in 2001. An older configuration was inadvertently used during 2000. It is shown in Figure D2 also taken from Short (2000). In either case, the raw data files contain the actual elevation used for each scan. The scan strategy is implemented using an interleaved pattern. Beginning with the lowest elevation, a complete rotation of the antenna is followed by raising the elevation by two scan elevations, skipping the scan elevation between. This process continues until the highest elevation is reached. The antenna then steps downward completing the scan angles that were skipped on the way up. The advantage of this interleaving is that temporal changes are smoothed between adjacent scan angles when volume averages are computed.

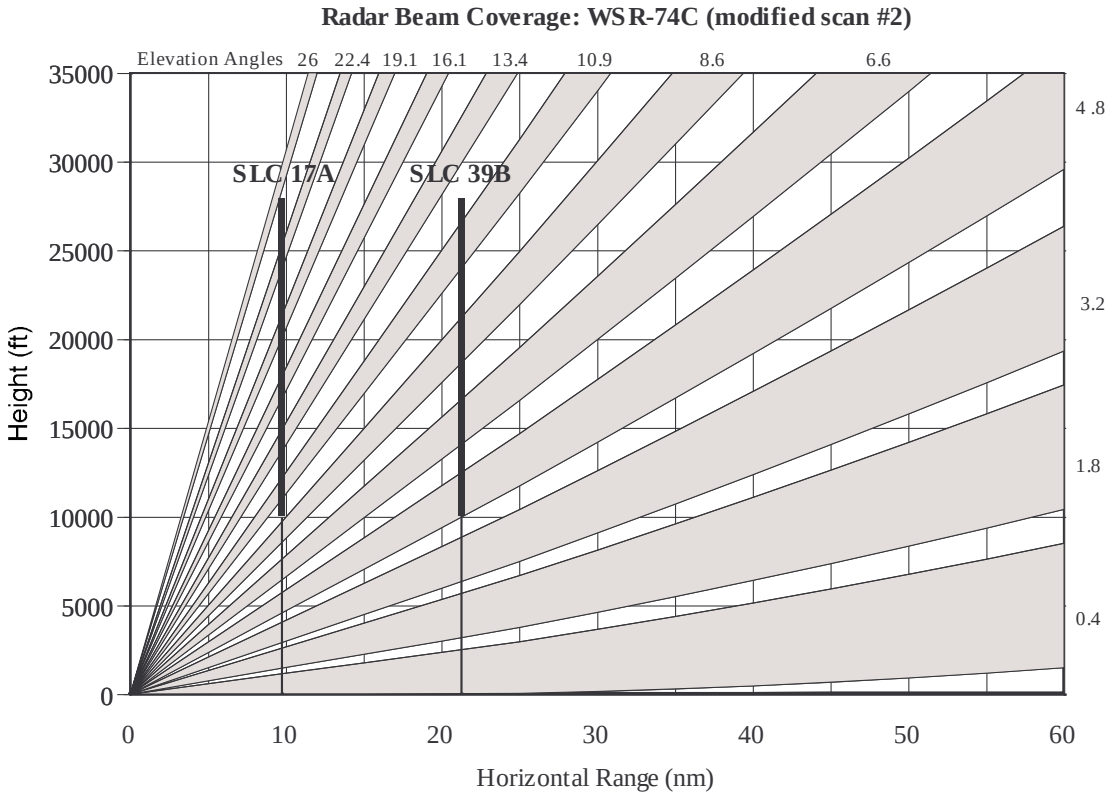

Figure D.1. Vertical cross-section of beam coverage by current WSR-74C volume-scan using 12 elevation angles. Ignore the label "modified scan #2". The elevation angle sequence is designed to produce vertical gaps between half-beamwidths that are constant with range at a fixed altitude. A beamwidth of 1.1° was used. The vertical lines indicate the locations of SLC 39B and SLC 17A relative to the radar. The line is thickened between 10 400 ft and 27 600 ft to emphasize the layer where mixed phase processes and electrification are most likely to occur within clouds. The elevation angles are 0.4°, 1.8°, 3.2°, 4.8°, 6.6°, 8.6°, 10.9°, 13.4°, 16.1°, 19.1°, 22.4°, and 26.0°.

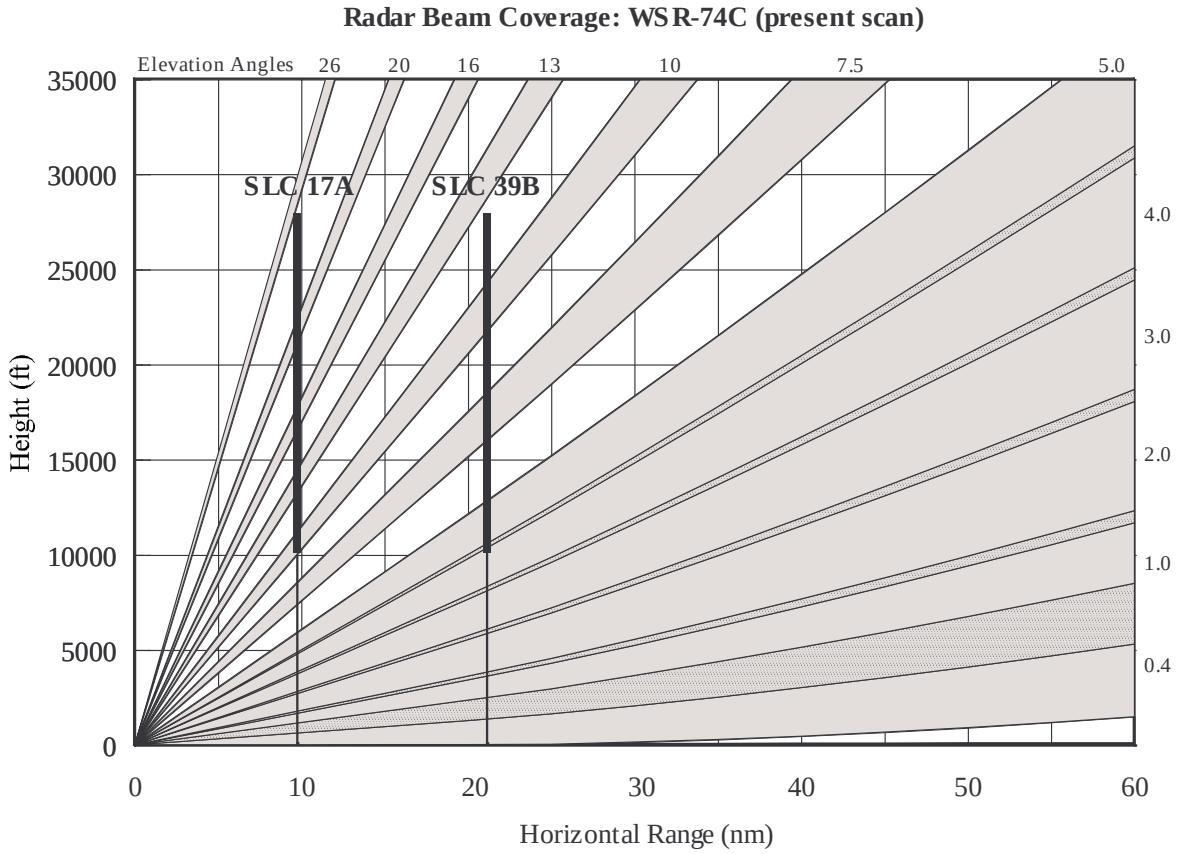

Figure D.2. Vertical cross-section of beam coverage by older WSR-74C volume-scan. Ignore the label "present scan". A beamwidth of 1.1° was used. The stippled pattern indicates overlapping coverage by adjacent beams. The vertical lines indicate the locations of SLC 39B and SLC 17A relative to the radar. The lines are thickened between 10 400 ft and 27 600 ft to emphasize the layer where mixed phase processes and electrification are most likely to occur within clouds. The elevation angles are 0.4°, 1.0°, 2.0°, 3.0°, 4.0°, 5.0°, 7.5°, 10.0°, 13.0°, 16.0°, 20.0°, and 26.0°.

1.3 Calibration

The WSR-74C receiver and digitizer are calibrated by direct signal injection from a calibrated signal generator. The transmitter power is calibrated using a calibrated power meter. There is no quantitative sphere or sun check done to verify antenna gain, but a qualitative sun check is used to verify pointing accuracy.

1.4 Errors and limitations

The sampling error based on 16 pulse averaging with a PRF of 160 Hz for a 5 cm radar is about 1.1 dBZ (*see* Doviak and Zrnic, 1993, section 6.1). The radial smoothing will reduce this error although quantitative calculation of the reduction is too complex to warrant inclusion here given the sources of random error including attenuation and propagation. The noise floor of the instrument is about -9 dBZ at a range of 100 km.

2. RE-ORDERING OF RAW DATA FOR SPRINT INGEST

To convert raw sweep data to a 225x225x20 km grid, the data were converted to universal format (uf) using the TRMM-RSL library. The gridding software, MMM-SPRINT, requires that uf data be in sequential order by elevation, so the interleaved scans were reordered before archiving in the uf format.

3. PRODUCTION OF CARTESIAN GRIDDED OUTPUT AND DISPLAY

The radar data in uf format was converted to Cartesian grid using NCAR's MMM-SPRINT. As provided, SPRINT uses a grid of 225 x 225 points. We chose to use 1 km grid spacing, so our gridded domains are 225 x 225 km. In the vertical, they typically are 1-20 km in 1 km steps. To avoid pre-judging what data might be useful in generating a radar-based lightning LCC, no filtering of the data was done during gridding. SPRINT was configured to perform a bi-linear interpolation with a maximum acceptable distance to relocate a closest point estimate of 0.2 km with no range interpolation. The reflectivity was converted from dB to a linear scale for interpolation. The WSR-74C and WSR-88D used the same input deck when running SPRINT.

The grids were determined by looking at the aircraft track and trying to specify a single grid that would contain the track for the entire flight. On some days, two different grids were needed to contain the track. The gridded reflectivities were produced as one file per volume scan. These data were recorded to CD and sent to NCAR for final processing.

The gridded volume scan data were used to produce Constant Altitude Plan Position Indicator (CAPPI) and vertical cross-section displays. CAPPIs were produced for low, middle and high levels of the clouds under investigation for each mission day. Typically these were near 4, 7 and 10 km altitude. The vertical cross-sections were made along the flight track of the aircraft and incorporated into combined MER (microphysics, E-field and radar) plots.

4. ABFM ISSUES

4.1. Attenuation

There are two primary sources of attenuation that could reduce the measured reflectivity enough to compromise the utility of the data for ABFM analysis: intervening precipitation and wetting of the radome. Both are strongly wavelength dependent.

Attenuation due to intervening precipitation obviously depends on the intensity of the precipitation. It also depends on whether the precipitation is liquid or frozen. In both cases it depends on the particle size spectrum. In the case of frozen precipitation it depends on the ice crystal type. As a result of these complexities, it is not possible to present a simple rule for estimating the actual attenuation in a specific case from reflectivity measurements alone.

It is possible to bound the attenuation by considering the worst case. If snow and both convective and stratiform rain are considered, a two-way attenuation envelope of the form

$$A\ (dB/km) = a10^{bZ\ (dB)}$$

will cover the worst case where A is the two-way attenuation rate and a and b are wavelength dependent constants. At the 5 cm wavelength of the WSR-74C, $a = 5x10^{-5}$ and b = 0.0875. The model is valid for intervening reflectivities from 30 to 60 dBZ which encompasses the region from negligible attenuation (0.02 dB/km) at 30 dBZ to maximum likely reflectivity (60 dBZ) at which the attenuation is 9 dBZ/km.

Attenuation also occurs when the radome of the radar gets wet because the water coating absorbs microwaves. The amount of attenuation depends on whether the radome is treated with a hydrophobic coating. The two way loss, L (dB), can be modeled by an empirical formula

$$L = CR\tanh^2(f/10)$$

where R is the rainfall rate (mm/hr) over the radome, f is the radar frequency (GHz) and C = 0.0575 for a coated radome or 0.165 for a standard radome (Merceret and Ward, 2002). The PAFB WSR-74C has a standard radome. Its two-way losses reach 1 dB at R = 10 mm/hr and reach 4.8 dB at R = 50 mm/hr. Qualitative observations of several cases and quantitative analysis of one (the authors acknowledge the contributions of Michael Brooks and Jennifer Ward of KSC to this analysis) indicate that the attenuation due to the wetting of the radome decays exponentially with a time constant of about 8.5 minutes upon termination or significant decrease of rainfall over the radome.

4.2 Cone of silence

The "cone of silence" is the conical region directly above the radar that is not scanned because it lies at an elevation angle higher than the elevation of the highest scan angle. For the WSR-74C, this cone is bounded by the 26 degree elevation common to both the 2000 and 2001 scan strategies shown in Figures D1 and D2. Within 20 km of the radar, clouds and precipitation at anvil height may not be detected because it is located in the cone. The cone of silence was also referred to as the radar “void” when aircraft observations were filtered for producing various scatter plots.

4.3 Scan gaps

Scan gaps occur between adjacent sweeps of the radar when the elevation difference between beams exceeds the beamwidth. Scan gaps will bias cloud top measurements to the low side since a cloud may extend upward beyond one scan elevation into the scan gap but not reach the next elevation. That cloud is taller than indicated since the radar can only report the presence of cloud to an altitude equivalent to the highest beam in

which it detects signal. Similarly, cloud bottom measurements are biased upward. The net result is to bias vertical cloud thickness estimates to the low side.

In the horizontal plane, scan gaps cause more distant features such as cloud edges to be biased toward the radar and closer features to be biased away from the radar. Again, this tends to bias the radial thickness of a cloud mass to the low side.

Radar reflectivity measurements are generally not biased by scan gaps unless there are large, non-linear gradients in the reflectivity field. In general, this is not a significant effect.

4.4 Propagation

Radar signals do not propagate in a straight line because they are refracted by gradients in the microwave index of refraction. The indicated height of each radar beam as a function of range is based on an assumption of standard propagation conditions (Doviak and Zrnic, 1993, Section 2.2). In the real atmosphere, conditions can deviate substantially from the assumed conditions. These deviations can result in the actual altitude of the beam differing by several kilometers from the indicated altitude at ranges of interest to the ABFM program (*ibid*; Wheeler, 1997). These effects can also result in errors in the radial positioning of features, although these errors are usually smaller than 1 km.

4.5 Comparison with WSR-88D

The WSR-74C and WSR-88D data generally agree well subjectively when attenuation of the WSR-74C is not a factor. A limited set of direct, quantitative comparisons were made by Michael Brooks of Dynacs, Inc. These indicated the systematic difference without attenuation was less than 1 dBZ when averaged over volumes of several tens of km^3 on a scan by scan basis. Some differences may be observed due to the processes used for putting the radar data on the same grid, especially in regions of large reflectivity gradients.

REFERENCES

Boyd, B.F., J.W. Weems, W.P. Roeder, C.S. Pinder and T.M. McNamara, 2003: Use of weather radar to support America's space program -- past present and future., Preprints, *31st International Conference on Radar Meteorology*, Seattle, WA August 6-12, 2003, 815-818.

Computer Sciences Raytheon, 2000: *Eastern Range Instrumentation Handbook*, Revision 15, January 2000.

Doviak, R.J. and D.S. Zrnic, 1993: *Doppler Radar and Weather Observations*, 2d Ed., Academic Press, San Diego, CA, 562 pp.

Merceret, Francis J. and Jennifer G. Ward, 2002: Attenuation of Weather Radar Signals Due to Wetting of the Radome by Rainwater or Incomplete Filling of the Beam Volume, NASA Technical Memorandum TM-2002-211171, April 2002, 16pp.

Short, D.A., 2000: *Final Report on IRIS Product Recommendations*, NASA Contractor Report CR-2000-208572, 18 pp.

Taylor, G.E., R.J. Evans, J.T. Manobianco, R.S. Schumann, M.M. Wheeler and A.M. Yersavich, 1994: *Report on the Comparison of the Scan Strategies Employed by the Patrick Air Force Base WSR-74C/McGill Radar and the NWS Melbourne WSR-88D Radar*, NASA Contractor Report 196291, 32 pp.

Wheeler, M.W., 1997: *Report on the Radar/PIREP Cloud Top Discrepancy Study*, NASA Contractor Report CR-204381, 18 pp.

Appendix E
WSR-88D RADAR

Frank Merceret, Monte Bateman and Sharon Lewis

1. DESCRIPTION OF THE RADAR

1.1 General Description

The WSR-88D weather radar is located at the National Weather Service Office in Melbourne, Florida (KMLB) about 45 km SW of the launch complexes at Cape Canaveral Air Force Station and Kennedy Space Center. The coordinates are 28 deg 06m 46s N, 80 deg 39m 14s W. The antenna is about 30m above mean sea level.

The radar is an S-band (10 cm) circularly polarized Doppler weather radar. The beam width is 0.95 degrees and the pulse width is 1.57 or 4.7 μs. Peak power is 750 kW. The pulse repetition frequency (PRF) may vary from 318 to 1304 Hz. Pulse pair processing is used to recover the Doppler information. Reflectivity data to a range of 460 km and Doppler data to a range of 230 km may be obtained with a resolution of 0.25 km. A full volume scan takes about 6 minutes. (CSR, 2000, Section 10.9)

1.2 Scan Strategy

The WSR-88D has four standard scan strategies called "Volume Coverage Patterns" (VCP) allocated among two modes: "Precipitation Mode" and "Clear Air Mode" (OFCM 2003, Chapter 4). Of these, only the Precipitation Mode VCP denoted VCP11 was used during the ABFM program. It is shown in Figure E1 below taken from Taylor *et al.* (1994).

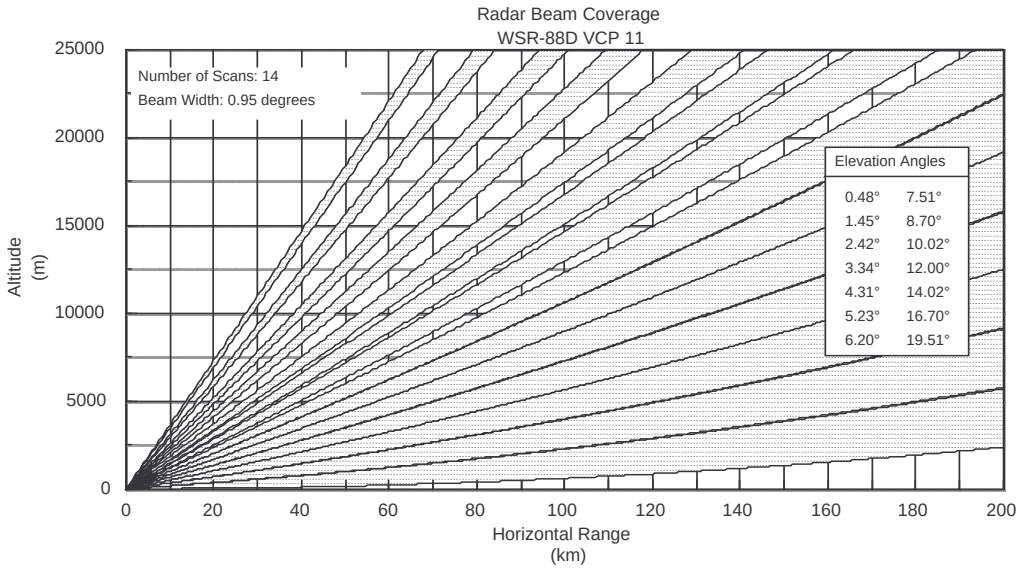

Figure E.1 WSR-88D Volume Coverage Pattern VCP11.

The operational radar products are generated in a Radar Product Generator (RPG) at the radar site and displayed on a Principal User Processor (PUP) (*ibid*; NWS/ROC, 2004), but the ABFM program generated its own products and displays from the archived Level II volume scan data.

1.3 Calibration

The WSR-88D is calibrated in two steps. First, the transmitter and receiver are calibrated by an end-to-end calibration referenced to a calibration port behind the antenna: then the antenna gain and pointing accuracy are verified by sun flux measurements (Operational Support Facility, 1997). The RMS calibration error is less than 1 dB (*ibid*).

1.4 Errors and limitations

The WSR-88D radar data are thresholded to maintain a 5 dB signal to noise ratio. Signals below the threshold are not recorded. The threshold is about -8 dBZ at a range of 50 km from the radar and +5 dBZ at 100 km. The effect of thresholding becomes evident beyond 75 km where signals below 0 dBZ are not available.

2. PREPROCESSING OF RAW DATA FOR SPRINT INGEST

The MLB NWSFO was requested to make 8mm (Exabyte) copies for the ABFM program on each operational day. During 2000, they made copies using old tapes that had been used many times. We had great difficulty reading data from these tapes. So for the 2001 season, the ABFM program supplied new tapes to use for these copies.

These data copies were NEXRAD ARC-II format archive tapes. We read the tapes into disk files, one file per volume scan. When reading the copies, a few of the 2001 tapes and many of the 2000 tapes would not read. Where possible, data were filled in by requesting data from the NCDC, using their online requesting system at has.ncdc.noaa.gov. These data were made available via FTP.

3. PRODUCTION OF CARTESIAN GRIDDED OUTPUT AND DISPLAY

As provided, SPRINT uses a grid of 225 x 225 points. We chose to use 1 km grid spacing, so our gridded domains are 225 x 225 km. In the vertical, they typically are 1-20 km in 1 km steps.

The grids were determined by looking at the aircraft track and trying to specify a single grid that would contain the track for the entire flight. On some days, two different grids were needed to contain the track. The gridded reflectivities were produced as one file per volume scan. These data were recorded to CD and sent to NCAR for final processing.

In order to simplify analysis among radars and aircraft data, the PAFB radar was chosen as the origin for all data. Thus, the KMLB data were translated so that the coordinate origin for gridded data was at the PAFB radar. The SPRINT input "card" was:

ORIGIN NEXRAD KMLB 28.1133 -80.6542 30.7 WSR74C 28.2557 -80.6055

which translates from the Lat/Long of KMLB to the Lat/Long of the WSR74C. The third parameter (30.7) is the altitude of the antenna in meters, above MSL. These data were obtained from:

http://scrl.usda.gov/SCRL/apmru/imms/meteorology/stncoord.html
or
http://www4.ncdc.noaa.gov/cgi-win/wwcgi.dll?WWDI~RadarList~N

which reports:

```
STATION ID    LAT N/ LONG W (deg,min,sec) ELEV(ft) TOWER HT(m)
   KMLB     280648 / 0803915                35         20
```

This gives an antenna elevation of: 35 ft + 20 m = 30.7 m MSL.

The gridded volume scan data were used to produce Constant Altitude Plan Position Indicator (CAPPI) and vertical cross-section displays. CAPPIs were produced for low, middle and high levels of the clouds under investigation for each mission day. Typically these were near 4, 7 and 10 km altitude. The vertical cross-sections were made along the flight track of the aircraft and incorporated into combined MER (microphysics, E-field and radar) plots.

4. ABFM ISSUES

4.1 Attenuation

The discussion of attenuation presented in Appendix D - WSR-74C Radar, Section 4.1 also applies to the WSR-88D although the numerical results differ because of the difference in wavelength and radome coating.

At the 10 cm wavelength of the WSR-88D, the constants in the intervening rain attenuation model are $a = 3.5 \times 10^{-5}$ and $b = 0.0647$. The model is valid for intervening reflectivities from 30 to 60 dBZ which encompasses the region from negligible attenuation (0.003 dB/km) at 30 dBZ to maximum likely reflectivity (60 dBZ) at which the attenuation is 0.3 dBZ/km. The WSR-88D has a hydrophobic radome. Its two-way losses reach 1 dB at R = 100 mm/hr.

4.2. Cone of silence

The discussion of issues relating to cone of silence in Appendix D - WSR-74C Radar, Section 4.2 also applies to the WSR-88D except that the location is over KMLB rather than PAFB. The highest beam for VCP11 is at an elevation of 19.5 degrees with a corresponding distance at anvil height of about 30 km.

4.3 Scan gaps

The discussion of issues relating to scan gaps in Appendix D - WSR-74C Radar, Section 4.3 also applies to the WSR-88D with appropriate differences in detail due to the differing scan strategies used by the two radars.

4.4 Propagation

The discussion of issues relating to propagation in Appendix D - WSR-74C Radar, Section 4.4 also applies to the WSR-88D.

5. COMPARISON WITH WSR-74C

The comparison between the WSR-74C and the WSR-88D is presented in Appendix D - WSR-74C Radar, Section 5.

REFERENCES

Computer Sciences Raytheon, 2000: *Eastern Range Instrumentation Handbook*, Revision 15, January 2000.

Merceret, Francis J. and Jennifer G. Ward, 2002: *Attenuation of Weather Radar Signals Due to Wetting of the Radome by Rainwater or Incomplete Filling of the Beam Volume*, NASA Technical Memorandum TM-2002-211171, April 2002, 16pp.

Operational Support Facility, 1997: *WSR-88D Reflectivity Calibration*, Technical Advisory Committee Briefing, OSF Engineering Branch, November 4, 1997, 13 pp.

National Weather Service Radar Operations Center, 2004: Operator Handbook: Guidance on Adaptable Parameters, *WSR-88D Handbook, Volume 4, RPG, Revision No. 2*.

Office of the Federal Coordinator for Meteorology, 2003: *Federal Meteorological Handbook No. 11: Doppler Radar Meteorological Observations, Part A*, 34 pp.

Taylor, G.E., R.J. Evans, J.T. Manobianco, R.S. Schumann, M.M. Wheeler and A.M. Yersavich, 1994: *Report on the Comparison of the Scan Strategies Employed by the Patrick Air Force Base WSR-74C/McGill Radar and the NWS Melbourne WSR-88D Radar*, NASA Contractor Report 196291, 32 pp.

Wheeler, M.W., 1997: *Report on the Radar/PIREP Cloud Top Discrepancy Study*, NASA Contractor Report CR-204381, 18 pp.

Appendix F
LIGHTNING DETECTION AND RANGING (LDAR)

Frank Merceret and Sharon Lewis

1. DESCRIPTION OF THE SYSTEM

1.1 Principle of operation

LDAR detects the VHF pulses in the band from 63 to 69 MHz from all parts of the lightning process from initial breakdown to the final return stroke and marks the time of arrival of each pulse at four or more antenna sites. The times of arrival from at least four antennas permit the time of emission and the three position coordinates of the source to be determined. By using additional sites, a better fit and an error estimate are obtained.

1.2 Hardware

LDAR consists of a central site and six remote sites located roughly on a 10 km radius circle about the central site as shown in Figure F1.

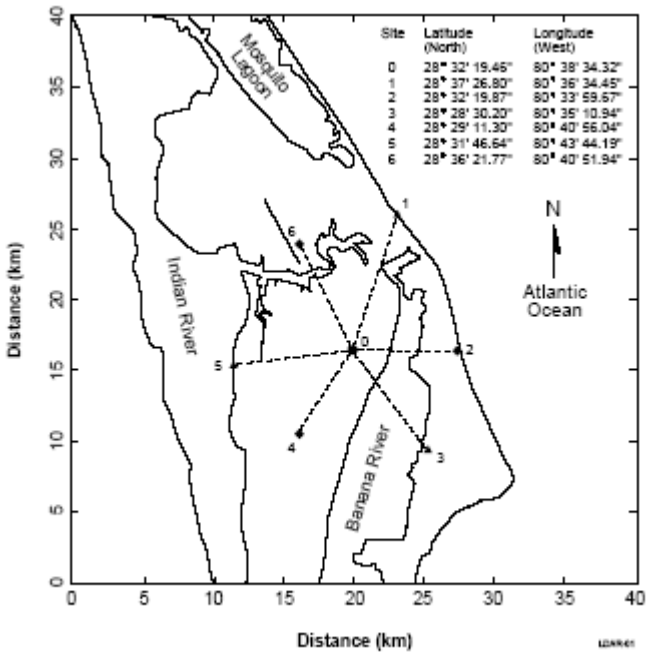

Figure F1. LDAR central site and remote site locations.

The remote signals are detected using logarithmic amplifiers, transmitted to the central site through microwave links and ingested into a "Timing Interval Unit" (TIU). The TIU includes a programmable time delay for the signals. Data from the TIU are processed in a Location Processor (LP) computer and distributed over a KSC/CCAFS LAN/WAN. Details are given in CSR (2000) Section 10.10.

1.3. Software

The arrival at the central site of a signal above a selectable threshold triggers digital sampling of the time-delayed signals in a preset window. Within the window, the largest signal from each antenna is time-tagged. The LP calculations account for the delay ("k-factor") introduced by each microwave link.

Events are located as follows. Any four of the seven sites can produce a location and time for a source. With seven sites receiving the signal and requiring that the central site participate in all solutions, there are 20 possible combinations of 4 sites. Using two of the 20 combinations of four sites is optimal for minimizing location errors for all x,y, and z values. If each coordinate (x,y,z) from two site combinations agrees within 5 percent or 350 meters, whichever is greater, the average x,y and z are used. Otherwise the solutions derived from all 20 combinations are used in determining the event location. In this case, the solutions are inter-compared for consistency and weighted appropriately. If x, y, and z of a given combination agrees within 5% or 350 meters, whichever is greater, of another combination, the weight of that solution is incremented by one. The event is located if the weight of any of the solutions exceeds seven, otherwise the location is the solution with the largest weight. The results are sent to the real time users and archived.

The LDAR data are in binary format. The format is slightly different between 2000 and 2001. Both have the same pattern:

-- block stating the time and number of flashes (num_flashes)
  -- Then there are "num_flashes" blocks
  --
  --
  ...

For 2001 the first block gives the second, and number of sources during that second (2000 has an additional variable that is not used). So the ingest for 2001 creates a structure with components of second and num_flashes (bloc = {second:0L, num_flashes:0}) and 2000 creates a structure with the additional unused variable (bloc = {second:0L, num_flashes:0, not_used:0})

NOTE: Although the software is written with num_flashes, num_flashes is really the number of sources detected during that second.

The time (or seconds) is in this first block is "computer time" where it is the number of seconds since 1970, so that needs to be converted to seconds from midnight on a 24 hour UTC clock.

After this first block there are blocks with more specific flash information for those number of flashes (there are num_flashes number of blocks following). These blocks have the format of (flash_info = {X:0L, Y:0L, Z:0L, time:0L}) where this time is given in milliseconds and measured as a dt from the time in the first block. So the time of a flash is given by:

bloc.second (time from 1970) - (conversion to current date) + flash_info.time*1e-6

The x, y and z is in meters measured from the central LDAR receiver, so an x and y offset must be added to the x and y locations to put that information in km from the radar. That offset is found from the lat/long position of the LDAR and the conversion mentioned earlier.
lat_LDAR=28.5387
lon_LDAR=-80.6428

Software was written to output this information into ASCII format. (This ASCII data are available on the web.) The format is:

```
yymmdd hhmmss  sfm  Nsources index   x      y        z       time
010618 120000 43200.0   9    0    -4.9757  29.9126  0.3150 43200.002537
```

where Nsources is number of sources, and index is just a count of the sources (starting with 0) for that second. x,y, and z are measured from the WSR74C radar, and the time is given to milliseconds.

Software was also written to determine the number of LDAR sources and CG flashes within a particular spatial range (we chose plus or minus 20 km) of the aircraft location and a time range (we chose plus 5 minutes and plus or minus 5 minutes).
The format is:

sfm	acx	acy	acz	ldmtrng	cgmtrng	ldpmtrng	cgpmtrng	noldar
sfm	km	km	m	cnt	cnt	cnt	cnt	nounits
78020.000	47.5348	-45.5785	6325.4473	47.	0.	137.	1.	1

where acx, acy, acz is the aircraft location with 0 being the location of the WSR74C.
ldmtrng is the number of LDAR sources within the spatial range, and
minus the time range
cgmtrng is the number of CG flashes within the spatial range, and
minus the time range
ldpmtrng is the number of LDAR sources within the spatial range, and
plus or minus the time range
cgpmtrng is the number of CG flashes within the spatial range, and
plus or minus the time range

This data set is presented in 10 second increments in order to be used to create the LDARm5 CGm5 LDARpm5 CGpm5 noldar columns in the merged file.

noldar is a 0/1 flag indicating if there was any LDAR data at all during this 10 second time. noldar is 1 if the LDAR did not have any data in the 10 second time window (78020 in this example). The counts indicate there was LDAR data within the 5 minute time window, but the noldar=1 indicates there was no data at 78020.

Lightning plots were made using the same grid(s) as were used for the radar. Panels of x-z, y-z and z-t were also part of the plot. Some of the z-t panels (Fig F2: 010610 2140-2150) show that during heavy lightning the LDAR gets overloaded and will show zero (0) sources for some seconds. There are also examples of times when LDAR reports no

sources but there are CGs. (Fig F3: 010624 2030-2040). These times were determined by hand. No attempt was made to incorporate these times into the filtering, but a table was created that lists questionable times.

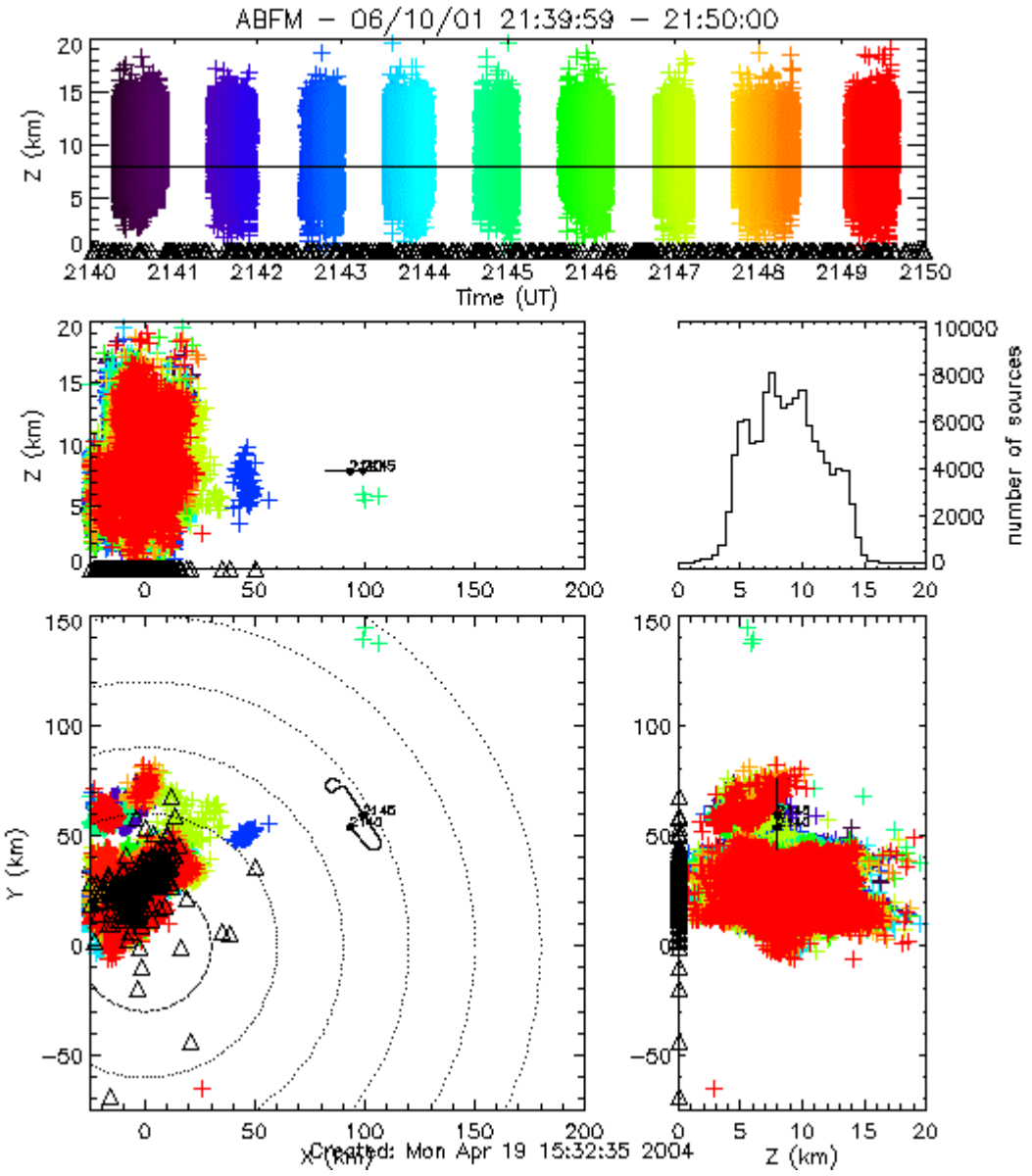

Figure F.2 Lightning plots from 010610 showing a case where the LDAR intermittently stopped showing sources.

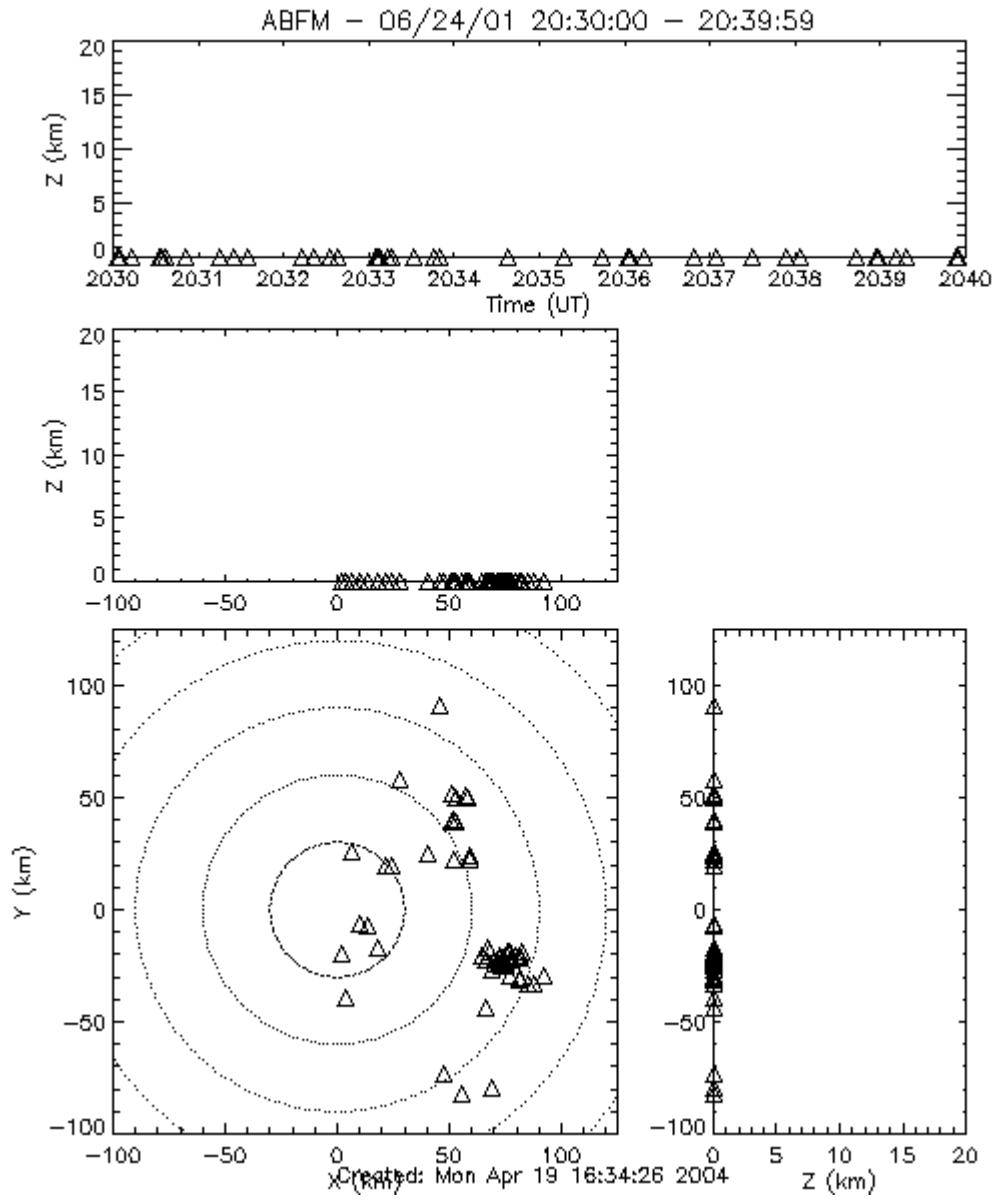

Figure F.3 Lightning plots from 010624 showing no LDAR sources, but plenty of CGs.

2. CALIBRATION

The major calibration concern is determination of the k-factor for each remote site and assuring that it has not changed. This is accomplished by transmitting a calibration pulse every minute exactly on the minute from a known location. If the pulse is not detected at any antenna for a prolonged period, maintenance may be required. If the position computed for the source of the calibration pulse is not accurate, the k-factors may need revision.

3. PERFORMANCE

3.1. Accuracy

LDAR locates sources with an accuracy of about 100m inside the network shown in Figure F1, and to within a few km at distances exceeding 100 km. The temporal resolution is less than 100 μs (Boccippio *et al.*, 2001). The flash detection efficiency approaches 100% inside the network (Maier, Maier and Lennon, 1995). Studies of the system accuracy in tracking an airborne test signal are provided in Maier, Lennon and Britt (1995).

3.2. Reliability

There are two significant factors that reduce the reliability of the LDAR system: hardware failures and radio frequency interference (RFI). The principal hardware failures are damage to remote site antennas and microwave link failures. Both are usually caused by exposure to the rough environment of the remote sites which are located in a wildlife preserve. Large birds will sit on the sense and communications antennas, ultimately damaging them. Lightning is also a constant threat. It is not unusual to lose one or more remote sites during heavy thunderstorm activity, but it is unusual to lose enough to prevent computing a valid and accurate solution.

RFI is caused primarily by tropospheric ducting of commercial channel 3 (60 - 66 MHz) television broadcast signals from large metropolitan areas several hundred km distant. Its signals do not meet the criteria to be recognized as lightning transients, so RFI generally does not produce false data. It does, however, raise the noise level that lightning signals must penetrate, thus reducing the detection efficiency substantially.

3.3. Sources of error

The primary source of error is false locations generated by the location algorithm. The algorithm also performs poorly in altitude and range for sources at large distances although the azimuth is generally quite accurate. This results in distant, heavy storms appearing smeared out in the radial direction, looking like "spokes" on the graphic display. Occasionally, the algorithm will generate a solution that is at the right distance from the central site but in exactly the opposite direction from the true direction. The cause of this 180 degree ambiguity is unknown, but it is observed infrequently. Finally, on days with multiple storms with heavy lightning, signals from multiple sources may appear within the same analysis window. This will sometimes generate a "wild" solution having no correspondence to any real source.

4. ISSUES FOR ABFM

The primary issue for the ABFM analysis is mislocated sources. Missing data are also a concern during periods of intense electrical activity such as shown in Figure F2 or periods of LDAR malfunction.

REFERENCES

Boccippio, D.J., S.J. Heckman and S.J. Goodman, 2001: A diagnostic analysis of the Kennedy Space Center LDAR network. 1. Data Characteristics. *J. Geophys. Res.*, **106**, 4769-4786.

Computer Sciences Raytheon, 2000: *Eastern Range Instrumentation Handbook*, Revision 15, January 2000.

Lennon, C. and L. Maier, 1991: Lightning Mapping System, *Proceedings of the 1991 International Aerospace and Ground Conference on Lightning and Static Electricity*, Cocoa Beach, FL, April 16-19, 1991, pages 89-1 to 89-10.

Maier, L., C. Lennon and T. Britt, 1995: Lightning Detection and Ranging (LDAR) system performance analysis. Preprints, *Sixth Conference on Aviation Weather Systems*, American Meteorological Society, Dallas, TX, January 15-20, 1995, 305 - 309.

Maier, M.W., L.M. Maier and C. Lennon, 1995: Lightning detection and location systems for spacelift operations. Preprints, *Sixth Conference on Aviation Weather Systems*, American Meteorological Society, Dallas, TX, January 15-20, 1995, 292 - 297.

Ushio, T., S.J. Heckman, and H. J. Christian, 2003: Vertical development of lightning activity observed by the LDAR system: lightning bubbles. *J. Appl. Meteor.*, **42**, 165 - 174.

Appendix G

CLOUD TO GROUND LIGHTNING SURVEILLANCE SYSTEM (CGLSS)

Frank Merceret and Sharon Lewis

1. DESCRIPTION OF THE SYSTEM

1.1 Principle of operation

The CGLSS records the position of cloud to ground lightning strikes near KSC and CCAFS. It detects radio signals radiated by the return stroke lightning channel. Positions are determined by a proprietary algorithm of Global Atmospherics, Inc. (GAI) that uses both the direction to the signal from direction finding antennas and the time of arrival of the signal at the antenna site.

1.2 Hardware

CGLSS consists of six GAI model 141-T Advanced Lightning Direction Finders (ALDF), a GAI IMPACT 280-T Advanced Position Analyzer and associated displays. Each sensor contains two magnetic direction-finding antennas, three horizontal electric field plates and a GPS antenna (CSR, 2000, Section 10.8). The locations of the ALDFs are shown in Figure G1.

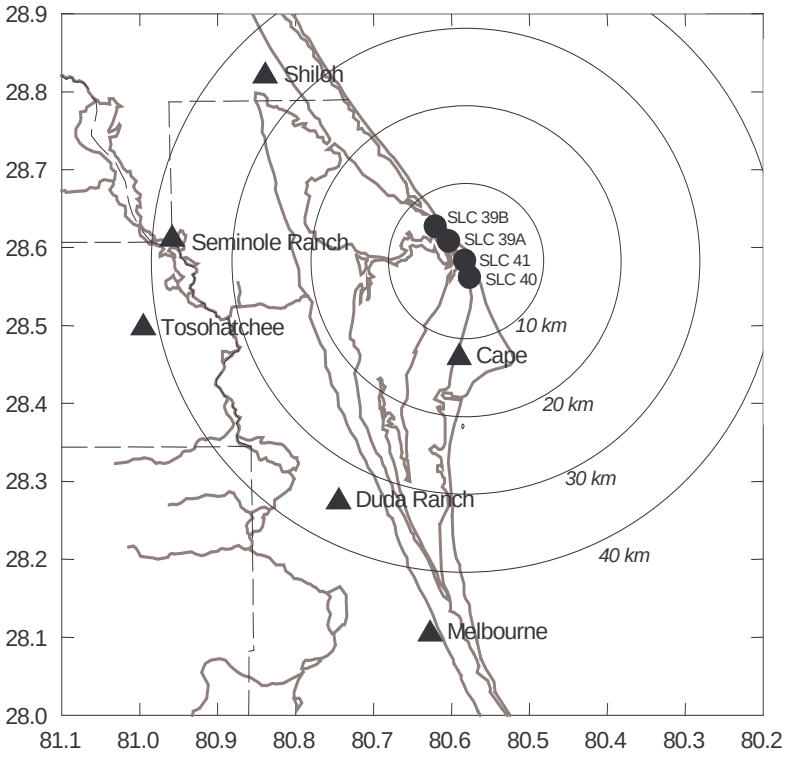

Figure G1. Locations of the CGLSS ALDF sensors during the ABFM program.

1.3 Software

Details of the flash location algorithm are proprietary. The algorithm uses both time of arrival and directional information from each antenna to select an optimum solution among all possible solutions for the time and location of the flash (*ibid*.).

There were two formats that the CGLSS data came in. They were both an ASCII format. The first had been pre-filtered and only contains data within 150 km of the radar (all of the 2000 data are in this format). This is a double spaced ASCII format that is produced in one hour increments, so they needed to be concatenated together and the headers of the subsequent files removed. There are nine columns in these files the first four were used in the work done at NCAR, the other five deal with the number and sign of the return strokes, and some QC parameters (see the web page for more details).

The header and a line of data look like this:

```
DAY[CYD]  HMS[HMS]  LAT[DEG]  LON[DEG]     NSTR  RS  DF1  DF2   FLAG

--------- --------- --------- --------- --------- --- ---- ----   ----

 2000164   110110   28.4413   79.6688   -147.4  2   1   6  +
```

Where the day is in year-Julian date (yyyyjjj),
time is in hour-minute-second (hhmmss), and
Latitude and longitude of the flash is given in decimal degrees.

Some of the 2001 data were available in a more detailed ASCII format. These data were not filtered to be within 150 km and the time is given in fractions of seconds. The header for this data is as follows:

```
time            lat          long    current  #rs    Stations
17:24:30.04   28:03:31  -80:41:13   -25.0    4  r  2,3,1,6,5
```

Again it is the first three columns of interest to the plotting routines used at NCAR.

time is in hour:minutes:decimal seconds
and the lat/long is in degrees:minutes:seconds
current is current of the first stroke in LLP units and indicates polarity
Stations gives the station numbers used for the solution

The software reads in the file then calculates the distance from the radar in km from the latitude and longitude given in the data.

All of the software developed at NCAR for the ABFM project used the same calculation for the lat/long to x/y with the exception of the radar data processing. The sprint software has a separate calculation for lat/long to x/y.

The IDL code for the conversion used in the software developed for the ABFM project follows.

```
;;;
```

```
  new_data(ind).x_pos = float(range*sin(head*torad))
  new_data(ind).y_pos = float(range*cos(head*torad))
endif else begin ;}{
  new_data(ind).x_pos = !values.f_nan
  new_data(ind).y_pos = !values.f_nan
endelse

end
;;;
```

present since a system upgrade was performed early in 2000 (Hal Herring, Computer Sciences Raytheon, private communication). These are all real lightning flashes, but have very large position errors related to the error minimization algorithm finding a local rather than a global minimum solution. This does not occur frequently, but in storms with high flash densities, a few may occur. This QC work has not been done.

1.4 Calibration

The principal calibration concern is the geographical alignment of the direction-finding antennas. This is determined initially at installation of each sensor and refined if necessary as experience with each sensor is obtained. Sensor location is determined by GPS.

1.5 Performance

1.5.1. Accuracy

The location accuracy of CGLSS is on the order of 300 meters (50% CEP) inside the area covered by the network shown in Figure G1 when all six sensors are active. At a range of 100 km, the accuracy is on the order of 3 km. Accuracy degrades when less than the full suite of sensors is available. With only two sensors, the accuracy at 20 km range is on the order of 1 km. The detection efficiency is a function of how many sensors are functioning. With the full set of sensors, the detection efficiency is better than 98%. With fewer active sensors the detection efficiency degrades. With only 2 sensors active, the detection efficiency falls below 60%. About 2% of the flashes detected are false indications not corresponding to actual lightning.

1.5.2. Reliability

CGLSS has frequent sensor outages due to the remote rural locations of the sensors and the difficult environment in which they must operate. The sensors themselves as well as essential communications links are subject to lightning-related power outages or damage. In major storms it is unusual if all six sensors continue to operate simultaneously.

1.5.3. Sources of error

CGLSS assumes a single cloud to ground strike is the source of the signals it processes. There are two primary causes of violation of that assumption: lightning flashes with multiple simultaneous ground attach points and strong in-cloud lightning. Both of these phenomena can generate spurious position estimates of the position of the detected lightning. In addition, the proprietary algorithm that optimizes the flash location sometimes converges on a local minimum rather than the global minimum in its least squares search procedure as noted above. This can cause a serious mislocation of the flash.

2. ISSUES FOR ABFM

The major concern for ABFM use of the CGLSS data has been the mislocated flashes noted immediately above. These must be manually identified by comparison with LDAR and radar data, a labor intensive process. Undetected flashes are also a concern, since the system detection efficiency is less than 100%.

REFERENCES

Computer Sciences Raytheon, 2000: *Eastern Range Instrumentation Handbook*, Revision 15, January 2000.

Maier, M.W., L.M. Maier and C. Lennon, 1995: Lightning detection and location systems for spacelift operations. Preprints, *Sixth Conference on Aviation Weather Systems*, American Meteorological Society, Dallas, TX, January 15-20, 1995, 292 - 297.

APPENDIX H
DESCRIPTION OF THE ABFM WEB SITE

Jim Dye and Sharon Lewis

It quickly became apparent that given the wealth of measurements a method was needed to display airborne and radar observations together. There also was a need to make these display products available to all participants at different institutions so that all members of the team could participate in analysis. As a result NCAR developed the ABFM Web site with the goal of not only displaying the measurements but also making the plots and many of the data sets available to participants (within the disk storage space limitation of the Web server). This Web site has now evolved into a powerful analysis and display tool and is described briefly in this Appendix. As this report is being written the ABFM Web site is being transferred to a server at NASA Kennedy Space Center.

At NCAR the URL for the ABFM Web site is: http://box.mmm.ucar.edu/abfm/
At NASA KSC the URL is yet to be determined

From this link the ABFM Home Page will come up and is shown in Figure H.1
Note the Instructions for Navigating This Website towards the bottom of the ABFM Home Page.

In addition to the need to be able to display and make analysis products available to participants we recognized the need to be able to view the radar and key airborne observations together on the same plots. To that end the MER (Microphysics, Electric fields, Radar) plots and also composite CAPPIs with overlay of aircraft track and if desired lightning observations from LDAR and CGLSS were developed at NCAR using the Interactive Display Language (IDL). Links to the different products are provided on each of the Daily Home Pages (ie. a page containing plots and data for each individual flight day). An example of one of the Daily Home Pages is shown in Figure H.2 for the Citation flight on June 13, 2000, the same flight that is described in Section 3.1 of the main body of the report.

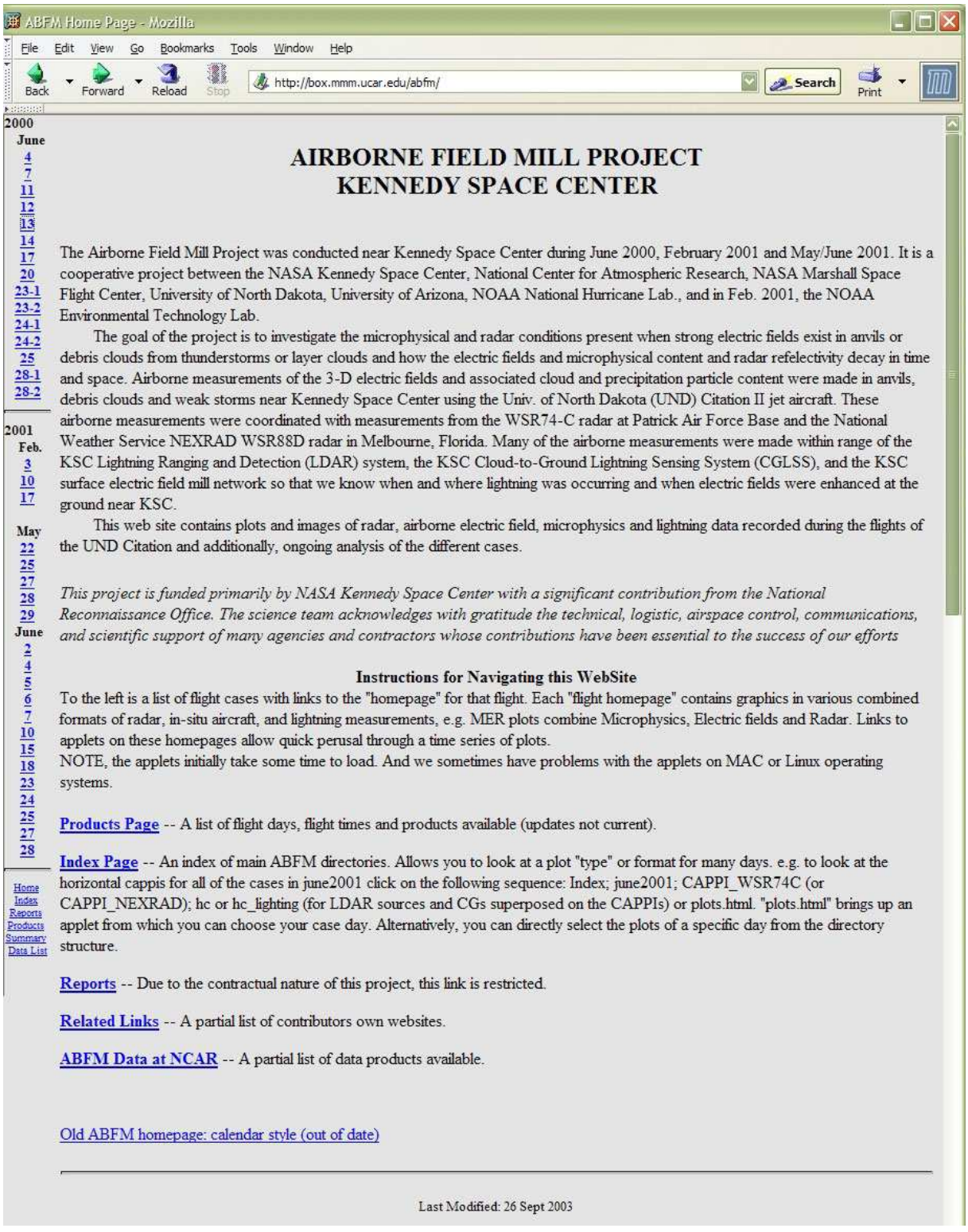

Figure H.1 The ABFM Home Web page. Links to each flight day are provided on the left and at the bottom there are links to various other sources of information including Reports.

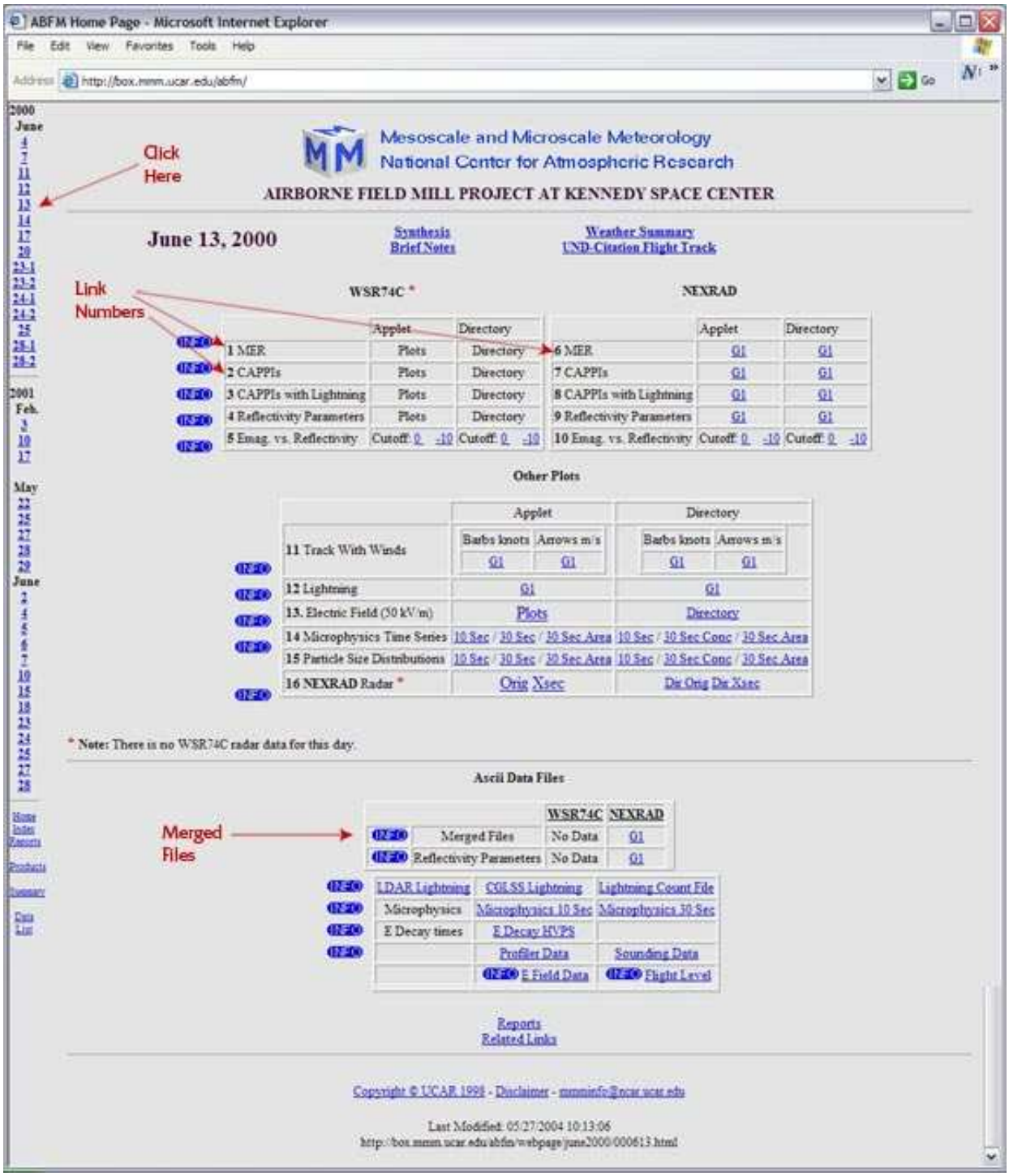

Figure H.2 The daily home page for the June 13, 2000 flight. See text.

At the top of each Daily Home Page there are links to a Synthesis, a Weather Summary, the Flight Track of the Citation and sometimes Brief Notes, all for that specific day. The Synthesis Link presents summaries and analyses done for that day. At the top of each

Synthesis there is a Summary Table. This table shows the time period of the aircraft investigation of the case; the type of case; complexity; degree of convective activity; approximate location (usually of the core); estimate of storm motion; and a brief verbal description of the case. It also presents minimum, maximum and average values for the resultant electric field, and particle concentrations in several different size categories for the specific time periods of each case. These statistics give a sense for the case but for most of the flights the variability is large so average and maximum values tell only part of the story. If the aircraft flew in more than one storm the above information is shown for each different case. Any analysis that has been written up for this flight day follows the Summary Tables. If more than one write-up was done, they are in reverse chronological order. Some of this analysis is from very early examination of the day, but often a more detailed analysis presented by an ABFM team member at a conference call is also provided.

Near the bottom of the Daily Home Page there is a Link to the "MERGED" data files for both the 74C and NEXRAD when data were available from both radars. They are an important source of measurements for any analysis to be undertaken. These MERGED files contain 10 sec averages of aircraft measurements of aircraft position and attitude, state parameters, microphysics and electric field time synchronized with various calculated reflectivity parameters.

The Daily Home Page also contains links to other measurements including the 1 s averages of the electric field measurements, LDAR and CGLSS lightning data, both 10 s and 30 s averaged particle measurements, KSC profiler and Rawinsonde measurements, and the Citation flight level data from the Univ. of North Dakota processing.

Links 1 and 6 (for WSR74C or NEXRAD radars, respectively) are to the MER plots that show measurements along the flight track of the Citation and the curtain of radar reflectivity in the column above and below the aircraft. MER plots have been produced for all days with radar data for both the PAFB WSR74C radar and also for the Melborne NEXRAD WSR88D. A 10 min time span is used for both the 74C and the NEXRAD MER plots to facilitate comparison. For the 74C this includes ~3 to 4 radar Volume Scans (~2.5 min each) and for NEXRAD 2 to 3 Volume Scans (~5 min each). More information on the MER plots (or any other link on the ABFM Web page) can be obtained by clicking on the "**INFO**" button beside the appropriate link. Examples of MER plots and CAPPIs can be seen in Section 3 of this report.

Links 2 and 7 show CAPPI plots for 74C and NEXRAD radar, respectively at altitudes of 4, 7 and 10 km MSL, or if the aircraft is airborne and near either 4 7 or 10 km, the CAPPI for the altitude of the aircraft (in 1 km increments) replaces the 4, 7 or 10 CAPPI. Aircraft track for the time period of the volume scan plus 2 min before and after are superimposed on the CAPPI.

Links 3 and 8 show the same CAPPI plots but with LDAR sources and CG flashes superimposed. Again more information about the plot can be obtained by clicking on the **INFO** button beside the link.

Links 4 and 9 display time series of different reflectivity parameters for the WSR74C or NEXRAD radar, respectively. We developed these plots for use in conjunction with our search for a radar parameter to be used for warning of the possibility of high electric fields. Information on the different plots can be found via the **INFO** button

Links 5 and 10 plot different reflectivity parameters as a function of Emag , the resultant electric field. We refer to these as scatter plots. These plots were used to explore the relationship between Emag and various reflectivity parameters in our quest for a suitable parameter to be used for a radar based LLCC for anvils.

Link 11 gives the aircraft track for that day in 10 min segments with the aircraft measured winds superimposed. There are periods during which the aircraft winds are not reliable because of icing of the nose and/or wing pitot tubes. During turns the winds may also be unreliable. The net result is that the winds need to be viewed very judiciously.

Link 12 goes to plots of lightning detected by LDAR or CGLSS. See the **INFO** button for an explanation of the plot format and Appendices F and G for descriptions of the LDAR and CGLSS measurement systems and uncertainty.

Link 13 leads to time series plots of the x, y and z components of the electric field, the magnitude of the total field (Emag) and charge on the aircraft (M Eq) and K Slack. Both of these later quantities are indicators of the quality of the electric field measurements.

Link 14 gives links to time series plots of 10 or 30 sec averages of particle concentration for different size categories. The link for 30 sec also shows time series of the particle cross-sectional area distributions for the anvil cases.

Link 15 leads to either 10 or 30 sec average plots of the particle concentration size distributions or for the 30 sec averages also to cross sectional area size distributions.

Link 16 shows CAPPI plots at 4, 7 or 10 km from the WSR74C radar except for the flight day of June 13, 2000. Because we have no recorded data for this day from the WSR74C radar, NEXRAD data are used.

Near the bottom of each Daily Home Page there are links to various ASCII data files that for the most part are self-explanatory. The MERGED files are files containing 10 sec average data from the aircraft and the corresponding radar reflectivity parameters for the location of the aircraft at that time. Some selected reflectivity parameters are contained in the MERGED file, while the Reflectivity Parameter file has fewer aircraft and microphysical parameters but includes most reflectivity variables that have been calculated. Those not listed can easily be calculated from variables included.

End of Report